Magnetoresistance of atomic structures studied with a Scanning Tunneling Microscope

Dissertation

zur Erlangung des Doktorgrades
der Mathematisch-Naturwissenschaftlichen Fakultät
der Christian-Albrechts-Universität zu Kiel

vorgelegt von

Johannes Schöneberg

Kiel, 2016

Erster Gutachter: Prof. Dr. Richard Berndt

Zweiter Gutachter: Prof. Dr. Stefan Heinze

Tag der mündlichen Prüfung: 03. November 2016

Zum Druck genehmigt: 10. November 2016

gez. Prof. Dr. Natascha Oppelt, Dekanin

Zusammenfassung

Spinabhängige Phänomene von Adsorbaten in unterschiedlichen magnetischen Umgebungen werden in dieser Arbeit mit einem Tieftemperatur-Rastertunnelmikroskop (RTM) untersucht. Spinpolarisierte Ströme und der anisotrope Magnetwiderstand (AMR) werden beobachtet für einzelne Atome und atomare Strukturen, die auf einer ferromagnetischen Fe Doppellage auf W(110) adsorbiert sind. Die magnetische Domänenstruktur dieser Lage besteht aus senkrecht (Domänen) und parallel (Domänenwänden) zur Oberfläche magnetisierten Bereichen. Äquivalente Adsorbate auf dieser Lage haben somit unterschiedliche magnetische Umgebungen, ohne dass ein externes Magnetfeld nötig ist.

Drei verschiedene Experimente zu Spin-Eigenschaften von atomaren Strukturen werden präsentiert. Mit spinpolarisierten Spitzen wird die Energie- und Abstandsabhängigkeit des spinpolarisierten differentiellen Leitwerts von einzelnen Ir Atomen untersucht. Unmagnetische Spitzen werden eingesetzt um die Auswirkungen der Spin-Bahn Kopplung (SBK) auf den differentiellen Leitwert von künstlich hergestellten Pb-Dimeren zu beobachten. Ebenso wird die durch SBK verursachte Leitwertänderung von atomaren Kontakten erforscht. Die letzten beiden Effekte werden dabei in Verbindung zum AMR gebracht, der die Widerstandsänderung für verschiedene Ausrichtungen der Magnetisierung aufgrund von SBK beschreibt.

Spinpolarisierte Messungen werden durchgeführt und zeigen, dass Ir Einzelatome durch die Fe Doppellage stark spinpolarisiert werden, obwohl Ir paramagnetisch als Volumenmaterial ist. Ein unbesetzter Zustand mit einer Spinpolarisation von über 60 % wird beobachtet, die invers zur Fe Lage ist. Diese Inversion wird durch das Filtern von Orbitalen durch die Tunnelbarriere verursacht. Die Abstandsabhängkeit dieses Filtermechanismus wird hier untersucht, indem der spin-abhängige differentielle Leitwert für unterschiedliche Abstände zwischen Spitze und Adatom und damit für verschieden große Tunnelbarrieren gemessen wird. Die Messungen zeigen, dass die Inversion konstant bleibt für den gesamten experimentell zugänglichen Bereich, der bis 1 Å an die Bildung des atomaren Kontakts heranreicht. Diese experimentellen Ergebnisse und weitere Berechnungen legen nah, dass die Inversion innerhalb des Nächste-Nachbar-Abstandes vom Ir Atom auftritt. Darüber hinaus ist das Auftreten einer Inversion energieabhängig.

Die Veränderungen des differentiellen Leitwerts aufgrund der SBK werden quantifiziert mit Hilfe des anisotropen magnetischen Tunnelwiderstandes (Tunnel-AMR, TAMR). TAMR wurde vorher mit dem RTM bei einzelnen Co Atomen beobachtet, aber bis jetzt gab es keine Untersuchungen für atomare Strukturen jenseits des Einzelatoms. Die atomare Umgebung kann jedoch die orbitale Struktur stark beeinflussen. Dadurch könnten SBK-abhängige Effekte und damit der TAMR wesentlich modifiziert werden, da die SBK direkt von der orbitalen Struktur abhängt. Diese Fragestellung wird hier untersucht, indem unterschiedlich ausgerichtete Pb Dimere auf der Fe Doppellage mit der Spitze des RTM gebaut werden. Für eine Dimer-Ausrichtung tritt ein signifikanter TAMR von $-20\,\%$ auf, wohingegen für die andere Ausrichtung kein TAMR beobachtet wird. Ein orbitales SBK-Modell wird verwendet, das den beobachteten TAMR durch eine SBK induzierte Hybridisierung erklärt, die Zustände mit unterschiedlichen Spins koppelt. Diese Ergebnisse zeigen, dass der TAMR modifiziert werden kann durch Adsorbate, die zusätzliche Orbitale beitragen und damit zu neuen Hybridisierungen durch SBK führen. Das unterschiedliche Verhalten der Dimere zeigt jedoch, dass dies empfindlich von der Adsorptionsgeometrie der Adsorbate abhängt.

Es wurde theoretisch vorhergesagt, dass AMR auch in ballistischen Kontakten auftreten sollte. Bisherigen Experimenten dazu mangelte es jedoch an einer Kontrolle auf der atomaren Skala und Magnetostriktion könnte die Ergebnisse beeinflusst haben. Diese Problematik wird hier gelöst, indem ballistische Kontakte mit dem RTM hergestellt werden, bei denen die Spitze des RTM einzelne Ir Adatome kontaktiert. Der vorhergesagte Effekt wird eindeutig nachgewiesen durch den kleineren Leitwert von Ir Adatomen auf Domänenwänden als auf Domänen. Experimente auf Co Adatomen bestätigen dieses Ergebnis. Dieser Leitwertunterschied variiert mit dem Spitze-Probe-Abstand. Berechnungen erklären dies durch das verschiedene Abklingverhalten der Orbitale in das Vakuum. Neue Transportkanäle treten im ballistischen Regime auf, die eine andere Symmetrie haben und somit anders hybridisiert werden durch SBK als die Kanäle, die den Strom im Tunnelbereich leiten.

Abstract

In this thesis spin-dependent properties of adsorbates placed in different magnetic environments are investigated using a low-temperature scanning tunneling microscope (STM). Spin-polarized currents and anisotropic magnetoresistance (AMR) are studied for single atoms and atomic structures adsorbed on a ferromagnetic Fe bilayer on W(110). This layer, thanks to its out-of-plane and in-plane magnetized domains and domain walls, respectively, allows to study equivalent adsorbates in different magnetic environments without the need for an external magnetic field.

Three different experiments on spin-properties of atomic structures are briefly introduced in the following. Using spin-polarized tips, the energy and distance dependence of the spin-polarized current of single Ir atoms is investigated. Nonmagnetic tips are employed to investigate the effect of spin-orbit coupling (SOC) on the differential conductance of artificially built Pb dimers and on the conductance of single atoms that are contacted with the STM tip. The last two effects are linked to AMR, which describes the SOC mediated dependence of the electrical resistance on the magnetization direction.

Spin-polarized measurements are performed and reveal that Ir is strongly spin-polarized by the Fe bilayer at the single-atom level even though it is paramagnetic as a bulk. An unoccupied state is observed with a spin polarization exceeding 60 % that is inverted with respect to the Fe layer. This inversion is caused by the tunneling gap acting as an orbital filter. To investigate this filtering mechanism the spin-dependent differential conductance is measured for different tip-adatom distances, *i. e.,* for different widths of the tunneling gap. The inversion of the spin-polarized signal is found to remain unchanged over the entire range of experimentally accessible distances from far in the tunneling regime to 1 Å from the point of contact formation. These findings and calculations strongly suggest that the inversion occurs within the next-neighbor distance from the single adatom. Furthermore, the occurrence of an inversion is found to be energy dependent.

The changes in the differential conductance due to SOC are quantified via the tunneling anisotropic magnetoresistance (TAMR). TAMR was previously observed with STM on single Co atoms, but so far no investigations for atomic structure beyond single atoms have been done. However, the atomic environment can strongly affect the orbital structure. In turn, SOC-induced effects like the TAMR may be considerably modified since SOC is directly linked to the orbital structure. This is investigated here by building differently oriented Pb dimers on the Fe bilayer with the tip of the STM. A significant TAMR of $-20\,\%$ is measured for one orientation of the dimers, while no TAMR is found for the other orientation. An orbital SOC model is used and suggests that the observed TAMR is a result of a SOC induced hybridization, which mixes states of different spin-character. These results show that the TAMR may be tuned by admixing new orbitals with adsorbates, which result in an additional hybridization due to SOC. However, as evidenced by the different behaviors of the different Pb dimers, this admixing crucially depends on the exact adsorption geometry.

It was predicted theoretically that AMR might occur in ballistic contacts. However, experimental results so far lacked control on the atomic scale and might have been influenced by magnetostriction. Here, these issues are resolved by forming ballistic contacts with the STM, *i. e.,* by contacting single Ir adatoms with the tip of the STM. The existence of the proposed effect is unambiguously shown by a lower conductance of the in-plane magnetized adatoms than for the out-of-plane magnetized adatoms. Experiments on Co adatoms confirm these findings. This conductance difference is found to vary with the tip-adatom distance. This is explained with the help of calculations by different decay rates of orbitals. Indeed, new transport channels emerge in the ballistic range, which are of different orbital symmetry and are thus differently influenced by SOC than the channels conducting the current in the tunneling regime.

Contents

List of abbreviations

AMR : anisotropic magnetoresistance

BAMR : ballistic AMR

dI/dV : differential conductance

DFT : density functional theory

DOS : density of states

FLAPW : full-potential linearized augmented plane wave method

GMR : giant magnetoresistance

LDOS : local density of states

MA : magnetocrystalline anisotropy

SOC : spin-orbit coupling

SQA : spin-quantization axis

STM : scanning tunneling microscope / microscopy

TAMR : tunneling anisotropic magnetoresistance

TMR : tunneling magnetoresistance

UHV : ultrahigh vacuum

1. Introduction

Magnetic media like hard disk drives are an ubiquitous component for storing data. Data bits are represented by different orientations of the magnetization in a ferromagnetic material. They are read using the giant magnetoresistance (GMR) effect [1–3]. This effect describes the dependence of the electrical resistance between two magnetic electrodes on the relative orientation of their magnetization directions. To prevent the magnetic moments of data bits from thermal fluctuations, they are stabilized via the magnetocrystalline anisotropy (MA) [3]. MA is the result of an interaction between the magnetic moment and the crystallographic structure caused by spin-orbit coupling (SOC) [4]. Tilting the magnetization results thus in different energies due to the anisotropy of the crystallographic structure.

SOC as well as GMR also manifest themselves in structures on the atomic scale. Experiments on this scale in real space became possible with the invention of the scanning tunneling microscope (STM) by Binnig and Rohrer [5, 6]. Furthermore, Eigler et. al showed that this experimental technique enabled the possibility to manipulate single atoms directly [7]. Shortly afterwards, Wiesendanger et al. obtained a magnetic contrast on the Cr(001) surface by introducing spin-polarized tips [8–10]. Consequently, numerous studies focused on magnetic properties of single atoms: Reports on spin-polarized measurements [11–15] as well as magnetic anisotropy [16–21] on the atomic level were published. The possibilities of atomic manipulation together with spin-dependent measurement were used to, *e. g.*, build spin-logics [22] and antiferromagnetically coupled Fe cluster, which stored magnetic bits [23].

Surprisingly, effects originating from spin properties may even be observed with non spin-polarized tips. As mentioned above, SOC results in different energies if the magnetization is tilted with respect to the crystallographic structure. This also affects the conductance of the tunneling junction in an STM, which was observed for a ferromagnetic domain structure [24] and single Co adatoms [25].

In this thesis, I examined three different spin-dependent properties of atomic structures adsorbed on the ferromagnetic domain structure of the second layer

Fe on W(110). Firstly, I investigated the spin-polarized signal of single Ir atoms and its dependence on thee tunneling gap between tip and adatom. Secondly, the effect of SOC on the differential conductance is studied for differently oriented Pb dimers, which have been built with the STM tip. Thirdly, the influence of SOC on the conductance of ballistic junctions is examined by contacting single adatoms with the STM tip.

This thesis is organized as follows:

In chapter **2**, a brief introduction to the basic theory of STM is given. This theory is then extended to the spin-polarized case. A derivation of the formula I use to link spin-polarized spectra of the differential conductance to the spin-polarization is presented. The limitations of this formula are discussed for a simplified model system.

Chapter **3** introduces SOC and its basic properties using a simplified orbital SOC model. The dependence of the SOC Hamiltonian on different orientations of the spin-quantization axis is discussed, which establishes the link between SOC and anisotropic magnetoresistance. The corresponding effect of SOC on the density of states and thus the spectra of the differential conductance is illustrated using this model.

Chapter **4** presents the basic properties of the Fe bilayer on W(110), which is used for all experiments presented in this thesis and in chapter **5** I give a short description of the experimental setup.

The energy- and distance-resolved spin-spectroscopy of single Ir atoms on the Fe bilayer is presented in chapter **6**.

The dependence of the differential conductance of differently oriented Pb dimers on the orientation of the magnetization is shown in chapter **7**.

In chapter **8** the conductance measurements of ballistic junctions on the atomic scale are presented.

The conclusion and an outlook of the thesis are in chapters **9** and **10**, respectively.

In the appendices in chapter **11** further information is given on SOC, on height corrections of experimental data and on the preparation stations used for high temperatures.

2. Spin polarized scanning tunneling microscopy

Shortly after the development of the scanning tunneling microscope (STM) by Binnig and Rohrer [5, 6], Tersoff and Hamann [26, 27] developed a theory that allowed the interpretation of STM data by linking the measured tunneling current to the densities of states (DOS) of sample and tip. Later, the emergence of experiments using ferromagnetic tips and samples [8] lead to an expansion of this theory considering the spin-resolved DOS [28]. In this chapter the 1D model of the tunneling current by Simmons [29] is first introduced for the non spin-polarized case. This theory is then extended to the spin-polarized case. Finally, the relation between the conductance asymmetry derived from spectra of the differential conductance ($\mathrm{d}I/\mathrm{d}V$) and the spin polarization of tip and sample is demonstrated. This relation is used in chapter **6** for single Ir atoms. For are more detailed description of the STM, please refer to Ref. [30].

According to Simmons [29], for 0 K the tunneling current I at an applied bias voltage V and a tip-sample separation z is:

$$I(z,V) \propto \int_0^{eV} \rho_S(\epsilon)\rho_T(\epsilon - eV)\tau(z,V,\epsilon)\mathrm{d}\epsilon \tag{1}$$

ρ_S and ρ_T are the spin-degenerate DOS of sample and tip, respectively. e is the elementary charge. The transmission factor τ describes the probability of an electron to tunnel through a voltage-dependent barrier. Using the Wentzel-Kramers-Brillouin approximation and assuming a trapezoid shape of the barrier, τ may be written as (see Ref. [31] and the appendix of [29]):

$$\tau(z,V,\epsilon) = \exp(-2\kappa z). \tag{2}$$

$\kappa = \frac{\sqrt{2m}}{\hbar}\sqrt{\overline{\Phi} + \frac{eV}{2} - \epsilon}$ is the decay constant for a particle with mass m and energy ϵ to tunnel through the barrier. $\overline{\Phi}$ is the mean of the workfunctions of tip and sample. $\hbar$ is the reduced Planck constant. For metals $\kappa \approx 1\,\text{Å}^{-1}$, so the tunneling current increases (decreases) by roughly an order of magnitude when the tip-sample separation is decreased (increased) by 1 Å. Consequently, STM measurements are highly sensitive to vertical displacements of the tip.

The voltage derivative of equation (1) under the assumption of an energy-

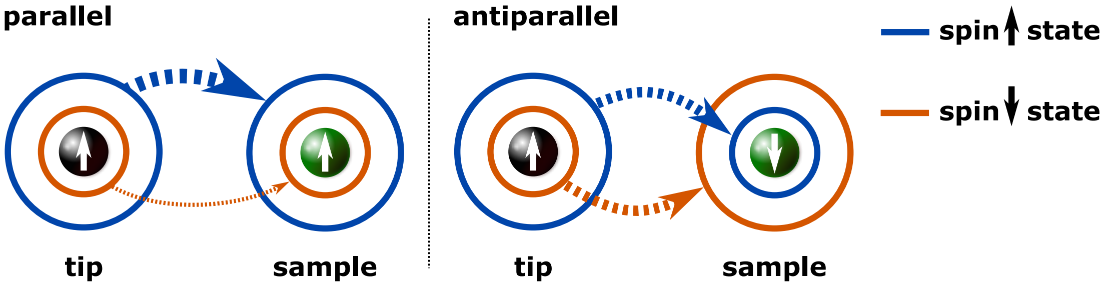

Figure 1. **Principle of spin-polarized scanning tunneling microscopy** Sketch of collinear tunneling for a parallel (left) and antiparallel (right) alignment of the magnetization axes of tip and sample in an orbital representation. The extent of the orbitals indicates isosurfaces of the spin-polarized DOS. If the spin is preserved, tunneling only occurs between states of same spin, which is indicated by the dashed arrows. The width of the arrows reflect the amount of the current that can pass through the corresponding orbitals.

independent tip DOS ($\frac{\mathrm{d}\rho_T}{\mathrm{d}V} = 0$) yields:

$$\frac{\mathrm{d}I(z,V)}{\mathrm{d}V} \propto \rho_S(eV)\,\rho_T(0)\,\tau(z,V,eV) + \rho_T \int_0^{eV} \rho_S(\epsilon)\frac{\mathrm{d}\tau(z,V,\epsilon)}{\mathrm{d}V}\mathrm{d}\epsilon \tag{3}$$

The second term in equation (3) results in a monotonous background in $\mathrm{d}I/\mathrm{d}V$ curves [10]. Additional features on top of $\mathrm{d}I/\mathrm{d}V$ curves are thus associated with the sample DOS. For smaller voltages, however, the second term may be discarded, so $\mathrm{d}I/\mathrm{d}V$ spectra are directly proportional to the sample DOS.

The spin-degeneracy is lifted in measurements involving magnetic tips and samples. Consequently, the DOS needs to be separated in its spin-up ($\rho_\uparrow$) and spin-down ($\rho_\downarrow$) contributions. In general the spin-quantization axes of tip and sample are not collinear. Their relative alignment may further depend on the applied bias voltage and the location of the tip above the sample. Wortmann et. al developed a theory based on the Tersoff-Hamann model that incorporates these effects [28]. Here, collinearly spin-polarized electrodes are considered and thus equation (1) simplifies to a variation of the Julliere model [9, 32]. Under the

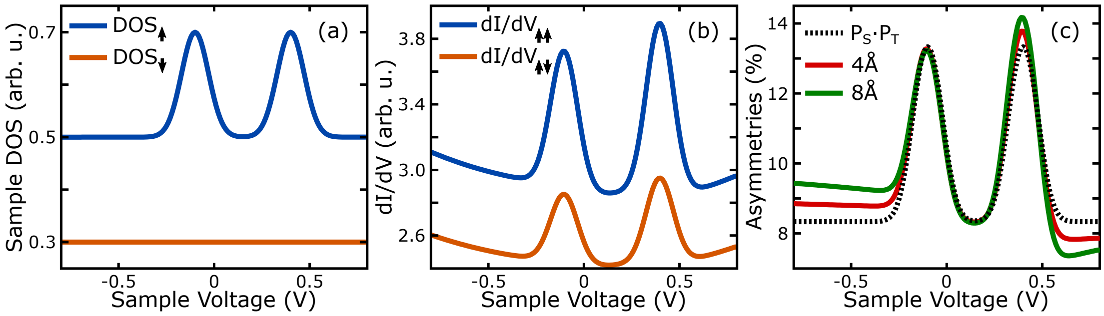

Figure 2. **Influence of the transmission factor on the asymmetry**

(a) Model sample DOS with constant spin-down DOS. The spin-up DOS has two identical peaks at different voltages. (b) dI/dV curves calculated via equations (4) and (5) and subsequent derivation. The spin-up and the spin-down DOS of the tip were set to constant values with a spin polarization of the tip of $P_T = 33.3\,\%$. Due to this partial spin polarization of the tip, the peaks of the spin-up DOS occur in both dI/dV curves. (c) Asymmetries calculated from dI/dV-curves at tip-sample separations of 4 Å and 8 Å and the expected asymmetry according to equation (9). While the peak close to the Fermi level is reproduced well, deviations between the expected and modeled asymmetry occur for the peak at higher voltages, which are furthermore dependent on the size of the tunneling gap.

assumption of the spin being preserved in tunneling one gets

$$I(z,V)_{\uparrow\uparrow} \propto \int_0^{eV} \left(\rho_{S,\uparrow}(\epsilon)\rho_{T,\uparrow}(\epsilon - eV) + \rho_{S,\downarrow}(\epsilon)\rho_{T,\downarrow}(\epsilon - eV)\right)\tau(z,V,\epsilon)\,\mathrm{d}\epsilon \qquad (4)$$

$$I(z,V)_{\uparrow\downarrow} \propto \int_0^{eV} \left(\rho_{S,\downarrow}(\epsilon)\rho_{T,\uparrow}(\epsilon - eV) + \rho_{S,\uparrow}(\epsilon)\rho_{T,\downarrow}(\epsilon - eV)\right)\tau(z,V,\epsilon)\,\mathrm{d}\epsilon \qquad (5)$$

with the current $I_{\uparrow\uparrow}$ ($I_{\uparrow\downarrow}$) for a parallel (antiparallel) alignment of the magnetizations of tip and sample (see Fig. **1**). Note that the transmission factor τ is assumed to be independent on the spin. If the voltage derivative of the transmission factor is discarded, equation (3) modifies accordingly to

$$\mathrm{d}I/\mathrm{d}V_{\uparrow(\uparrow,\downarrow)} \propto \left(\,\rho_{S,(\uparrow,\downarrow)}(eV)\,\rho_{T,\uparrow}(0) + \rho_{S,(\downarrow,\uparrow)}(eV)\,\rho_{T,\downarrow}(0)\,\right)\tau(z,V,eV). \qquad (6)$$

The spin polarization may be extracted from the conductance asymmetry A, which is defined as [9, 10]:

$$\begin{aligned} A &= \frac{\mathrm{d}I/\mathrm{d}V_{\uparrow\uparrow} - \mathrm{d}I/\mathrm{d}V_{\uparrow\downarrow}}{\mathrm{d}I/\mathrm{d}V_{\uparrow\uparrow} + \mathrm{d}I/\mathrm{d}V_{\uparrow\downarrow}} \\ &= \frac{(\rho_{S,\uparrow}\rho_{T,\uparrow} + \rho_{S,\downarrow}\rho_{T,\downarrow}) - (\rho_{S,\downarrow}\rho_{T,\uparrow} + \rho_{S,\uparrow}\rho_{T,\downarrow})}{(\rho_{S,\uparrow}\rho_{T,\uparrow} + \rho_{S,\downarrow}\rho_{T,\downarrow}) + (\rho_{S,\downarrow}\rho_{T,\uparrow} + \rho_{S,\uparrow}\rho_{T,\downarrow})} \\ &= \frac{(\rho_{T,\uparrow} - \rho_{T,\downarrow})(\rho_{S,\uparrow} - \rho_{S,\downarrow})}{(\rho_{T,\uparrow} + \rho_{T,\downarrow})(\rho_{S,\uparrow} + \rho_{S,\downarrow})} \end{aligned} \tag{7}$$

For this derivation it is mandatory, that the $\mathrm{d}I/\mathrm{d}V$ spectra are measured at the same height, or otherwise the transmission factors would not cancel out. The influence of height differences and their correction are discussed in chapter **11 (b)**. With the definition of the spin polarization P

$$P = \frac{\rho_\uparrow - \rho_\downarrow}{\rho_\uparrow + \rho_\downarrow} \tag{8}$$

equation (7) can be written concisely:

$$A(V) = P_\mathrm{T}\, P_\mathrm{S}(V) \tag{9}$$

with the spin polarization P_T (P_S) of the tip (sample). Note that this relation was derived under the assumption of a constant tip DOS (resulting in a constant spin polarization of the tip), collinear orientation of the tip and sample magnetization and neglecting corrections due to the transmission factor (second term in equation (3)). However, even if the tip fulfills all requirements, the transmission factor may not be fully discarded. Indeed, Fig. **2** shows that due to the transmission factor the conductance asymmetry depends on the tip-sample separation and the voltage. The asymmetry therefore deviates from the relation given in equation (9), especially at elevated voltages. Consequently, equation (9) should be regarded as a qualitative relation that helps to compare experimental result with calculated spin polarizations, which is done in chapter **6** for spin-polarized measurements of single Ir atoms.

3. Spin-orbit coupling

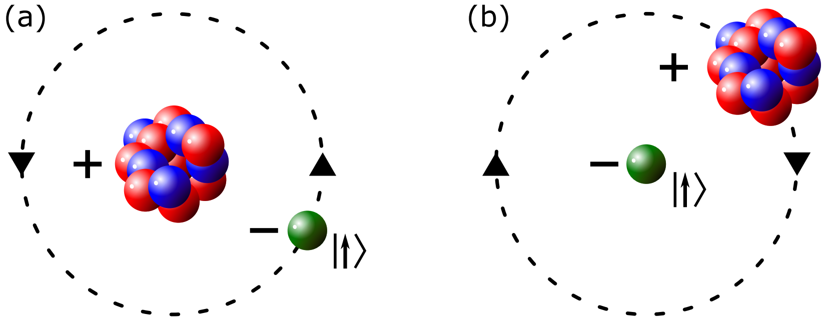

Figure 3. **Sketch of a simplified SOC model**

(a) A negatively charged electron is orbiting around a positively charged nucleus. (b) The frame of reference is changed to the electron. In this frame, the nucleus is orbiting around the electron, producing an electric current and thus a magnetic field. This magnetic field interacts with the spin ($|\uparrow\rangle$) of the electron and thereby induces energy corrections to the Hamiltonian, which is the spin-orbit coupling [33].

Spin-orbit coupling (SOC) (also called spin-orbit interaction) is a fundamental effect in solid-state physics because it connects the anisotropic real-space structure of crystals with the spin. This results in a dependence of spin related effects on the orientation of the magnetization with respect to the crystallographic structure. Prominent examples are the magnetocrystalline anisotropy, which is the varying amount of energy required to magnetize a crystal in different directions, and the anisotropic magnetoresistance (AMR), which is the dependence of the resistance upon the orientation of the magnetization. See Ref. [4] for a detailed description of these effects. AMR is related to investigations presented in this thesis in chapters **7** and **8**. In the present chapter a brief introduction to SOC is thus given and some general properties are discussed. Then, the effect of SOC on the DOS and the differential conductance in STM experiments is illustrated within a simplified orbital SOC Hamiltonian.

The mechanism of SOC may be understood intuitively from a simplified model sketched in Fig. **3** [33]: Consider a system consisting of an electron orbiting around a nucleus in the resting frame of the nucleus. This system may be transformed to the resting frame of the electron, where the nucleus is orbiting around the electron. This moving charge corresponds to a current that is generating a magnetic field. Spin-orbit coupling originates from the interaction between the spin of the electron and the field generated by its orbital movement.

Dirac showed that spin is a consequence of relativistic considerations with the formulation of a relativistic wave equation. Consequently, a more sophisticated approach to derive the SOC Hamiltonian (H_{SOC}) occurs naturally, when the Dirac equation is approximated for small velocities [34]:

$$H_{\mathrm{SOC}} = -\frac{e\hbar}{4m^2c^2}\,\boldsymbol{\sigma}\cdot\mathbf{E}\times\mathbf{p} \tag{10}$$

with $\boldsymbol{\sigma}$ the vector of the Pauli spin matrices, $\mathbf{E}$ the electric field and $\mathbf{p}$ the momentum operator. Under the assumption of a central field, $\mathbf{E}$ may be written as $\mathbf{E} = -grad(\varphi) = -\frac{1}{r}\frac{\mathrm{d}\varphi}{\mathrm{d}r}\,\mathbf{r}$, with φ the electric potential. Using this result and the dimensionless definition of the angular momentum $\mathbf{l} = \frac{1}{\hbar}\,\mathbf{r}\times\mathbf{p}$ equation (10) results in:

$$H_{\mathrm{SOC}} = \frac{e\hbar}{4m^2c^2}\,\boldsymbol{\sigma}\cdot\frac{1}{r}\frac{\mathrm{d}\varphi}{\mathrm{d}r}\,\mathbf{r}\times\mathbf{p} = \lambda\,\boldsymbol{\sigma}\cdot\mathbf{l} \tag{11}$$

with the spin-orbit parameter $\lambda = \frac{e\hbar^2}{4m^2c^2r}\frac{\mathrm{d}\varphi}{\mathrm{d}r}$. $\lambda \propto Z/r^3$ for a Coulomb potential ($\varphi \propto Z/r$) with Z the atomic number. Evaluating the expectation value of $1/r^3$ for hydrogen like atoms yields $\lambda \propto Z^4$ [31, 35], *i. e.,* heavy atoms are expected to be more affected by SOC. For $3d$ elements values of λ on the order of 25 meV were reported [25, 36, 37][1].

Equation (11) may be rewritten to a handy formula by introducing the Pauli spin matrices

$$\sigma_x = \begin{pmatrix} 0 & 1 \\ 1 & 0 \end{pmatrix} \qquad \sigma_y = \begin{pmatrix} 0 & -i \\ i & 0 \end{pmatrix} \qquad \sigma_z = \begin{pmatrix} 1 & 0 \\ 0 & -1 \end{pmatrix}$$

and the creation and annihilation operators of the angular momentum $l_\pm = l_x \pm i\, l_y$

---

[1] In Refs. [25, 36, and 37] the SOC Hamiltonian is defined as $H_{\mathrm{SOC}} = \xi\,\mathbf{s}\cdot\mathbf{l}$ with $\mathbf{s} = \boldsymbol{\sigma}/2$ as the dimensionless spin-operator. The spin-orbit parameter ξ consequently relates to λ via $\lambda = \xi/2$.

(see Ref. [31] for the properties of these operators):

$$H_{\mathrm{SOC},\,z}=\lambda\begin{pmatrix} l_z & l_- \\ l_+ & -l_z \end{pmatrix} \tag{12}$$

The index z indicates that the spin is quantized along the z direction. The hybridization between states with different and equal spin is described by the off-diagonal and diagonal operators, respectively. States with equal spin are thus coupled via l_z. Consequently, different eigenstates of l_z are not hybridized via SOC because they are orthogonal.[2] States with different spin, however, may be mixed. SOC thus results in eigenstates that are a mixture of different spin states.

Equation (12) was derived for an identical quantization axis of spin and angular momentum (z-axis). In a bulk system, however, the orbital moment is linked to the crystallographic structure while the spin direction may be altered by a magnetic field. The SOC Hamiltonian for a spin-quantization axis (SQA) along the y-direction can be derived by interchanging the Pauli spin matrices to [4]:

$$\tilde{\sigma}_x = -\sigma_y \qquad \tilde{\sigma}_y = \sigma_z \qquad \tilde{\sigma}_z = -\sigma_x$$

This results in a more complex equation for SOC:

$$H_{\mathrm{SOC},\,y}=\lambda\begin{pmatrix} \frac{i}{2}(l_- - l_+) & -l_z + \frac{i}{2}(l_- + l_+) \\ -l_z - \frac{i}{2}(l_- + l_+) & -\frac{i}{2}(l_- - l_+) \end{pmatrix} \tag{13}$$

The resemblance between equations (12) and (13) is nonetheless apparent since $\pm\frac{i}{2}(l_- - l_+) = \pm l_y$ and $-l_z \pm \frac{i}{2}(l_- + l_+) = -l_z \pm i l_x$. In contrast to equation (12) states with equal spin are now coupled via l_y. Eigenstates of l_z with equal spin may therefore be hybridized. Tilting the spin-quantization axis consequently results in a varying hybridization between the states. The total energy, however, remains constant, which can be shown in a more general scheme since the trace of a diagonalizable matrix equals the sum of its eigenvalues and

$$tr(H_{\mathrm{SOC}}) = 0. \tag{14}$$

(See also Ref. [36] and chapter **11 (a)**). This property originates from the equal number of positive and negative orientations of the angular momentum and the spin in a fully occupied shell that cancel each other.

---

[2] $<1\,|l_z|\,2> \propto <1\,|\,2>= 0$ for two different eigenstates $|\,1>$, $|\,2>$ of l_z.

The differences in H_{SOC} for spin-quantization axes along the z- and y-direction may be illustrated by evaluating equations (12) and (13) for the Cartesian p-states, *i. e.*, $p_x = \frac{1}{\sqrt{2}}(\,|\,1,-1> - \,|\,1,1>)$, $p_y = \frac{i}{\sqrt{2}}(\,|\,1,-1> + \,|\,1,1>)$ and $p_z = \,|\,1,0>$ [35] for both spin directions.[3] With the corresponding basis $\{p_{x\uparrow}, p_{y\uparrow}, p_{z\uparrow}, p_{x\downarrow}, p_{y\downarrow}, p_{z\downarrow}\}$ one gets:

$$H_{\mathrm{SOC},z} = \lambda \left(\begin{array}{ccc|ccc} 0 & i & 0 & 0 & 0 & 1 \\ -i & 0 & 0 & 0 & 0 & -i \\ 0 & 0 & 0 & -1 & i & 0 \\ \hline 0 & 0 & -1 & 0 & -i & 0 \\ 0 & 0 & -i & i & 0 & 0 \\ 1 & i & 0 & 0 & 0 & 0 \end{array}\right) \quad H_{\mathrm{SOC,y}} = \lambda \left(\begin{array}{ccc|ccc} 0 & 0 & i & 0 & i & 0 \\ 0 & 0 & 0 & -i & 0 & 1 \\ -i & 0 & 0 & 0 & -1 & 0 \\ \hline 0 & i & 0 & 0 & 0 & -i \\ -i & 0 & -1 & 0 & 0 & 0 \\ 0 & 1 & 0 & i & 0 & 0 \end{array}\right) \qquad (15)$$

The (2,6)-element of $H_{\mathrm{SOC},z}$, for instance, was calculated via $<p_{y\uparrow}\,|l_-|\,p_{z\downarrow}>$. The effect of these Hamiltonians on an unperturbed spin-degenerate system described by a Hamiltonian H_0 may be derived by calculating the new eigenvalues ϵ via $0 = \det(\epsilon \mathbb{1} - H_0 - H_{\mathrm{SOC}})$. This results in the same equation for both orientations of the SQA:

$$0 = ((\epsilon - \mathrm{E}_x)(\epsilon - \mathrm{E}_y)(\epsilon - \mathrm{E}_z) - \lambda^2(3\epsilon - \mathrm{E}_x - \mathrm{E}_y - \mathrm{E}_z) + 2\lambda^3)^2 \qquad (16)$$

with E_j as the energy of the unperturbed spin-degenerate p_j states. If all states have the same initial energy E, the eigenvalues of equation (16) are $E+\lambda$ (fourfold degenerate) and $E - 2\lambda$ (double degenerate). SOC is may therefore cause an asymmetric shift of the energy levels. However, if all states are occupied the total energy remains constant since $4 \cdot (\lambda) + 2 \cdot (-2\lambda) = 0$.

Since equation (16) defines the eigenvalues for an orientation of the SQA along the z-direction as well as the y-direction, the eigenvalues of the SOC Hamiltonian are independent on the orientation of the SQA if the states are spin-degenerate. Lifting the spin degeneracy is therefore necessary to observe an angular dependence of the total DOS on the orientation of the SQA. This is illustrated in chapter

---

[3] The usual notation $|\,l,m>$ is used, with l being the eigenvalue of the angular momentum and m the projection of the angular momentum on its orbital quantization axis.

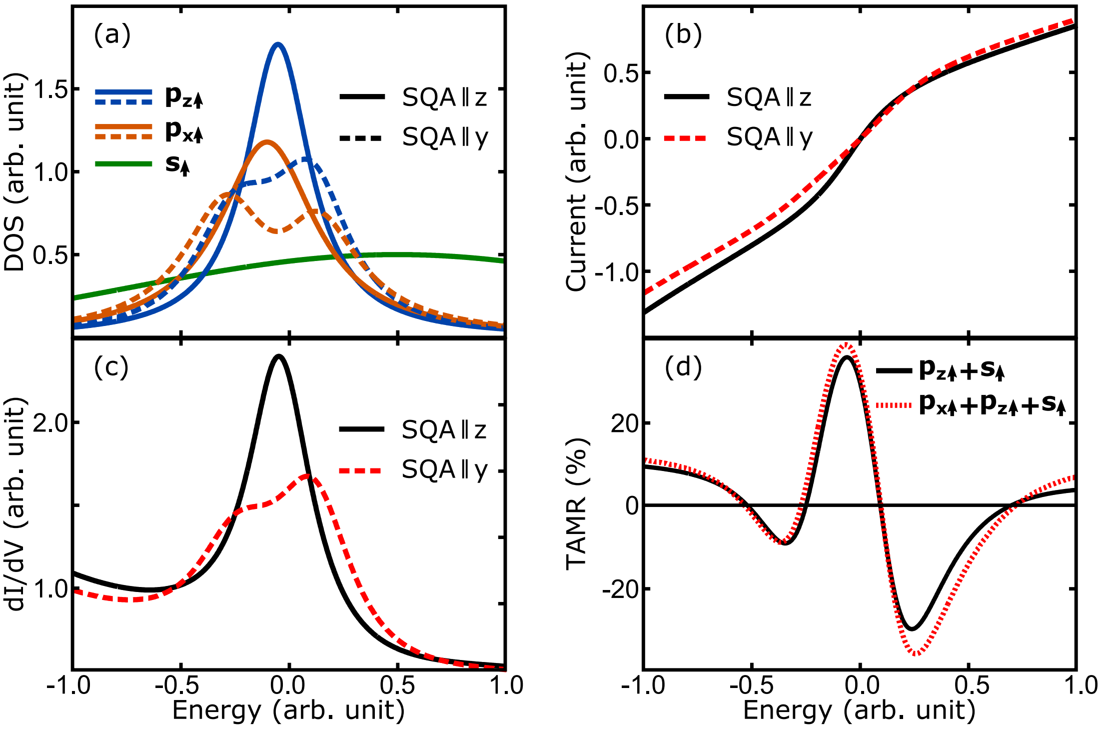

Figure 4. **SOC-induced hybridization of $p_{x\uparrow}$ and $p_{z\uparrow}$ states**

(a) DOS of the $p_{x\uparrow}$ $p_{z\uparrow}$ and $s_{\uparrow}$ states for an orientation of the spin-quantization axis (SQA) parallel to the z-axis (solid curves) and parallel to the y-axis (dashed curves), respectively, calculated via equations (12) and (13). The angular momentum is quantized along the z-direction. The $p_{x\uparrow}$ and $p_{z\uparrow}$ state hybridize for SQA ∥ y and split by an amount proportional to the spin-orbit parameter λ, which was set to 0.2 arb. unit. The $s_{\uparrow}$ state is independent on the orientation of the SQA. (b) Tunneling current calculated for a constant tip DOS and a sample DOS that is the sum of the $p_{z\uparrow}$ and the $s_{\uparrow}$ states from (a) via equation (1). (c) dI/dV curves calculated by deriving the curves in (b). (d) The solid curve is the TAMR calculated from the curves in (c) via equation (17). The dashed curves was calculated from dI/dV curves derived from a sample DOS consisting of the $p_{x\uparrow}$, $p_{z\uparrow}$ and $s_{\uparrow}$ states in (a).

11 (a) by calculating the DOS for SOC Hamiltonians with an arbitrary oriented spin-quantization axis [36–39]. Chapter **11 (a)** additionally shows that the SOC induced hybridization between the six p states may result in a very intricate behavior of the DOS. For simplicity, the effect of SOC on the DOS is illustrated here by only hybridizing the $p_{x\uparrow}$ state and the $p_{z\uparrow}$ state. The spin-degeneracy is thus lifted by omitting the $\downarrow$-states. The DOS is calculated using the Green's function method described in chapter **11 (a)**. Fig. **4** (a) displays the resulting DOS for an orientation of the SQA along the z-direction and the y-direction, respectively. The DOS of an $s_{\uparrow}$ state is considered additionally, which is unaffected by SOC due to its angular momentum being zero. This state therefore leads to a SOC independent background in the total DOS. Consequently, a SOC induced variation of the total DOS is less noticeable in this case. The $p_{z\uparrow}$ state remains an eigenstate for a SQA along the z-direction (see $H_{\mathrm{SOC},\,z}$ in equation (15)) and thus shows one Lorentzian peak in the DOS. For a SQA along the y-direction, however, the $p_{x\uparrow}$ and $p_{z\uparrow}$ states hybridize via SOC (see $H_{\mathrm{SOC},\,y}$ in equation (15)) and split by an amount proportional to λ. Note that this sequence is reversed if the p_x and p_z states have a different spin character, *i. e.,* $p_{x\uparrow}$ and $p_{z\downarrow}$ hybridize for the SQA along the z-direction and remain unchanged for the SQA along the y-direction.

How this splitting affects STM experiments is illustrated in the following. The tunneling current is determined by states that dominate in the vacuum. Consequently, the tunneling current shown in Fig. **4** (b) is calculated for a sample DOS consisting of the $p_{z\uparrow}$ state and the $s_{\uparrow}$ state from Fig. **4** (a). Fig. **4** (c) displays the corresponding dI/dV curves. The effect of SOC on dI/dV spectra may thus manifest itself in a variation of the amplitude of peaks accompanied by an energy shift. This was previously observed for single adatoms [25] and a ferromagnetic domain structure [24] and successfully described by SOC. In chapter **7** similar results for Pb dimers are presented. Indeed, dI/dV spectra are acquired over Pb dimers that are subjected to an in-plane and out-of-plane magnetization, respectively. The difference between the dI/dV curves is quantified by the tunneling anisotropic magnetoresistance (TAMR) [40] in Fig. **4** (d) via

$$\mathrm{TAMR} = 1 - \frac{\mathrm{d}I/\mathrm{d}V_{\mathrm{SQA}\,\|\,\mathrm{y}}}{\mathrm{d}I/\mathrm{d}V_{\mathrm{SQA}\,\|\,\mathrm{z}}}. \tag{17}$$

The TAMR for a DOS that consists of the $s_{\uparrow}$, the $p_{z\uparrow}$ and the $p_{x\uparrow}$ state is additionally shown in Fig. **4** (d). The differences between both TAMR indicate that the observed asymmetry is altered by adding states of different symmetries (here: $p_{x\uparrow}$) to the tunneling current. This may be achieved by decreasing the tunneling gap, which is shown in chapter **8** for atomic contacts involving single Ir and Co adatoms.

In conclusion, SOC mixes different states for different orientations of the spin-quantization axis with respect to the orbital quantization axis. This mixing, however, is not affecting the DOS unless the spin-degeneracy is lifted. The resulting dependence of the DOS on the orientation of the spin-quantization axis may be observed by comparing $\mathrm{d}I/\mathrm{d}V$ spectra of structures (*e. g.,* single atoms) with different alignments of their magnetization. Peaks in these spectra may change in amplitude and shift in energy due to the varying degree of hybridization. $\mathrm{d}I/\mathrm{d}V$ spectra are furthermore affected by the symmetry of the states contributing to the tunneling current because the SOC mediated hybridization between states depends on their symmetry. Changing the proportions of the states contributing to the tunneling current therefore results in a variation of the observed SOC dependence.

4. Fe bilayer on W(110)

The aim of this thesis is the study of atomic scale structures subjected to different magnetic environments. A suitable substrate for these experiments is the double layer Fe on W(110) because its domain structure is composed of areas with a magnetization normal to the surface (domains) as well as parallel to the surface (domain walls). Furthermore, this system has been subject of numerous studies focusing on its magnetic as well as its structural properties [24, 41–56]. These results turn the Fe bilayer into a perfect template to study magnetic properties of adsorbates, which is done in this thesis for single atoms and dimers. Similarly, previous studies investigates single molecules [57, 58] or single atoms [15, 25]. A short overview of the main properties of this system is given here.

Because of the high surface energy of W, the first layer of Fe covers the whole surface before single Fe islands start to grow in the second layer [41, 59, 60]. Both layers are pseudomorphic up to 1.5 monolayers [47], *i. e.,* the lattice constant of the Fe layers matches the W lattice constant, even though it is 10 % larger than the value for bulk Fe. This mismatch results in a high strain that is released by the formation of dislocation lines at coverages exceeding 1.5 monolayers [47], which are oriented along the [001] direction [55, 61].

Initially, the magnetic properties were investigated using spatially averaging techniques: They found that the magnetization direction of the Fe layers changes from in-plane in the first layer [62–64] to out-of-plane in the second layer [46, 65]. Later, spin-polarized STM studies refined these results by investigating the magnetic environment of the second Fe layer on the local scale: While small islands in the second layer are magnetized in-plane by the first layer, bigger islands are single domain particles with an out-of-plane magnetization [51]. Additionally, some large islands showed a domain wall. These walls appear far more frequently in larger Fe patches, which are attached to the W step edges when the crystal is heated to $\approx 500\,\mathrm{K}$ during Fe evaporation [49, 50, 52, 66]. The rotational sense of the spin in the domain wall remained unknown at first due to the lack of control over the orientation of the tip's magnetization direction in spin-polarized STM. While earlier studies assumed Bloch walls because of their reduced stray

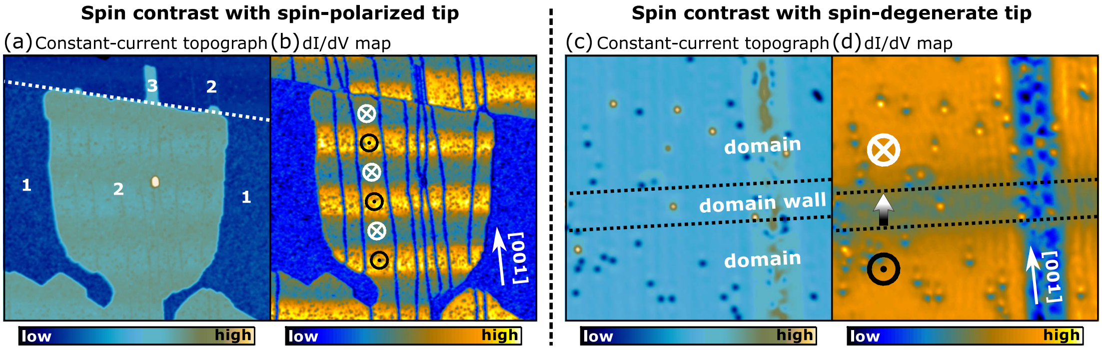
Spin contrast with spin-polarized tip
(a) Constant-current topograph (b) dI/dV map
Spin contrast with spin-degenerate tip
(c) Constant-current topograph (d) dI/dV map

Figure 5. **The domain structure of the second monolayer Fe on W(110).** (a) Constant current topograph and (b) dI/dV map recorded simultaneously with a Fe covered W tip (700 mV, 0.5 nA, $250 \times 250\,\mathrm{nm}^2$). The dashed line in the topograph indicates a step edge while the numbers $1, 2, 3$ denote the local coverage in monolayers. A large scale contrast of the second monolayer is visible in the dI/dV map. It is caused by the out-of plane spin-polarized domains, whose orientation is indicated by $\odot$ and $\otimes$. Note that the assignment of $\odot$ and $\otimes$ is arbitrary because of the unknown orientation of the out-of-plane component of the tip's magnetization. The vertical lines are dislocation lines, which are oriented along the [001] direction.
(c) Constant current topograph and (d) dI/dV map recorded simultaneously with a spin-degenerate W tip (70 mV, 0.5 nA, $30 \times 30\,\mathrm{nm}^2$). Single Ir atoms (defects) are visible as protrusions (depressions). The vertical line is, again, a dislocation line. The dI/dV map displays a horizontal stripe of reduced differential conductance, which is a domain wall [50]. While the orientations of the magnetizations are chosen arbitrarily, the domain wall is of Néel type, *i. e.,* its magnetization is orthogonal to the boundary between domain and domain wall [56].

field [50], measurements using a triple axes vector magnet to orient the tip's magnetic moment revealed the Néel character of the domain walls [56]. This was motivated earlier by calculations including the Dzyaloshinskii-Moriya interaction [67]. Surprisingly, the domain walls may even be observed with spin-degenerate W tips [24], because the magnetization directions on domains and domain walls are different and thus the local DOS is also different due to SOC (see chapter **3**). The main aspects of the Fe layer used in this thesis, namely its domain structure and the visibility of domain walls with non-magnetic tips, are shown in Fig. **5**.

5. Experimental details

All experiments presented in this thesis were done with a home-built scanning tunneling microscope operated at 4.5 K in ultrahigh vacuum (UHV) under a base pressure of 10^{-9} Pa. The UHV system consists of three connected chambers in total: a chamber for transferring tips and samples from atmospheric to low pressure, a chamber with a He-bath cryostat onto which the STM is mounted and a chamber for preparing single crystals and tips. In the preparation chamber tips and samples can be cleaned by heating via electron bombardment, sputtering with noble-gas ions and chemical reactions with gases introduced through a leak valve into the UHV system. While layers of metals can be grown by filament or electron beam evaporation in this chamber, single atom depositions are performed on samples held at low temperatures in the STM to prevent diffusion. A detailed description of the preparation procedure for the experiments presented on this thesis is given in the next chapter.

The STM is controlled with a SPM1000 electronic from *RHK Technology.* The tunneling current is amplified using a DLPCA-200 transimpedance amplifier from *FEMTO Messtechnik GmbH.* The differential conductance $\mathrm{d}I/\mathrm{d}V$ is recorded using Lock-In techniques. To this end the a sinusoidal modulation of usually 4 to 5 kHz is superimposed on the bias voltage using a SR830 Lock-In amplifier from *Stanford Research Systems.* While $\mathrm{d}I/\mathrm{d}V$ spectra were measured at a fixed tip height above the substrate and a modulation of $5\,\mathrm{mV_{rms}}$, $\mathrm{d}I/\mathrm{d}V$ maps were measured with a modulation of $20\,\mathrm{mV_{rms}}$ and at a constant current controlled with the feedback loop. Throughout this thesis the bias voltage is referenced with respect to the sample, *i. e.,* a positive (negative) voltage corresponds to a higher (lower) electric potential of the sample with respect to the tip.

(a) Sample and tip preparation

The main contaminations of the W crystal are carbon impurities that segregate from the bulk to the surface [68]. To remove them, the crystal is heated to 1500 K in an O_2 partial pressure of 10^{-6} Pa for 20 minutes. CO is formed and evaporates from the surface. Tungsten oxides are also generated but they are far more stable. They are removed by heating the crystal to 2200 K for a short period of time of ≈ 10 s. Since heating to these temperatures is not possible with standard UHV equipment, two new heating stations were built in the course of this thesis that could endure such high temperatures reliably. Their design is described in chapter **11 (c)**.

The Fe layers were grown by thermal sublimation of a 99.99 % pure Fe wire wrapped around a W wire. The evaporation rate was determined with a quartz balance. To induce a formation of large patches of Fe attached to the step edges the crystal was held at 500 K during evaporation [49, 50, 52, 66].

Single atoms were deposited on the crystal while it was mounted in the STM. This ensured a temperature of below 10 K during deposition of the single atoms. While Ir atoms were evaporated directly from a 99.8 % pure wire, Pb atoms were evaporated from a wire of 99.999 % purity that was suspended by a W filament.

W tips were electrochemically etched from a W wire of 0.25 mm diameter and 99.95 + % purity using a 2 mol/l NaOH solution. Fe(60 %)Cr(20 %)NiMn tips were electrochemically etched from a wire of 0.5 mm diameter using a 1 mol/l HCl solution. Residues on the tip apex were removed under vacuum conditions by short annealing and sputtering with Ar ions.

To get a spin-contrast in STM measurements, the tip needs a non-vanishing spin polarization, which is usually achieved by using (anti-) ferromagnetic materials for the whole tip or as layers deposited on a non-magnetic tip [9, 10]. For the spin-polarized measurements presented in this thesis, the second method is used by covering the tips with Fe *in-situ* by indenting the tip in the surface. The domain structure of the Fe layer (see chapter **4**) served to characterize the spin polarization of the tip.

(b) Tip and sample design for spin-polarized and AMR measurements

Although the experiments presented in this thesis probe different phenomena, they have a certain number of similarities. They, for instance, share the same substrate – the Fe bilayer on W(110) – and spin-polarized measurements and

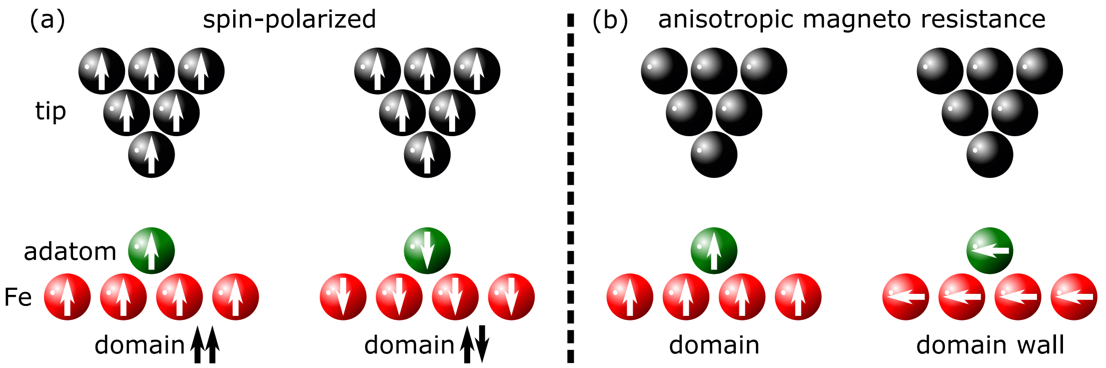

Figure 6. **Tip and sample magnetizations for the different experiments** (a) For spin-polarized measurements the tip needs a DOS with lifted spin-degeneracy and data on oppositely magnetized domains are acquired. (b) For measurements of the anisotropic magnetoresistance the tip has a spin-degenerate DOS and data on perpendicular magnetized domains and domain walls are acquired. For the sketches in (a), (b) a ferromagnetic coupling between adatom and Fe layer is assumed.

measurements related to anisotropic magnetoresistance (AMR) are both realized using similar adsorbates. However, the setups of these experiments fundamentally differ, which is illustrated in Fig. **6**.

The goal of spin-polarized measurements is to investigate spin-polarized properties of adsorbates and the ferromagnetic substrate. To this end a magnetic tip with a spin-split DOS is needed to measure $\mathrm{d}I/\mathrm{d}V$ spectra on oppositely magnetized structures (Fig. **6** (a)). The asymmetry of the $\mathrm{d}I/\mathrm{d}V$ curves is linked to the tip and sample spin polarization by the relation given in chapter **2**. This procedure is done in detail for single Ir adatoms in chapter **6** and for Pb dimers in chapter **7**.

The goal of AMR measurements is to observe and investigate the effect of spin-orbit coupling (SOC) on the (differential) conductance of adsorbates and the ferromagnetic substrate. However, SOC affects the DOS and thus the current of structures magnetized along the same axis (parallel or antiparallel) in the same way (see chapter **11 (a)**). Consequently, the effect of SOC can only be observed if structures with different spin-quantization axes are studied. This is done in this thesis by comparing data recorded on out-of plane magnetized domains with data recorded on in-plane magnetized domain walls and atomic structures adsorbed

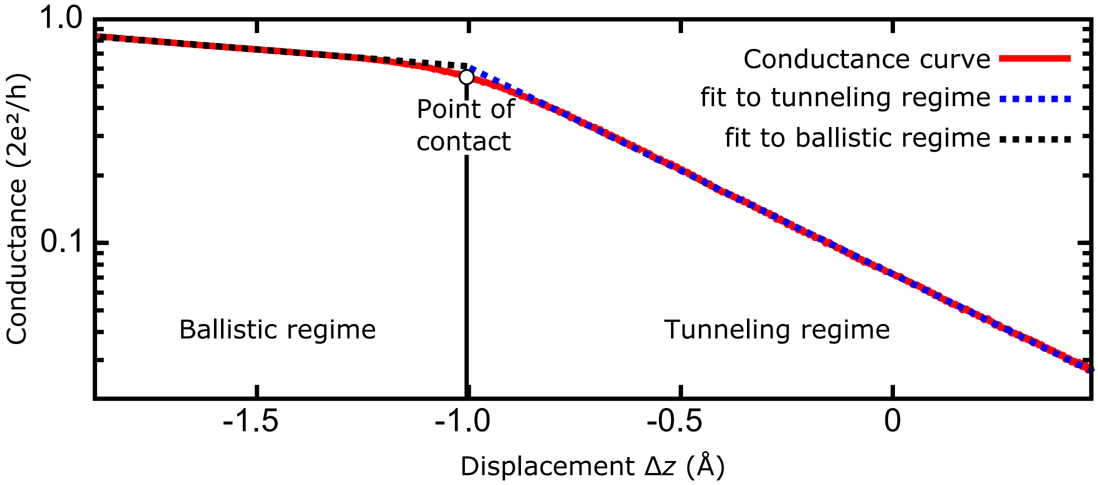

Figure 7. **Conductance curve**

The conductance of one Ir adatom is measured as a function of the tip displacement Δz relative to the adatom. $\Delta z = 0\,\text{Å}$ is defined by the parameters, at which the feedback loop was opened prior to the conductance measurement (100 mV, 0.5 µA). Two regimes of the conductance can be observed that are characterized by different slopes. These regimes are the tunneling regime ($\Delta z > -1\,\text{Å}$) and the ballistic regime ($\Delta z < -1\,\text{Å}$). The boundary is determined by the intersection of fits to both regimes. This intersection defines the point of contact (marked with $\circ$), which occurs at $0.56\,\mathrm{G}_0$ in this particular example.

on them, respectively (Fig. **6** (b)).

If the tip is spin-polarized the data is influenced by SOC and spin-polarized properties simultaneously. The DOS of the tip used for measurements of the AMR is therefore spin-degenerate to avoid the necessity of disentangling both effects afterwards. This procedure is used to measure the effect of SOC on the differential conductance of Pb dimers in chapter **7** and on the conductance of single Ir and Co adatoms in chapter **8**.

(c) Contact measurements

Controlled contacts may be formed with the tip of the STM to surfaces [69] or adsorbates like single molecules [70] or atoms [71] to study the transport of electrons on this scale. See Ref. [72] for an overview of this topic. Since contact measurements are performed in chapter **8** some general properties of them are discussed here.

If the dimensions of the contact are smaller than the mean free path of the electrons, they will pass ballistically through the junction [73]. Thus the contact regime will be referred to as ballistic regime. The contacts are formed by decreasing the tip-sample separation from the tunneling to the ballistic regime. In the tunneling regime the current and thus the conductance depends exponentially on the separation. Consequently, the conductance curve appears as a straight line on a logarithmic scale (Fig. **7**). A change of the slope of this line indicates the start of the ballistic regime. The conductance data of Ir adatoms that are presented in Fig. **7** and in chapter **8** show a smooth transition from the tunneling to the ballistic regime. For this case, the point of contact is defined by the intersection of fits to both regimes. Different atomic species, however, may exhibit different contact evolutions. Contacts to Au, for instance, are prone to show a jump to contact [74, 75], which is referred to as the transition regime (see Ref. [72]).

The total conductance G of a ballistic junction may be described with the Landauer-Büttiker model [76, 77]

$$G = G_0 \sum_j T_j. \tag{18}$$

T_j is the transmission probability of eigenchannel j and $G_0 = 2e^2/h$ [73]. Since $0 < T_j < 1$ the maximum conductance of one eigenchannel is G_0. G_0 is therefore called the quantum of conductance. However, the total conductance may be of a non-integer value of G_0 because the T_j are in general not unity. This is illustrated by the contact conductance of $0.56\,\mathrm{G_0}$ in Fig. **7**.

6. Distance- and energy-resolved spin-spectroscopy of Ir atoms

The contents of this chapter have been reproduced in part with permission from J. Schöneberg, N. M. Caffrey, P. Ferriani, S. Heinze and R. Berndt, Phys. Rev. B, **94**, 115418 (2016). *Copyright 2016 American Physical Society.*

The tunneling magnetoresistance (TMR) effect in magnetic multilayer junctions relies on the relative magnetization alignment of two ferromagnetic layers separated by an insulating barrier, an effect exploited in magnetic field sensors [4]. It originates from the spin-polarized density of states (DOS) of the electrodes and depends on the applied bias voltage and the electronic structure of the insulator, as well as its thickness [78–81]. The symmetry of the majority and minority electrons was shown to determine their decay rates within the barrier [82] and thus the spin-polarized tunneling current and the TMR.

The detailed dependence of the TMR effect on the width of the barrier can be difficult to assess using a typical multilayered device. This can be overcome by utilizing the spin-polarized tip of a scanning tunneling microscope (STM) as one electrode and the vacuum gap as the tunneling barrier between tip and the second electrode. In doing so, the energy and distance dependence of the spin-polarized signals can be studied in a controlled manner.

A distance dependence of the spin polarization was previously shown to occur above Ni tips tunneling to GaAs by inducing circularly polarized luminescence [83] and above clean ferromagnetic Co substrates by using an electromagnetic[4] tip [84] or Zeeman splitting in superconducting tips [85]. In contrast to these studies a new approach for distance-dependent measurements is employed here by using spin-polarized tips directly.

The energy dependence of the spin-polarized current was investigated for clean ferromagnetic surfaces [86–88] as well as for molecules [58, 89, 90] and single atoms [11–15] adsorbed on such surfaces. In some cases it was reported that the sign of the spin polarization above adatoms was inverted with respect to the underlying surface [15, 91]. Analogous to the mechanism in layered TMR

---

[4] An alternating current was passed through a coil wound around a magnetic tip.

devices, an orbital filtering effect of the vacuum tunneling barrier was suggested to be the source of this behavior [13, 15, 91, 92]. These studies found that, for $3d$ magnetic adatoms, minority d states tend to dominate at the adatom, with a much smaller contribution from majority s states. However, the d states decay much faster in the vacuum than the s states, with the result that the majority s states contribute primarily to the conductance in the vacuum. From this, it is evident that the sign of the spin polarization will be inverted at a certain tip-adatom separation. However, the distance dependence of the spin polarization above single adatoms has not been experimentally explored to date and several open questions remain. For example, Alvarado predicted that for bulk Ni tips on GaAs the largest change of the spin polarization will occur at large electrode separations [83], whereas other studies reported a rather constant rate of change of spin polarization with distance in this range [14, 85, 93].

Here, we experimentally investigate the energy and distance dependence of the spin polarization to determine at which electrode separation the transition to non-inverted spin polarization occurs. We find the sign of the spin polarization remains constant over a wide range of experimentally accessible tip-sample distances. This would suggest that the high density of minority d-states, known to be present at the adatom in an energy range around the Fermi level are not detected. Density functional theory (DFT) calculations are then used to determine which orbitals contribute to the tunneling current and to verify the proposed model of spin-dependent spatial decay of the orbitals [13, 91, 92]. We find that the d-states have decayed sufficiently at distances so close to the adatom that they are not accessible with a STM tip. Consequently, sp_z states determine the tunneling current at all tip-adatom separations. Moreover, the transition to non-inverted spin polarization is critically dependent on the electron energy.

Previous experiments mainly involved $3d$ elements, due to their high magnetic moments. Stable magnetic moments, however, may be expected for all atoms with partially filled shells. We use the $5d$ element Ir, in which a magnetic moment is induced by coupling to a ferromagnetic Fe bilayer on a W(110) surface.

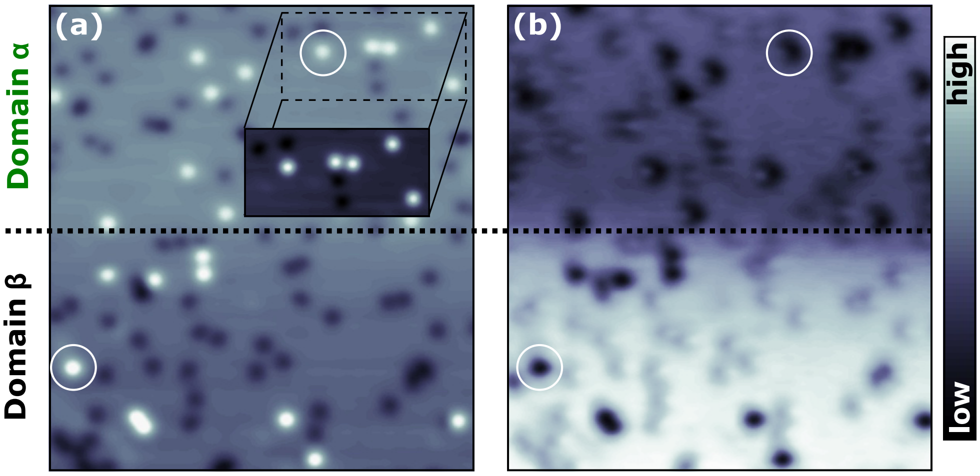

Figure 8. **Ir atoms adsorbed on the domain structure of the Fe bilayer** (a) Topograph (700 mV, $32 \times 35\,\mathrm{nm}^2$) of Ir atoms adsorbed on magnetic Fe domains measured with a spin-polarized tip. Single Ir atoms are readily distinguishable as protrusions, which is further illustrated by the inset (1 V) where the color scale has been adjusted. Defects of the Fe layer appear as depressions. (b) $\mathrm{d}I/\mathrm{d}V$-map recorded simultaneously with the topograph (a). At the applied sample voltage of 700 mV the $\mathrm{d}I/\mathrm{d}V$ signal varies on a large scale that stems from differently spin-polarized magnetic domains. Since the magnetic domains are polarized out-of-plane [49], this variation of the signal directly reflects out-of-plane spin sensitivity of the tip. The boundary between both domains is indicated by the dashed line. Note, that a domain wall is present close to this line but it may not be distinguished at the applied bias voltage. For further evaluation we refer to domains with lower (higher) $\mathrm{d}I/\mathrm{d}V$ signal at 700 mV by using α (β) as index. Atoms are indexed according to the domain they are adsorbed on. The positions of two Ir atoms adsorbed on differently polarized Fe domains are indicated by circles in (a) and (b).

(a) Methods

Single Ir atoms were deposited onto the Fe bilayer on W(110) at ≈ 10 K and appear as protrusions in constant current topographs (Fig. 8 (a) and inset). Information on the spin polarization is gained by spectroscopy of the differential conductance ($\mathrm{d}I/\mathrm{d}V$) using spin-polarized tips, which were fabricated by covering non-magnetic W or stainless steel tips with Fe *in-situ*. The existence of an out-of-plane spin polarization was verified by analyzing the contrast between the magnetic Fe domains in dI/dV maps at 700 mV (Fig. **8** (b)).

DFT calculations are performed using the VASP code [94, 95]. Structural relaxations are performed using the revised Perdew-Burke-Ernzerhof [96] parametrization of the generalized gradient approximation while the electronic structure was determined within the local spin density approximation using the Perdew-Zunger [97] parametrization of the Ceperley-Alder data [98]. The projector-augmented wave (PAW) method [99] is used with the standard PAW potentials supplied with the VASP distribution. The plane wave basis set is converged using a 450 eV energy cutoff. Structural relaxations are carried out using a 17 × 24 × 1 k-point Monkhorst-Pack mesh [100] to sample the three-dimensional Brillouin zone. The vacuum DOS was determined by positioning an empty sphere at the required height directly above the adatom onto which the DOS was projected. The system is modeled using a symmetric slab consisting of five atomic layers of W with two monolayers of Fe on each side. The experimental lattice constant of W was used ($a_0 = 3.165$ Å). The adatom was added on each Fe surface in the hollow-site position. The minimum distance between the adatoms in adjacent unit cells is 6.33 Å so that any interaction between them will be negligibly small. Additionally, a thick vacuum layer of approximately 21 Å is included in the direction normal to the surface to ensure no spurious interactions between repeating slabs. The positions of the Fe atoms as well as the adatom are optimized until all residual forces are less than 0.01 eV/Å.

The spin polarization P is defined as:

$$P = \frac{n_{\mathrm{maj}} - n_{\mathrm{min}}}{n_{\mathrm{maj}} + n_{\mathrm{min}}} \tag{19}$$

with n_{maj} and n_{min} as the majority and minority local DOS (LDOS), respectively. It is not possible to experimentally measure directly the LDOS, as it is coupled with the DOS of the tip, and instead we refer to the conductance asymmetry, A, which is defined as [9, 10]:

$$A = \frac{(\mathrm{d}I/\mathrm{d}V)_\beta - (\mathrm{d}I/\mathrm{d}V)_\alpha}{(\mathrm{d}I/\mathrm{d}V)_\beta + (\mathrm{d}I/\mathrm{d}V)_\alpha} \tag{20}$$

where $(\mathrm{d}I/\mathrm{d}V)_{\alpha,\beta}$ refer to dI/dV spectra taken on structures α and β (Fe domains or Ir atoms) with opposite magnetizations (see Fig. **8**). According to the derivation presented in chapter **2**, the conductance asymmetry $A_{\mathrm{Fe,Ir}}$ for Fe domains and Ir adatoms reads

$$A_{\mathrm{Fe,Ir}} = P_{\mathrm{Fe,Ir}} \cdot P_{\mathrm{T}} \tag{21}$$

with P_{Fe} (P_{Ir}) as the spin polarization of the Fe domains (Ir adatoms) and P_{T} as the spin polarization of the tip. In order to extract $P_{\mathrm{Fe,Ir}}$ from the experimental data, $\mathrm{d}I/\mathrm{d}V$ spectra must be measured at the same tip-substrate separation in both the α and β domain [101]. However, the apparent heights of domains and adatoms are usually different for different domains. To refer to the same absolute height we corrected for these differences [15, 101], which is further explained in chapter **11 (b)**. The largest challenge in interpreting the $\mathrm{d}I/\mathrm{d}V$ spectra of Ir is the unknown spin polarization P_{T} of the tip, which is usually energy dependent and may be affected by tip modifications [92, 102]. We therefore use established results from Fe domains [15, 24], to deduce properties of the tip through a comparison of experiment and theory.

(b) Energy dependence

Fig. **9** (a) shows $\mathrm{d}I/\mathrm{d}V$ spectra measured above oppositely magnetized Fe domains. Two prominent peaks at -60 and $720\,\mathrm{mV}$ due to d_{z^2} minority states [15, 24] are present on both domains. They are reproduced by peaks at $-200\,\mathrm{mV}$ and $800\,\mathrm{mV}$ in the calculated minority vacuum LDOS (Fig. **9** (b)). As the peaks are observed in the $\mathrm{d}I/\mathrm{d}V$ signals from both domains, this implies that the tip is only partially spin-polarized. Consequently, $(\mathrm{d}I/\mathrm{d}V)_{\alpha,\beta}$ should not directly be compared to $n_{\mathrm{maj,min}}$. However, information about P_{T} can be deduced from the vanishing of the asymmetry of the Fe domains at $V = -140$ and $630\,\mathrm{mV}$ (Fig. **9** (e)). According to equation (21) this can only occur if $P_{\mathrm{T}} = 0$ or $P_{\mathrm{Fe}} = 0$. Since our calculations and previous results show that $P_{\mathrm{Fe}} < 0$ for the considered energy range (Fig. **9** (f)), P_{T} has to vanish at these voltages. Consequently, we divided the voltage scale into three region I, II and III. For voltages below $-140\,\mathrm{mV}$ (region I) and above $630\,\mathrm{mV}$ (region III) $A_{\mathrm{Fe}} > 0$ (Fig. **9** (e)) and $P_{\mathrm{Fe}} < 0$ (Fig. **9** (f)). According to equation (21), $P_{\mathrm{T}} = A_{\mathrm{Fe}}/P_{\mathrm{Fe}} < 0$ at these voltages, *i. e.,* the tip is more sensitive to minority states (see equation (19)). Between these two

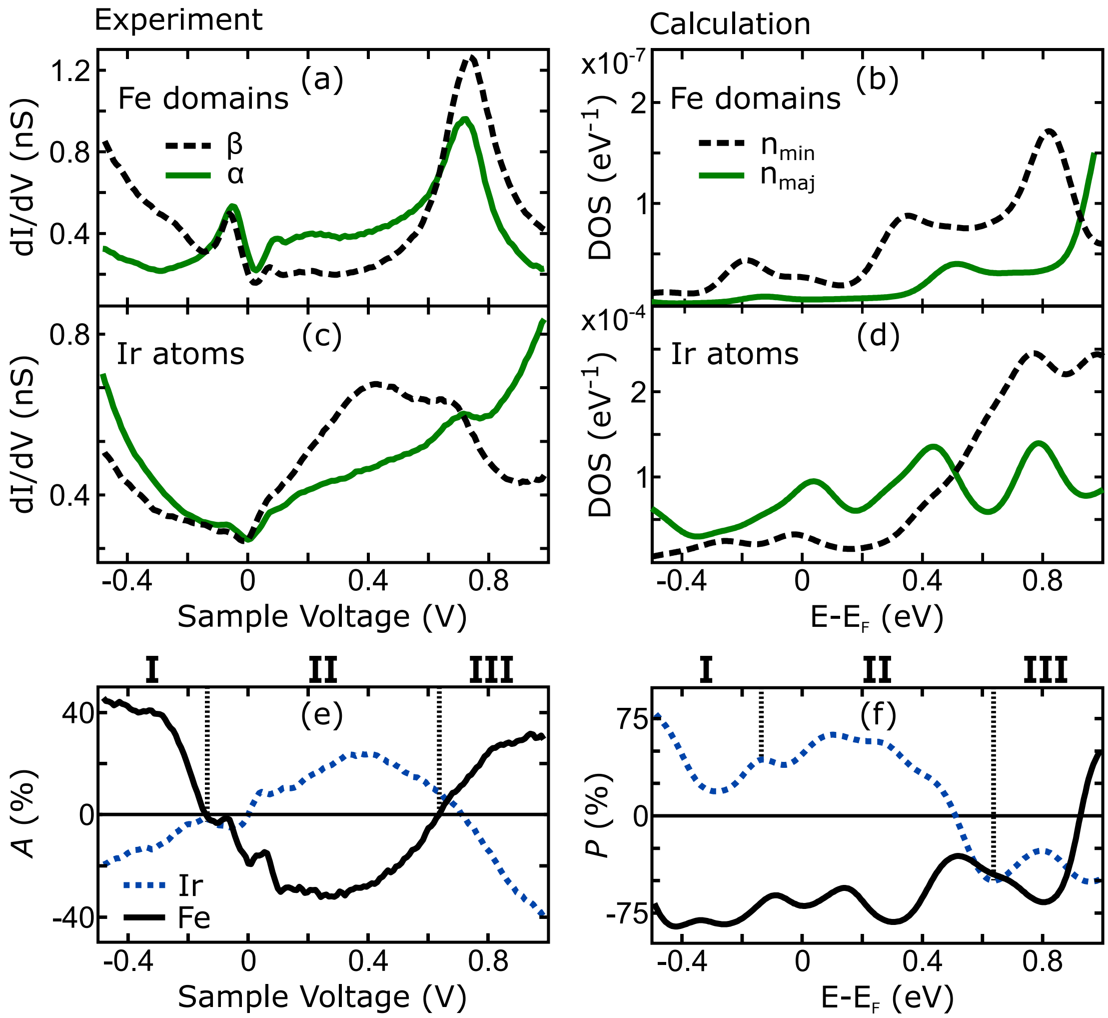

Figure 9. **Spin-polarized dI/dV spectra and spin-polarized DOS** Spin-polarized dI/dV spectra of Fe domains (a) and Ir atoms (c). For the definition of α, β please refer to Fig. **8**. (b) Majority (n_{maj}) and minority (n_{min}) vacuum densities of states 8.6 Å above the hollow site of the Fe surface and (d) 5 Å above the Ir atom, respectively. A one-to-one correspondence between the dI/dV curves and n_{maj} or n_{min} may not be expected as the tip is only partially spin-polarized. (e) Experimental asymmetries A of Fe domains and Ir atoms adsorbed on the Fe domains calculated from the dI/dV curves in (a), (c) via equation (20). (f) Corresponding calculated spin polarizations P from n_{maj} and n_{min} in (b), (d) via equation (19). Comparison of (e) and (f) in combination with equation (21) suggests that the spin polarization of the tip changes sign between regions I, II and III. In the regions I and III the tip is more sensitive to minority states while for region II majority electrons prevail.

voltages (region II) $P_\mathrm{T} > 0$, *i. e.,* majority electrons prevail.

Using this information, we can interpret the Ir data, presented in Fig. **9** (c), as follows: States appear on β-atoms at 410 and 640 mV, whereas α-atoms show a resonance at 710 mV on an monotonously increasing background. The absence of other signatures shows that the state observed at β-atoms at 410 mV is largely dominated by one spin channel. Because the tip is more sensitive to majority electrons at this energy, we identify this peak as being the state in the majority channel at 400 meV in the spin-polarized vacuum LDOS (Fig. **9** (d)), which is predominantly of sp_z character (see Fig. **10** (a)). This state is not present in the minority channel, apart from a small shoulder, in agreement with the experimental observations. The experimental peaks at 640 mV and 710 mV are reproduced by the peaks in n_maj and n_min at 750 mV.

Due to the vanishing spin polarization of the tip, A_Ir vanishes at similar voltages as A_Fe (Fig. **9** (e)). Surprisingly, the signs of both asymmetries are different over almost the whole voltage range of -0.5 V to 1 V, suggesting that Ir is polarized oppositely to the Fe surface. This interpretation is supported by the spin polarizations calculated via the vacuum LDOS (Fig. **9** (f)). For energies between -500 and 500 meV, Ir predominantly exhibits majority states while Fe displays minority states. The vacuum spin polarization reverses sign at an energy of 500 meV as a result of the large increase in the minority p_z states. The agreement between experimental and theoretical results is less favorable for voltages exceeding 500 meV. We attribute the deviation to limitations of equation (21), which is derived assuming a low bias voltage (see chapter **2**).

At a sample voltage of 370 mV the conductance asymmetry of Ir reaches an extremal value of 25 %. To determine the corresponding value of P_Ir the spin polarization of the tip at this voltage is extracted from the Fe data (Fig. **9** (e), (f)) using equation (21) via $P_\mathrm{T} = A_\mathrm{Fe}/P_\mathrm{Fe} = 40\,\%$. This value is similar to the previously used value of 44 % [86, 87], which is based on the spin polarization of Fe in planar junctions [103]. Consequently, the Ir spin polarization, given by $P_\mathrm{Ir} = A_\mathrm{Ir}/P_\mathrm{T}$, is 63 %. This is of the same order of magnitude as reported for Co atoms [15] and agrees well with the theoretical value in Fig. **9** (f).

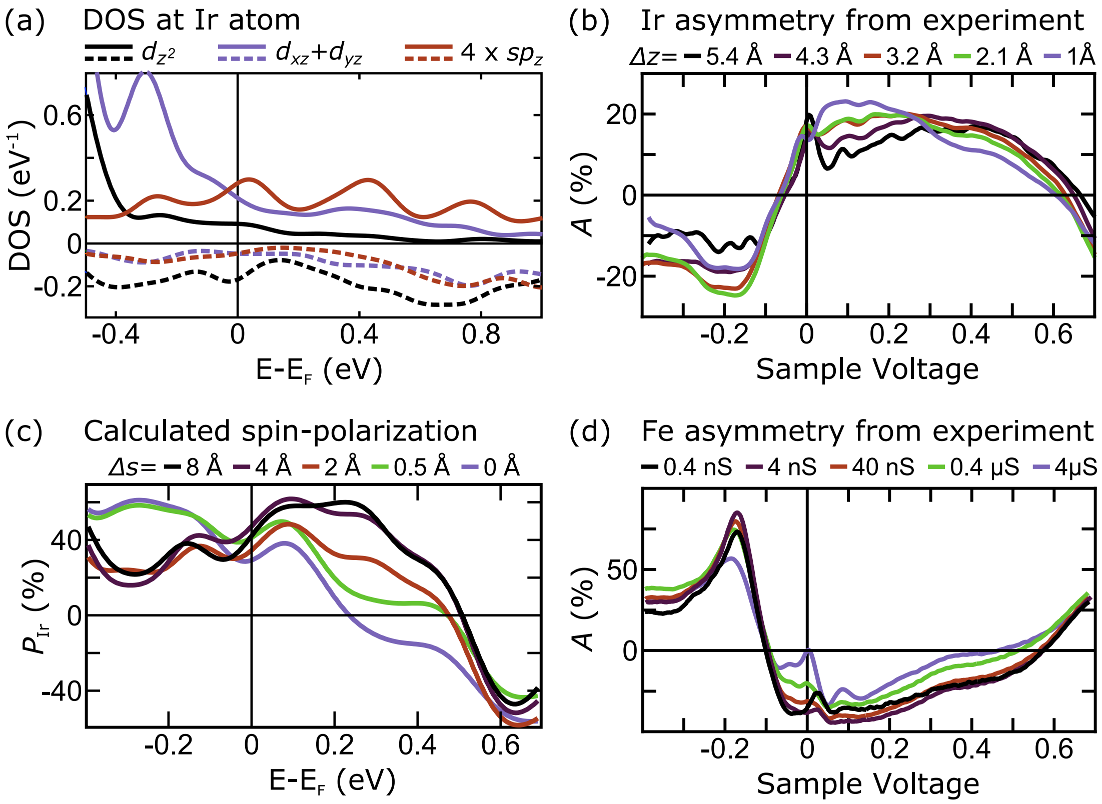

Figure 10. **Calculated and measured distance dependence of the spin polarization and conductance asymmetry**

(a) Orbital decomposition of the Ir DOS calculated with VASP. Majority (minority) states are represented as positive (negative). The sp_z state was multiplied by 4. (b) Asymmetries of single Ir atoms measured with a spin-polarized tip at conductances ranging from 0.4 nS to 4 μS, which correspond to distances Δz of 5.4 Å to 1 Å from the formation of the single-atom contact at $\approx 35\,\mu$S (see chapter **6 (d)** on the details of this conversion). (c) spin polarization of single Ir atoms at different distances Δs into the vacuum calculated via DFT using VASP. $\Delta s = 0$ Å is at the center of the Ir atom. (d) Asymmetries of the bare Fe surface measured with the same tip as in (b) and at the same conductances. A conversion to a distance scale is not done because the point of contact to the Fe surface was not determined (see text for details).

(c) Distance dependence

Fig. **10** (a) shows the DOS of the Ir adatom projected onto the sp_z, d_{xz}+d_{yz} and d_{z^2} states. The majority states are dominated by the d_{xz}+d_{yz} state. In particular, there is a large peak in the $d_{xz}+d_{yz}$ DOS at $-300\,\mathrm{meV}$. However, this peak is not visible in $\mathrm{d}I/\mathrm{d}V$ curves (Fig. **9** (c)) and the vacuum DOS (Fig. **9** (d)), with the implication that this state decays quickly in the vacuum. In fact, the peaks visible in $\mathrm{d}I/\mathrm{d}V$ spectra (see Fig. **9** (c)) and in the vacuum DOS at $50\,\mathrm{meV}$, $400\,\mathrm{meV}$ and $750\,\mathrm{meV}$ correspond to peaks in the majority sp_z DOS at the adatom. This suggests that the sp_z state, despite its smaller DOS at the adatom, decays slowly and eventually dominates in the vacuum over the faster decaying $d_{xz}+d_{yz}$ state. The minority DOS at the adatom, on the other hand, is dominated by d_{z^2} states in a wide energy region around the Fermi level, with a small peak just below the Fermi level and a larger broad peak at $700\,\mathrm{meV}$. The magnitude of the sp_z state in the same energy region is considerably smaller. In total, d states will dominate at distances very close to the adatom while sp_z states will prevail with increasing tip height, *i. e.,* the vacuum gap acts as an orbital filter.

This filter influences the spin polarization. Consider, for instance, the preponderance of the minority states at the adatom at certain energies above the Fermi level. In contrast, the conductance asymmetry (Fig. **9** (e)) and the calculated spin polarization in the vacuum $5\,\text{Å}$ above the adatom (Fig. **9** (f)) show a large positive spin polarization above the Fermi level, *i. e.,* majority electrons dominate. Consequently, the vacuum gap changes the amplitude of the observed spin polarization and may even induce a sign inversion at a certain separation between tip and adatom. The DOS at negative energies, however, is dominated by the majority $d_{xz}+d_{yz}$ state at the adatom and by the majority sp_z state in the vacuum, *i. e.,* the sign inversion with respect to the negatively spin-polarized surface occurs directly at the adatom and so will not be experimentally observable.

To further characterize the distance dependence of the filtering effect, and to determine whether an inversion of the spin polarization can be observed at any energy, we measured the asymmetry A_{Ir} for several conductances, which correspond to different tip-adatom separations. Fig. **10** (b) shows A_{Ir} measured using the same tip at conductances ranging from $0.4\,\mathrm{nS}$ to $4000\,\mathrm{nS}$. As a comparison the asymmetry A_{Fe} of the Fe layer is measured at the same conductances (Fig. **10** (d)). The conductances of the Ir adatom are converted to distances to enable better comparison with the calculations. $\Delta z = 0\,\text{Å}$ is defined as the point of contact that occurs at a conductance of $\approx 35\,\mu$S. Measurements in contact were not feasible due to junction instabilities at the elevated voltages used for recording dI/dV curves. The conversion yields that A_{Ir} was recorded at distances Δz of 5.4 Å to 1 Å prior to formation of the single-atom contact (see chapter **6 (d)** on the details of this conversion). A similar conversion could not be done for A_{Fe} because the point of contact was not determined since contacts to bare surfaces are less reproducible than to adsorbates [104, 105].

The Ir and Fe conductance asymmetries change sign at similar voltages as before due to the varying spin polarization of the tip as a function of energy. Additionally to this energy dependence P_{T} will also be distance dependent and thus will influences the magnitude of the asymmetry at different tip-adatom separations. Nonetheless, the sign and the overall shape of A_{Ir} remain essentially similar over the entire range of 4.4 Å. Its inversion with respect to the Fe layer and thus the dominance of the majority spin states is furthermore supported by A_{Fe} that also remains essentially unaltered. This is in agreement with the calculated spin polarizations of Ir at different distances Δs from the atomic core. The magnitude of P_{Ir} saturates at 4 Å (Fig. **10** (c)).[5]

It is also consistent with previous calculations of an approximately constant spin polarization for Co and Ni atomic contacts in this range [93]. It is therefore clear that the inversion of the spin polarization occurs at distances too small to be probed by this method.

The calculated spin polarization at heights of 0 Å, 0.5 Å and 2 Å above the adatom (Fig. **10** (c)) show that the length scales at which such inversions occur are indeed very small. At the atom (0 Å) P_{Ir} is negative between 250 meV and 470 meV. By a height of 0.5 Å above the atom, this is already inverted, due to the majority sp_z state at 400 meV (Fig. **10** (a)). The decreasing influence of the $d_{xz}+d_{yz}$ state with increasing height is particularly evident at -300 meV. Here, it is clear that the large peak in the majority $d_{xz}+d_{yz}$ state (Fig. **10** (a)) influences the spin polarization at distances very close to the adatom; a large polarization of $+60\,\%$ is found for distances less that 1 Å from the atom. By 2 Å from the adatom, however, the effect of this majority state is negligible. This is in agreement with

---

[5] Assuming that the single atom contact occurs at the next-neighbor distance of Ir (2.7 Å), the experimental distance $\Delta z = 1$ Å corresponds to the theoretical distance $\Delta s = (1+2.7)$ Å $= 3.7$ Å.

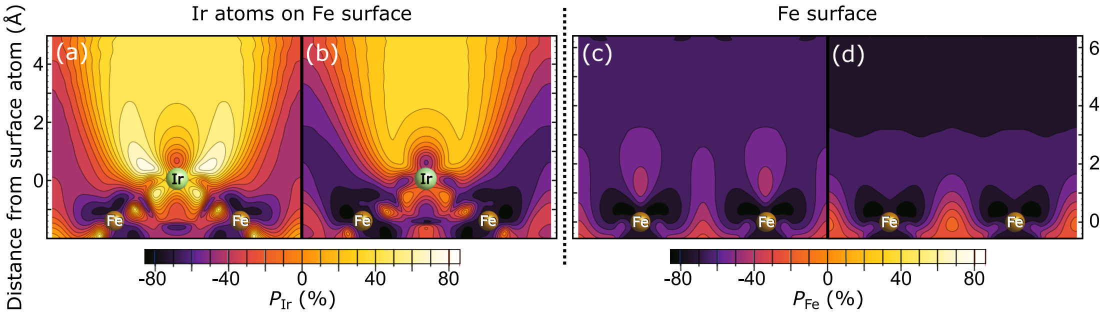

Figure 11. **Spatial dependence of the spin polarization**

Spatial dependence of the spin polarization of the Ir adatom (a, b) and the bare second Fe layer on W(110) (c,d) integrated over the energy intervals $[-50\,\mathrm{meV}, 50\,\mathrm{meV}]$ (a, c) and $[300\,\mathrm{meV}, 400\,\mathrm{meV}]$ (b, d).

previous results from single adatoms [14] and with the results presented in chapter **8**, which showed that additional orbitals contribute to the conductance at contact. Finally, Fig. **11** (a, b) shows slices of the spin polarization above an adsorbed Ir atom, where the spatial distribution of the spin polarization can be seen more clearly. As a comparison, we also show the evolution of the spin polarization above a clean Fe surface in Fig. **11** (c, d). For the clean surface, the spin polarization is a constant negative value over a wide range of energy and distance. In contrast, directly above the adatom the spin polarization changes sign rapidly. Close to the Fermi energy (Fig. **11** (a)) the negative spin polarization of the clean surface is inverted directly at the Ir adatom, due to the majority $d_{xz} + d_{yz}$ state. Far from the adatom, the spin polarization remains positive, but is now carried by states with sp_z symmetry. In contrast, at energies between 300 meV and 400 meV (Fig. **11** (b)), and very close to the adatom, the spin polarization is negative due to the influence of a minority d_{z^2} state. However, with increasing height, the influence of this state wanes and the positive spin polarization associated with the sp_z state begin to dominate with an associated inversion of sign. This inversion occurs at distances less than 0.5 Å from the adatom, and so is not experimentally accessible.

In conclusion, Ir, which is paramagnetic as a bulk material, exhibits a spin polarization of similar magnitude as the well-studied $3d$ elements. The tunneling current to unoccupied states exhibits a large spin polarization of more than 60 %

that is inverted with respect to the underlying Fe layer. Distance-dependent measurements along with DFT calculations show that the spin polarization remains stable over a wide range of tip-adatom separations. The calculations relate this behavior to an orbital filtering of the tunneling gap between tip and adatom. This filtering happens over a distance of less than 4 Å from the atomic core.

(d) Appendix: Conversion of the conductance to the distance scale

In the previous chapter the asymmetry of Ir adatoms was measured at different conductances corresponding to different tip-adatom separations Δz. For better comparison with the theory the conductances have been converted to Δz. The procedure for conversion is discussed here. The conductance G depends exponentially on the tip-adatom separation in the tunneling regime

$$G(\Delta z) = G_{\mathrm{contact}} \exp(-2\,\kappa\,\Delta z). \tag{22}$$

κ is the decay constant (see equation (2)) and G_{contact} is the conductance at the point of contact (cf. chapter **5 (c)**). The point of contact is defined to occur at $\Delta z = 0\,\text{Å}$ by equation (22). Experimentally, the tip-adatom separation decreases by 1.1 Å if the conductance is increased by a factor of ten. This results in a decay constant of $\kappa = 1.05\,\text{Å}^{-1}$.

$G_{\mathrm{contact}} = 35\,\mu\mathrm{S}$ was determined by conductance curves at 50 mV and 100 mV with spin-polarized tips. The separation Δz at a conductance G can be retrieved by converting equation (22) to

$$\Delta z(G) = \frac{1}{2\,\kappa} \ln(G_{\mathrm{contact}}/G). \tag{23}$$

At a conductance of $G = 4\,\mu\mathrm{S}$ the tip is thus $\Delta z(4\,\mu\mathrm{S}) = 1.04\,\text{Å}$ away from the formation of the single-atom contact. G_{contact} may differ at a voltage of 0.8 V, which was used to stabilized the tip prior to the $\mathrm{d}I/\mathrm{d}V$ measurements. However, while G_{contact} may vary with the voltage, the interpretation given in the previous paragraph is not critically affected. A 50 % larger G_{contact}, for instance, would result on a shift of the Δz scale by only 19 pm.

7. Tunneling anisoptropic magnetoresistance of Pb dimers

Spin-orbit coupling (SOC) leads to magnetic anisotropies in bulk materials. Indeed, SOC modifies the energy needed to tilt the magnetization with respect to the crystallographic structure. Albeit being a small effect, prominent examples like the magnetocrystalline anisotropy (MA) and anisotropic magnetoresistance (AMR) originate from SOC. MA is a key quantity to stabilize magnetic moments, which is important in mass storage devices. Consequently, with the goal of miniaturization, numerous studies investigated MA on the level of single atoms [16–21].

AMR describes the change in the electrical resistance for a current passing through a ferromagnetic electrode for different magnetization directions and is thus used in magnetic field sensors. While the resistance varies by $\approx 3\,\%$ in bulk systems [106], it can be largely enhanced in tunneling devices on the atomic scale to values on the order of several $10\,\%$ [25, 107–111]. This tunneling AMR (TAMR) may thus reach similar values as the giant magnetoresistance.

Since TAMR is intrinsically linked to SOC, an increase of the TAMR may be achieved by tuning SOC with the use of appropriate atomic species, *i. e.,* heavy atoms with large orbital moments [110]. However, SOC causes TAMR by hybridizing orbitals and the orbital structure may be influenced much larger by modifying the coupling between the atoms comprising the junction. To date it remains unclear how the TAMR of atomic structures is affected by their environment.

So far the TAMR on the atomic scale was only investigated for single Co adatoms with the STM [25] by measuring $\mathrm{d}I/\mathrm{d}V$ curves, which are determined by the DOS and thus states of the sample, which are hybridized via SOC. The atomic environment can be readily addressed and modified with an STM [7, 112]. Using this technique the importance of the atomic environment was shown for inelastic spin excitations of atoms adsorbed on surfaces. These excitations are altered by the adsorption site of the atom [113], (in)direct exchange between atoms [23, 114–117] or by the modifications atoms induce in the substrate layer [118]. Similar dependencies may also occur for the TAMR of structures on the atomic scale but presently little is known about this. Here, we address this issue by showing that the TAMR of Pb dimers, which are built with the STM, critically depends on the coupling between the atoms.

(a) Formation and orientation of Pb dimers on the Fe bilayer

In order to build atomic structures, atomic manipulation with the STM tip was performed. The tip exerts forces on the atom that weaken the bond of the atom to the surface. These forces have an electrical contributions due to the applied bias voltage and a chemical contribution due to the interaction between tip and adatom that occurs from the overlap of their orbitals [112, 119]. Consequently, the strength of the forces is controlled by changing the tunneling parameters, *i. e.,* the bias voltage and the current and thus the resistance of the junction. Tunneling resistances needed to move metallic atoms are on the order of 20 kΩ to 400 kΩ [119, 120] in contrast to resistances on the order of GΩ that are typically used to acquire constant-current topographs. The spread of the parameters illustrates that the force required for manipulation drastically changes for different adsorbate-substrate combinations due to different bonding strengths [121]. Since the chemical forces are determined by the orbital overlap between tip and adatom, variations of the orbital structure of the tip additionally influence these parameters.

Here, dimers were built from single atoms. In a first attempt Ir atoms were used. Even though the resistance was reduced down to 10 kΩ (100 mV, 10 µA) the lateral position of the atoms remained unchanged. Higher voltages resulted in transfers of the adatom from the surface to the tip. The robustness of the Ir atom supposedly originates from a strong hybridization with the Fe layer. This may be caused by the chemical similarity of Ir and Fe because both are *d*-elements in the groups 8 and 9 of the periodic table, respectively.

A reduced hybridization may be expected for a chemically different atomic species. Additionally, a chemical element with a large mass is preferable since it results in a large SOC and thus may increase the TAMR. The 6*p*-element Pb is used here because it fulfills these requirements and is furthermore known to evap-

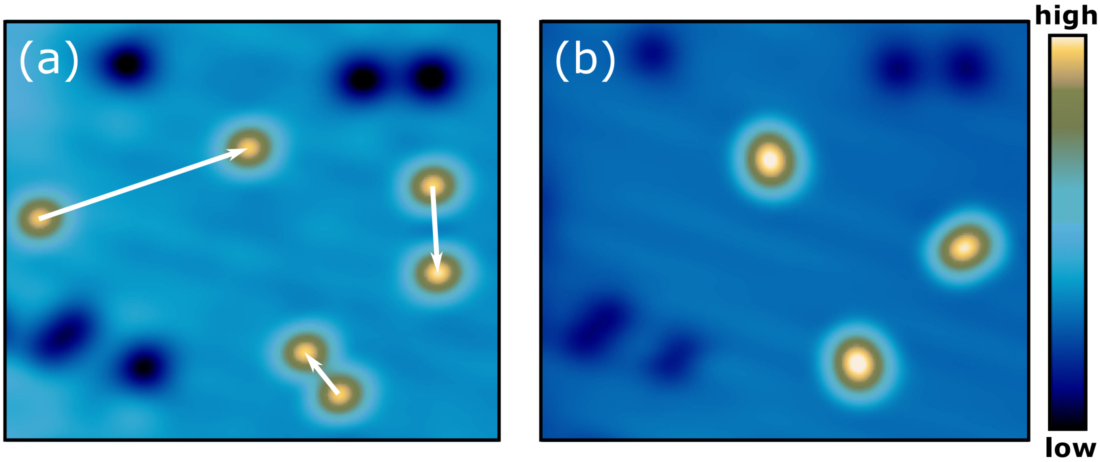

Figure 12. **Building of Pb dimers**

(a) Constant-current topograph ($6.6 \times 9\,\mathrm{nm}^2$, 100 mV) showing six single Pb atoms adsorbed on the second layer Fe on W(110). They appear as protrusions whereas defects of the layer appear as depressions. The tip of the STM was used to move the Pb atoms as indicated by the arrows. For this purpose the tips was first placed next to the atom and then the tunneling resistance was decreased to 25 kΩ (100 mV, 4 µA). At these parameters the atom was pushed across the surface by the tip and its new position was determined with a subsequently recorded constant-current topograph at a high resistance, *i. e.,* large tip-sample separation. (b) Moving the atoms resulted in the formation of three dimers with two different orientations ($7 \times 9\,\mathrm{nm}^2$, 1 V).

orate easily due to its low melting point. In earlier experiments Pb dimers were furthermore successfully built on Cu(211) [120]. Fig. **12** (a) displays six Pb atoms adsorbed on the Fe bilayer on W(110). These atoms were moved at a tunneling resistance of 25 kΩ (100 mV, 4 µA) to build three dimers (Fig. **12** (b)). Dimers with different orientations were successfully formed. To determine the adsorption geometries of the dimers, an atomically resolved constant-current topograph of the Fe layer was recorded at a high conductance of $0.92\,\mathrm{G}_0$ (Fig. **13** (a)). The positions and spacings of the Fe atoms are marked and superimposed on differently oriented Pb dimers under the assumption of the Pb atoms being adsorbed on the hollow sites of the Fe surface (Fig. **13** (b)). The dimers are oriented along the [001] and $[1\bar{1}1]$ direction, respectively. Because the Fe layer is pseudomorphic [47] the spacing of the Pb atoms in the dimers is given by the lattice constant

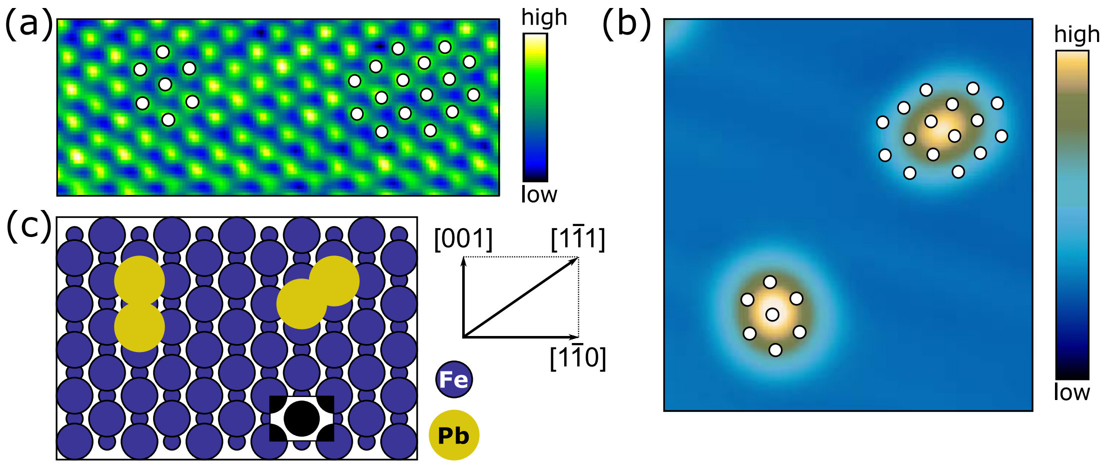

Figure 13. Dimer orientation on the Fe lattice

(a) Constant current topograph with atomic resolution ($4.7 \times 1.9\,\mathrm{nm}^2$, 70 mV, 5 µA). The structure of the bcc(110) Fe surface is marked by dots. (b) The dot structures from (a) are superimposed on two differently oriented dimers shown in the constant current topograph ($3.8 \times 4\,\mathrm{nm}^2$, 1 V). It is assumed that the Pb atoms are adsorbed on the hollow sites of the surface. (c) Sketch of the Fe layer with adsorbed Pb dimers. The left (right) Pb dimer is adsorbed in the [001] ([1$\bar{1}$1]) orientation on the Fe layer. All hollow sites of the Fe layer are equivalent, which is indicated by the positions of the Fe atoms of the first layer (small circles). The conventional unit cell of the bcc(110) surface is shown by the black inset.

of W, $a_W = 3.16\,\text{Å}$ [122]. While the atoms in the [001] – dimer are separated by a_W they are 13 % closer in the [1$\bar{1}$1] – dimer with a separation of $\sqrt{3}/2\,a_W$. These results are illustrated in a hard sphere model of the Pb dimers on the Fe layer in Fig. **13** (c). Additionally the Fe atoms of the first atomic layer are shown to indicate that all hollow sites are equivalent. Complexities arising from different adsorption sites do thus not have to be considered here in contrast to earlier experiments (*e. g.,* Refs. [118, 123, and 124]). $\mathrm{d}I/\mathrm{d}V$ maps were used to locate the positions of the Pb dimers on the domain structure of the Fe layer. Fig. **14** (a), (b) displays six dimers that are adsorbed on a domain and a domain wall. With two differently oriented dimers subjected to two different magnetization orientations four different configurations were studied in total (Fig. **14** (c)).

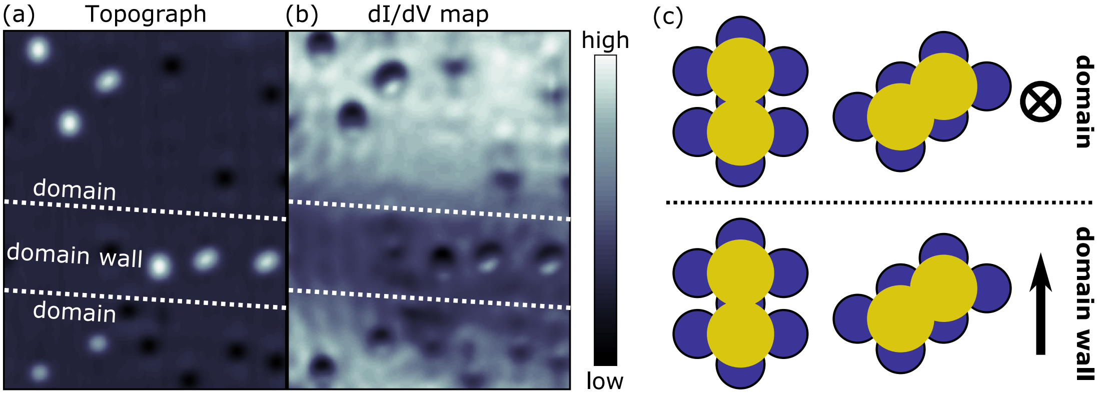

Figure 14. **Position of the Pb dimers on the domain structure**

(a) Constant current topograph and (b) simultaneously recorded dI/dV map showing six dimers ($13 \times 19\,\mathrm{nm}^2$, 70 mV). The upper (lower) three dimers are adsorbed on a domain (domain wall) and are consequently subjected to an out-of-plane (in-plane) orientation of the magnetization. (c) Schematic of the four different fabricated configurations. The yellow (blue) circles represent Pb (Fe) atoms. The magnetic orientation of the domain (domain wall) is indicated by $\otimes$ ($\uparrow$).

(b) Electronic structure of Pb dimers

dI/dV spectra were acquired with a W tip that should not be spin-polarized. Nevertheless, to exclude an influence of a spurious spin polarization of the tip (*e. g.,* by picking up Fe atoms) on the dI/dV spectra, its absence was verified with maps and/or spectra of the differential conductance of the Fe layer. For measurements determining the TAMR spectra were recorded on dimers adsorbed on domains (domain walls) with an opposite magnetization. The error of the mean was calculated from these spectra to quantify the measurement uncertainty. Consequently, the spread between curves of the same style reflects this uncertainty in Fig. **16**.

While both dimers show an unoccupied state close to 600 mV the [001] – dimer exhibits an additional occupied state at -50 mV. This peak is absent on the $[1\bar{1}1]$ – dimer, which is illustrated by an additional dI/dV curve in Fig. **15** (b). Surprisingly, only this peak is significantly affected by the magnetization direction, whereas the dI/dV spectra of the $[1\bar{1}1]$ – dimer remain essentially un-

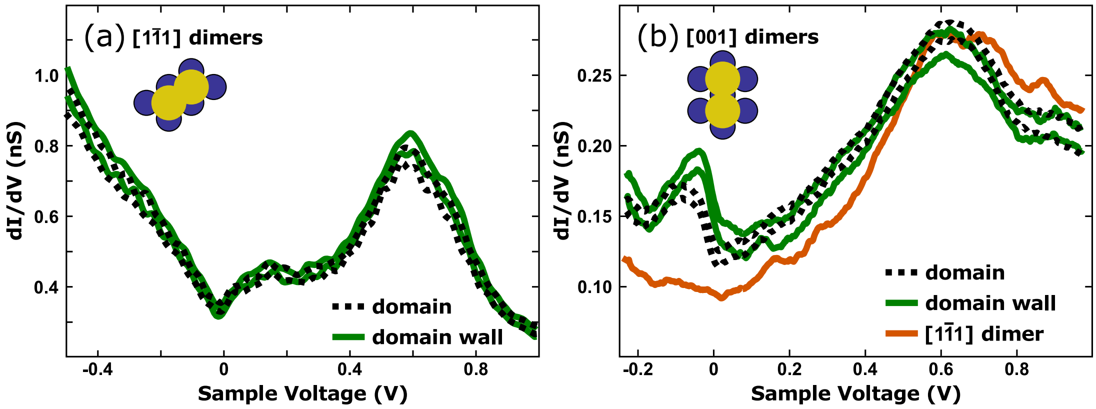

Figure 15. **Differential conductance of [1$\bar{1}$1] – dimers and [001] – dimers**
(a) Averaged dI/dV spectra on [1$\bar{1}$1] – dimers on a domain (dotted) and a domain wall (solid) (the feedback was opened at 1 V, 500 pA). The spread between curves of the same style represents the measurement uncertainty derived from averaging spectra of three different dimers adsorbed on one domain (one domain wall). A significant difference between [1$\bar{1}$1] – dimers is not observed. (b) Averaged dI/dV spectra on [001] – dimers. The spread between curves of the same style represents the measurement uncertainty derived from averaging spectra of one dimer adsorbed on a domain wall and two dimers adsorbed on oppositely magnetized domains. A spectrum of a [1$\bar{1}$1] – dimer (orange) is shown additionally for comparison (the feedback was opened at 1 V, 200 pA). The spectra in (a) and (b) were taken with different tips.

changed. Because the spectra are rather unaffected by the magnetization direction at positive bias voltages, the apparent heights of the dimers are identical on domains and domain walls. Consequently, no height correction had to be done for the spectra shown in this chapter because the tip was stabilized at 1 V prior to the spectroscopic measurements (see chapter **11 (b)** for the influence of different apparent heights).

The influence of the magnetization direction on the peak at −50 mV becomes clearer in Fig. **16** (a) displaying dI/dV spectra measured on [001] – dimers close to the Fermi level. Their difference is quantified in terms of the TAMR shown in Fig. **16** (b), which is defined as [25]:

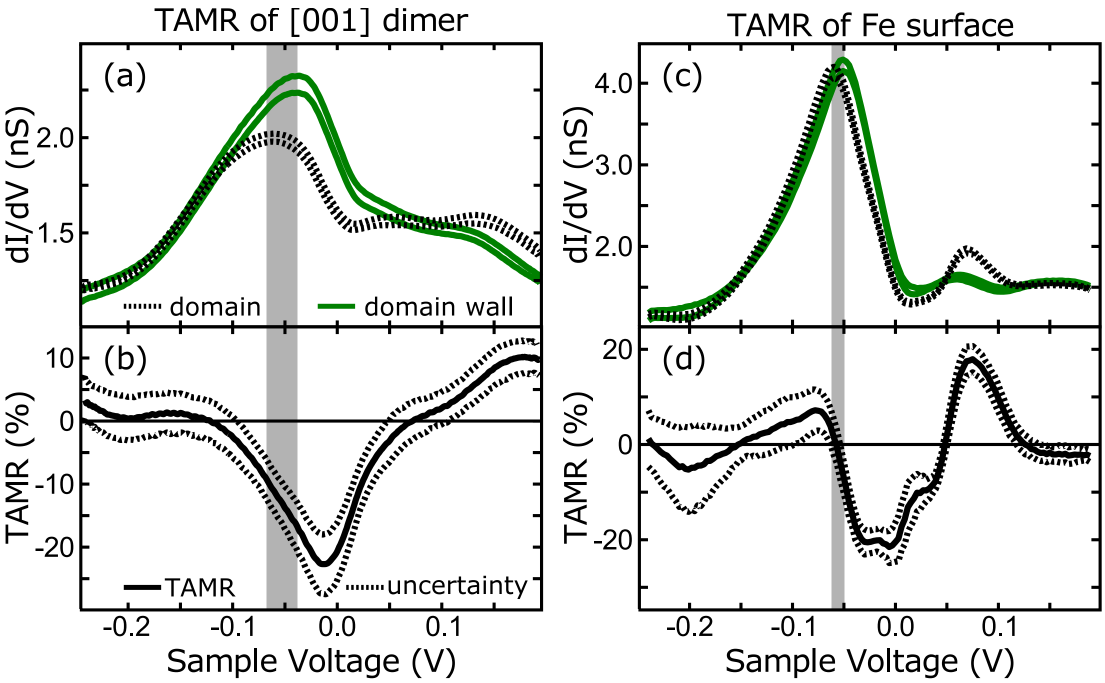

Figure 16. **TAMR of [001] − dimer and Fe surface**

(a) Averaged dI/dV spectra of [001] − dimers adsorbed on domains and domain walls, respectively. Spectra have been recorded on dimers adsorbed on oppositely magnetized domains (domain walls) to exclude an influence of a spurious spin polarization of the tip. Consequently, the spread of identical curves corresponds to the uncertainty of the measurement. (b) TAMR of the spectra in (a) calculated via equation (24). The dashed curves represent the error margin due to to measurement uncertainty. (c) Averaged dI/dV spectra of Fe domains and domain walls and (d) correspondent TAMR. The gray areas mark the positions of the peaks in the dI/dV spectra.

$$\mathrm{TAMR} = \frac{(\mathrm{d}I/\mathrm{d}V)_{\text{domain}} - (\mathrm{d}I/\mathrm{d}V)_{\text{domain wall}}}{(\mathrm{d}I/\mathrm{d}V)_{\text{domain}}} \tag{24}$$

The TAMR reaches its maximal value of $-(23 \pm 3)\,\%$ at a sample voltage of $-14\,\mathrm{mV}$.[6] At the Fermi level the magnitude of the TAMR is $-(21 \pm 5)\,\%$, which is twice as large as previously reported values obtained for single Co adatoms [25]. Additionally, the peak in the dimer dI/dV shifts by 21 mV upon modification of the magnetic orientation and exhibits a TAMR of $\approx -14\,\%$ (see the gray area in Fig. **16** (a, b)). The same experiment was performed on the bare Fe bilayer

---

[6] The ±-values correspond to the measurement uncertainty.

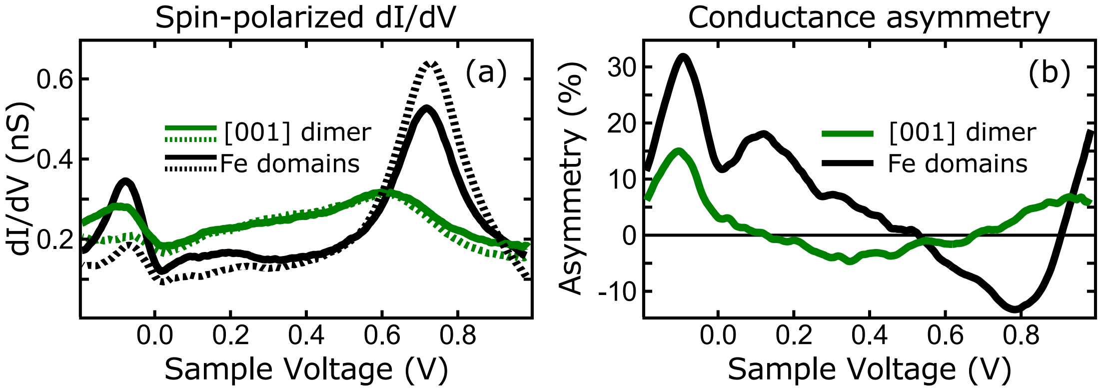

Figure 17. **Spin character of the dimer state**

(a) Spin-polarized dI/dV spectra of [001] – dimers and Fe domains. Dashed and solid curves correspond to oppositely spin-polarized domains and dimers adsorbed on them. (b) Asymmetry of the spectra in (a) (see chapter **6**).

for comparison (see Fig. **16** (c, d)). The dI/dV spectra on Fe exhibit a peak at 70 mV with a TAMR of (18 ± 3) %. Actually, this magnetization-dependent Fe state is used throughout this thesis to locate the position of domain walls with dI/dV maps. A second Fe state occurs at −55 mV and is thus at a similar energy as the dimer peak, which indicates that they may be linked. This is further corroborated by their similar shift due to varying the magnetization direction: Even though this Fe state shows no significant TAMR it shifts by 9 mV closer to the Fermi level like the dimer state (see the gray area in Fig. **16** (c, d)). It should be noted that the shift of the Fe state was previously attributed to different work functions on the domain and the domain wall in Ref. [24]. Different work functions, however, do not shift the energy scale and, moreover, the Fe state at 70 mV shifts in the other direction. It remains therefore unclear why one shift should result from work function differences while the other originates from SOC. It seems more reasonable to attribute all shifts to SOC. This is corroborated by the effect of SOC on the dimer state as will be shown below.

The relationship between the Fe state and the dimer state is further validated by spin-polarized dI/dV spectra that reveal the spin-character of both states. To this end the tip was covered with Fe in-situ and further modified until a spin-contrast between differently spin-polarized domains was achieved, thus ensuring

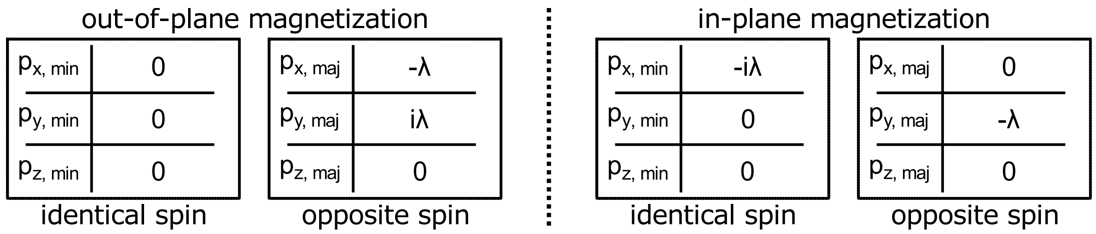

out-of-plane magnetization

identical spin

$p_{x,\,min}$	0
$p_{y,\,min}$	0
$p_{z,\,min}$	0

opposite spin

$p_{x,\,maj}$	$-\lambda$
$p_{y,\,maj}$	$i\lambda$
$p_{z,\,maj}$	0

in-plane magnetization

identical spin

$p_{x,\,min}$	$-i\lambda$
$p_{y,\,min}$	0
$p_{z,\,min}$	0

opposite spin

$p_{x,\,maj}$	0
$p_{y,\,maj}$	$-\lambda$
$p_{z,\,maj}$	0

Figure 18. Spin-orbit coupling of a minority p_z state to other p states
SOC matrix elements for a minority p_z state coupled to p states of different symmetries (p_x, p_y and p_z) and diffeernt spin-character (minority and majority) for an out-of-plane (domain, z-axis) and in-plane (domain wall, y-axis) magnetization direction (see equation (15) in chapter **3**). λ is the spin-orbit parameter.

an out-of-plane sensitivity of the tip [49]. Fig. **17** (a) shows the resulting $\mathrm{d}I/\mathrm{d}V$ curves acquired on Fe domains of opposite magnetization and [001] – dimers adsorbed on them, while Fig. **17** (b) displays the resulting conductance asymmetries (see chapter **6** for the relation between conductance asymmetry and spin polarization). Both asymmetries are positive at the sample voltages corresponding to the peak positions. Consequently, the dimer state at $-50\,\mathrm{mV}$ has the same spin-character as the Fe state, which is a minority d_{z^2} state [24]. Note that the Fe asymmetry is twice as large as the Pb asymmetry, which translates to their corresponding spin polarizations.

In conclusion, the similar energies of the Fe state and the dimer state, their similar shifts with varying the magnetization direction and their identical spin-characters strongly suggest that they are related. Since Pb is a 6p-element, its p_z state should hybridize with the d_{z^2} state. Consequently, the dimer state is presumably predominantly a minority p_z state. This may also be expected because p_z states preponderate in the vacuum over p states of different symmetry.

The absence of this peak on the $[1\bar{1}1]$ – dimer is likely a consequence of the different adsorption geometries of the dimers (see Fig. **14** (c)). The main difference between both dimer types is the presence of an Fe atom directly underneath the [001] – dimer, which is missing for the $[1\bar{1}1]$ – dimer. Consequently, the d_{z^2} state of the Fe layer may hybridize more easily with states of the [001] – dimer than the $[1\bar{1}1]$ – dimer, resulting in the occurrence of the additional peak.

The open question remains why this dimer peak shows a pronounced TAMR while its origin – the Fe peak – is only weakly affected by different magnetization directions. This difference can be explained using the orbital SOC model presented in chapter **3**. SOC hybridizes states differently depending on the orientation of the magnetization. Consequently, the observed TAMR may be explained by investigating the SOC hybridization of the minority p_z state of the dimer to other states. All these states are p states (p_x, p_y and p_z) for the two spin orientations (minority and majority). The SOC hybridization between these six states and the minority p_z state of the dimer is evaluated for an out-of-plane (z-direction) and an in-plane (y-direction) orientation of the magnetization, which reflect the domain and the domain wall, respectively. Fig. **18** displays the resulting couplings, which have been taken directly from equation (15) in chapter **3** with λ as the spin-orbit parameter.

If states hybridize, their amplitude decreases and they shift in energy. Experimentally, the amplitude of the dimer peak is larger on the domain wall than on the domain (see Fig. **16** (a)). Consequently, the hybridization is smaller on the domain wall (in-plane) than on the domain (out-of-plane). This requirement is only fulfilled by a SOC hybridization between the minority p_z state of the dimer and a majority p_x state,[7] *i. e.,* a mixing of the spin channels is required to explain the experimental observation. The small dependence of the minority Fe state on SOC might therefore originate from the lack of majority states on the Fe layer, which is corroborated by its large spin polarization of $\approx 75\,\%$ (see Fig. **9** (f) in chapter **6**). In comparison, the spin polarization of the dimer state is $\approx 37\,\%$ (Fig. **17** (b)). The dimer state is thus more affected by SOC than the Fe state because Pb contributes orbitals of new symmetries and has a smaller spin polarization, *i. e.,* more majority states are present that might be hybridized with minority states via SOC.

In conclusion, the TAMR of Pb dimers crucially depends on the exact adsorption site of the two atoms forming the dimers. While the electronic structure of $[1\bar{1}1]$ – dimer is essentially unaffected by SOC, the $[001]$ – dimer shows a TAMR as large as $-20\,\%$ close to the Fermi level. This TAMR is caused by an additional

---

[7] If the in-plane magnetization is chosen in the x-direction it would be the majority p_y state.

state on the [001] − dimer, which is missing on the $[1\bar{1}1]$ − dimer. Experimental observations strongly suggest that this state is linked to a state of the Fe layer. However, this Fe state is only weakly affected by SOC. The large TAMR of the dimer state can be motivated by a SOC mediated hybridization by orbitals that are admixed by the Pb atoms. An orbital SOC model suggests that a mixing of the spin channels can explain the observed TAMR. This mixing may be increased for all types of adsorbates because their spin polarization is smaller with respect to the substrate, *i. e.,* more minority and majority states are present at the same energy that can be coupled via SOC.

8. Ballistic anisotropic magnetoresistance of atomic Ir and Co contacts

The contents of this chapter have been reproduced in part with permission from J. Schöneberg, F. Otte, N. Néel, A. Weismann, Y. Mokrousov, J. Kröger, R. Berndt and S. Heinze, Nano Lett., **16**, 1450 (2016). *Copyright 2016 American Chemical Society. For further information regarding the tight-binding and DFT calculations presented in this chapter, please refer to the paper's accompanying supplementary information.*

The role of spin-orbit coupling (SOC) in transport phenomena is a research frontier in spintronics [40, 125–129]. A fundamental consequence of SOC is anisotropic magnetoresistance (AMR), which may be studied in junctions down to the scale of ballistic point contacts. Large magnetoresistances were reported from ferromagnetic Ni junctions [130, 131] and attributed to ballistic transport through a constrained domain wall [132–135] or magnetostriction [136, 137]. It has been predicted that single-atom junctions may display a giant magnetoresistance effect when electron transport occurs through a single fully spin-polarized quantum state [138]. Experimental data consistent with such a scenario were reported, but other interpretations remain possible [139, 140].

Large AMR effects have been predicted for the ballistic transport range [141–145] but their experimental verification is challenging. Although some results [108, 146] can be explained in terms of ballistic AMR (BAMR), large variations of its magnitude occur, likely due to the unknown atomic geometry of the junction [108, 137]. Suggested alternative interpretations are telegraph noise [136], quantum fluctuations [107] or magnetostriction [147].

Here, AMR is probed without using an external magnetic field thus eliminating possible artifacts due to magnetostriction. On a substrate with magnetic domains and domain walls exchange coupling is used to orient the magnetic moments of single adatoms out-of-plane and in-plane, respectively. The tip of a scanning tunneling microscope (STM) is used to measure the conductances of the resulting junctions on domains (G_d) and domain walls (G_w) as a function of the tip-sample

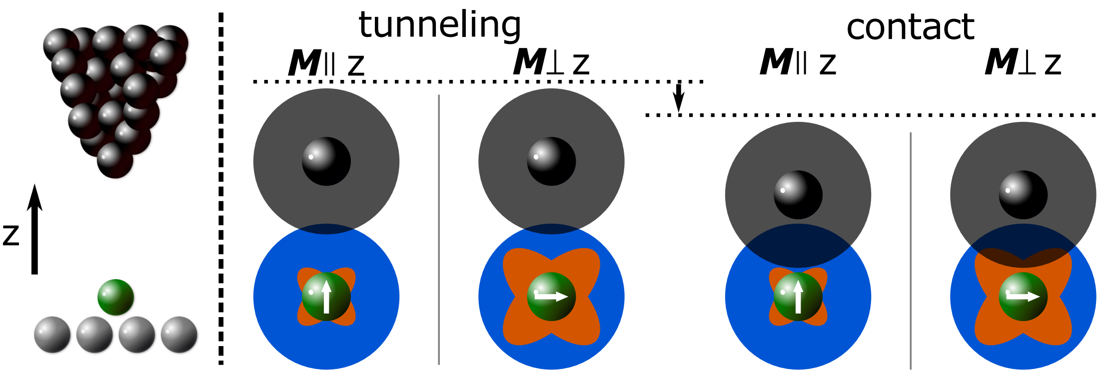

Figure 19. **Distance-dependent AMR of single-atom contacts in a nutshell** Sketch of the experiment. Left panel: A sharp tip (black) is placed within nm distance of an adatom (green) on a substrate (gray). Right panel: The overlap between orbitals of the tip apex atom (black) and orbitals of the adatom (blue and orange) determines the current. SOC is changing the extent of the orange orbital (indicated by the isosurface of the LDOS) for different orientations of the magnetization $\boldsymbol{M}$. This orbital does not contribute to the current in the tunneling range but becomes relevant at contact.

distance. We define the AMR as

$$\mathrm{AMR} = (G_\mathrm{d} - G_\mathrm{w})/G_\mathrm{d}\,. \tag{25}$$

(a) Tight-binding model

The essential physics leading to distance-dependent AMR may be demonstrated with a microscopic model. Its main ingredients are (i) a local spin-orbit coupling of the adatom's d-states and (ii) different spatial decays into the vacuum of orbitals with different symmetries. Fig. **19** shows sketches of the experiment and of the orbitals whose overlap is causing the current. The orbitals are shown for two different orientations of the magnetization $\boldsymbol{M}$ and two tip-adatom distances. In the tunneling range the tip orbital only overlaps with the extended orbital of the adatom. The current thus probes SOC-mediated effects of this orbital and is insensitive to the more localized state. At smaller separations, however, the contribution of this orbital increases. Consequently, the AMR in the tunneling range is dominated by the states with the weakest spatial decay, while at contact orbitals with another symmetry and hence different SOC-related

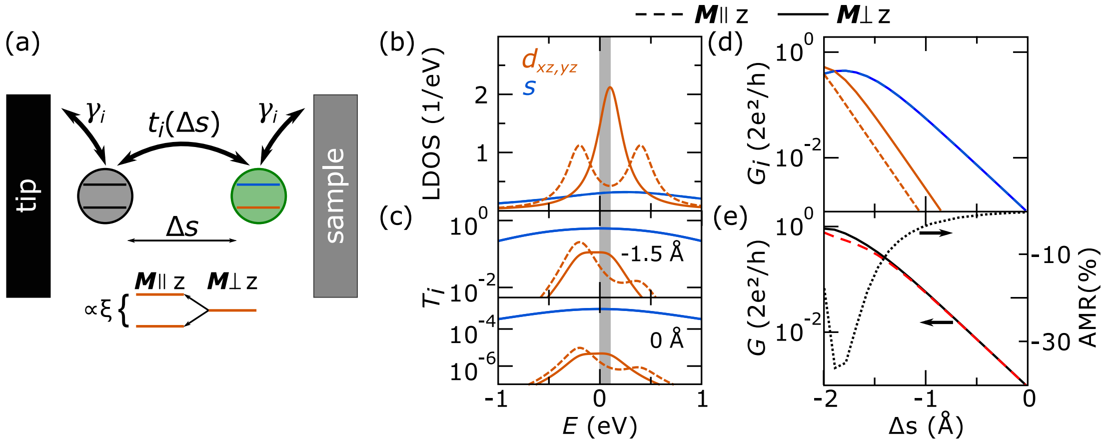

Figure 20. **Tight-binding model**

(a) The orbitals i of two atoms are coupled to metallic contacts by self-energy terms $-i\gamma_i$ added to the onsite energies and mutually via hopping terms $t_i(\Delta s)$ (Δs: gap distance with respect to reference point in the tunneling regime), respectively. The $t_i(\Delta s)$ reflect different spatial decays of the orbitals into the vacuum. For simplicity, we only consider s (blue) and $d_{xz,yz}$ (orange) states of the same spin channel for the adatom. Depending on the orientation of $\boldsymbol{M}$, SOC splits the $d_{xz,yz}$ orbitals by an amount proportional to the spin-orbit coupling strength ξ. (b) Local density of states of the adatom at $\Delta s = 0\,\text{Å}$ decomposed into atomic orbitals. Solid (dashed) lines show data for a magnetization perpendicular (parallel) to the surface. (c) Transmissions T_i of channels i for two displacements Δs. (d) Conductance of different channels as a function of the separation Δs calculated for the energy window $[0, 100]$ meV as indicated by the gray shading in (c) and (d). (e) Total conductance and corresponding AMR calculated via equation (25).

effects play a role. The evolution of the conductance with the tip-adatom distance can be modeled with a tight-binding scheme (Fig. **20**). In this model two atoms are coupled mutually via hopping terms and to metallic contacts via constant self-energy terms that lead to a broadening of the atomic states (Fig. **20** (a)). The hoppings are dependent on Δs, which is the gap distance defined to a reference point in the tunneling regime. We consider three orbitals of the adatom s, d_{xz} and d_{yz}, with different decay lengths and assume the two d states to be of the same spin channel and energetically degenerate without SOC. The modification of the electronic structure due to SOC is included by the Hamiltonian $H_{\mathrm{SOC}} = \xi\, \mathbf{l} \cdot \mathbf{s}$, where $\mathbf{l}$ and $\mathbf{s}$ are the operators of the orbital and spin angular momenta, respectively, and ξ is the spin-orbit coupling strength (see chapter **3**). For the d_{xz} and d_{yz} states this hybridization is proportional to $\cos\theta$ (see chapter **11 (a)**), θ being the angle between the magnetization direction $\boldsymbol{M}$ and the surface normal. Consequently, the $d_{xz,yz}$ state is split by an amount proportional to ξ in the local density of states (LDOS) for a parallel magnetization ($\theta = 0$) (Fig. **20** (b)) (see chapter **3**). The resulting transmissions T_i for the different orbitals i are shown in Fig. **20** (c). They are not symmetric like the LDOS because they include the effect of the tip states with different onsite energies. In the tunneling regime ($\Delta s = 0\,\text{Å}$) the transmission of the s state exceeds that of the $d_{xz,yz}$ orbitals by far. When the separation is decreased ($\Delta s = -1.5\,\text{Å}$), however, similar transmissions of all channels are found near $E = 0\,\text{eV}$. Integration over the range $[0, 100]\,\text{meV}$ leads to the orbital conductances shown in Fig. **20** (d). The tunneling conductance is dominated by the slowly decaying s orbital. At contact ($\Delta s < -1.5\,\text{Å}$), the $d_{xz,yz}$ orbitals significantly contribute. They cause the conductance change between different magnetization directions that can be seen in the total conductance (Fig. **20** (e)). The resulting AMR vanishes in the tunneling range and is negative at contact.

The quantitative evolution of the conductance depends on the energy interval used for integration, but some effect of the magnetization on the conductances remains so long as the interval includes the $d_{xz,yz}$ states. As a result, negative as well as positive AMR values with different magnitudes may be expected from this model. To test these predictions for atomic-scale contacts, we investigated single Co and Ir atoms adsorbed onto a double layer Fe film on W(110). As previously shown, AMR may also occur at larger tip-adatom distances in the tunneling range, where the differential magnetoresistance showed an oscillatory behavior as a function of the bias voltage [25]. To avoid this complication and also to increase the junction stability at µA currents in the ballistic regime, the present study of BAMR focuses on a low bias range. For this study it is assumed that the magnetic moments of Co and Ir atoms adsorbed on the Fe double layer align parallel to the Fe magnetization, which is corroborated by first-principles

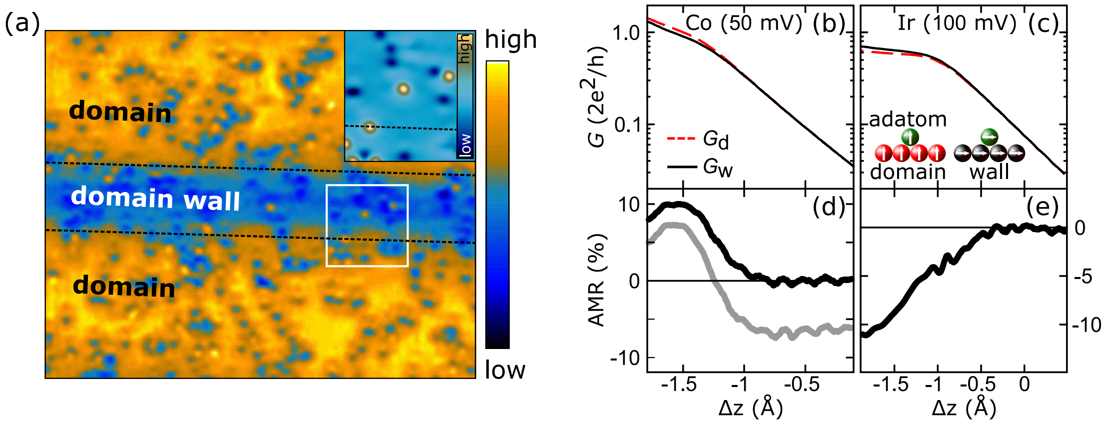

Figure 21. **Experimental data from Co and Ir adatoms on a ferromagnetic Fe bilayer on W(110)**

(a) dI/dV map (70 mV, 0.5 nA, $52 \times 42\,\mathrm{nm}^2$) of single Ir atoms on an Fe bilayer . Magnetic domains and domain walls of the Fe bilayer are separated by dashed lines. Defects and atoms appear with reduced and enhanced signal, respectively. The white square marks an area whose constant-current topograph is shown in the inset (100 mV, 50 pA, $10 \times 10\,\mathrm{nm}^2$). The central atom lies on the domain wall and is separated from the nearest defect by 2 nm. (b) Conductance G versus vertical tip displacement Δz for Co, and (c) for Ir adatoms. Bias voltages were set to 50 mV (Co) and 100 mV (Ir). Negative Δz indicates a reduction of the tip-adatom distance. The dashed and solid curves show the conductances for an adatom on a domain (G_d) and on a domain wall (G_w), respectively. (d) and (e) display the AMR calculated via equation (25) for Co and Ir, respectively. In panel (d), the black curve represents the ARM of Co adatoms with no correction for their different apparent heights. Including these height differences in the calculation of the AMR results in the gray curve (see text for details).

calculations [25, 37].

(b) Experimental results

dI/dV maps and simultaneously recorded topographs served to locate the adatoms adsorbed on domains and domain walls (Fig. **21** (a)). We measured the conductance $G(\Delta z)$ of single atoms while changing the tip-adatom distance by a displacement Δz of the tip. $\Delta z = 0\,\mathrm{pm}$ is defined by the parameters at which the feedback loop was opened (Co: 50 mV, 1.1 µA; Ir: 100 mV, 0.5 µA). Since the same parameters were used for adatoms on domains and domain walls $G_\mathrm{w} = G_\mathrm{d}$ and consequently AMR = 0% at $\Delta z = 0\,\mathrm{pm}$.

Nonetheless, AMR in the tunneling range may be observed. SOC affects the density of states at certain energies and thus the tunneling current at certain voltages. Adatoms with non-equivalent magnetization directions may therefore appear with different apparent heights in constant-current topographs. Far in the tunneling regime (≈ 0.1 nA) Co atoms on domain walls appear 2.5 pm higher than Co atoms on domains at 50 mV, whereas Ir atoms exhibit no height difference at 100 mV.

The conductance data of Co and Ir show smooth transitions to contact (Fig. **21** (b), (c)). At contact ($\Delta z < -1\,\mathrm{Å}$) the conductance of Co atoms on domains is higher than on domain walls. Surprisingly, for Ir this sequence is reversed. This difference is directly reflected by the AMR, which is positive for Co and negative for Ir at contact (black curves in Fig. **21** (d), (e)).

Accounting for the different apparent heights of Co adatoms results in a horizontal shift of the conductance traces with respect to each other. As a consequence the AMR curve moves vertically while its shape remains essentially unaltered (gray curve in Fig. **21** (d)).

Nonetheless, this result shows that a height difference of few pm results in a modification of the AMR by several %. The influence of such height differences is quantified in the following. In the tunneling regime the conductance depends exponentially on the tip-adatom separation. Consequently, the influence of height differences may be illustrated by evaluating equation (25) for two identical exponential conductance curves, which start at tip-adatom separations z and $z + d$:

$$1 - \frac{\exp(-2\,\kappa\,z)}{\exp(-2\,\kappa\,(z+d))} = 1 - \exp(-2\,\kappa\,d) \approx 2\,\kappa\,d. \tag{26}$$

The decay constant κ is typically on the order of $1\,\mathrm{Å}^{-1}$ for metals, while d is typically on the order of few pm. Hence, the exponential function is approximated linearly. Equation (26) shows that every pm height uncertainty is translated to an AMR uncertainty of 2 %. This is in agreement with the shift of the AMR for Co in Fig. **21** (d) by ≈ 5 % in the tunneling regime for an apparent height difference

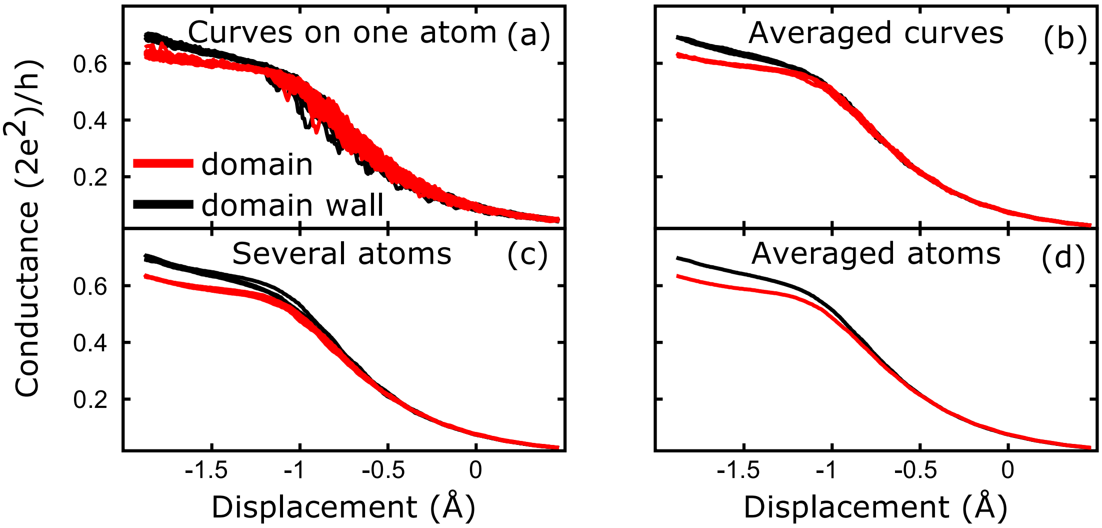

Figure 22. **Measurement procedure of the BAMR**

(a) 20 conductance curves measured on one adatom adsorbed on a domain wall (domain). (b) Several mean curves for one atom calculated from sets like the one shown in (a). (c) The mean curves from (b) were averaged to get a final curve for one atom. Such curves are shown her for several atoms. (d) Mean curve from the data in (c).

of 2.5 pm. This dependence also occurs for fluctuations in Δz. Consequently, great care was done to minimize this influence on the conductance curves, which is illustrated in the following. The procedure carried out for this purpose is illustrated in Fig. **22** (a) to (d) for the conductance curves of Ir atoms adsorbed on domains and domain walls measured with the same tip. First, on one atom adsorbed on a domain (domain wall) several sets containing 20 conductance curves were measured, from which one set is shown in Fig. **22** (a). The position and integrity of the adatom was checked in between these sets with constant-current topographs. Second, the mean curve for each set was calculated. Fig. **22** (b) shows several of such curves. Third, all these curves were averaged to obtain the final curve for one adatom. This procedure was repeated on different adatoms. Their final curves, which were measured with the same tip, are displayed in Fig. **22** (c). At this stage domain and domain wall data are compared and checked for consistency. Finally, the data curves of all adatoms are averaged (Fig. **22** (d)).

Another influence on the observed AMR might originate from a spurious spin polarization of the tip. This effect was excluded by checking for differences in the apparent heights and in the differential conductance using simultaneously recorded constant-current topographs and dI/dV maps at the bias voltage, at which the feedback loop was opened. Additionally, conductance curves were measured on atoms adsorbed on antiparallel magnetized domains (domain walls).

We note that the exact shape of the conductance and thus the AMR depends on the tip, which is discussed in chapter **8 (d)**. Despite these quantitative differences the evolution of the AMR is qualitatively reproduced with different tips.

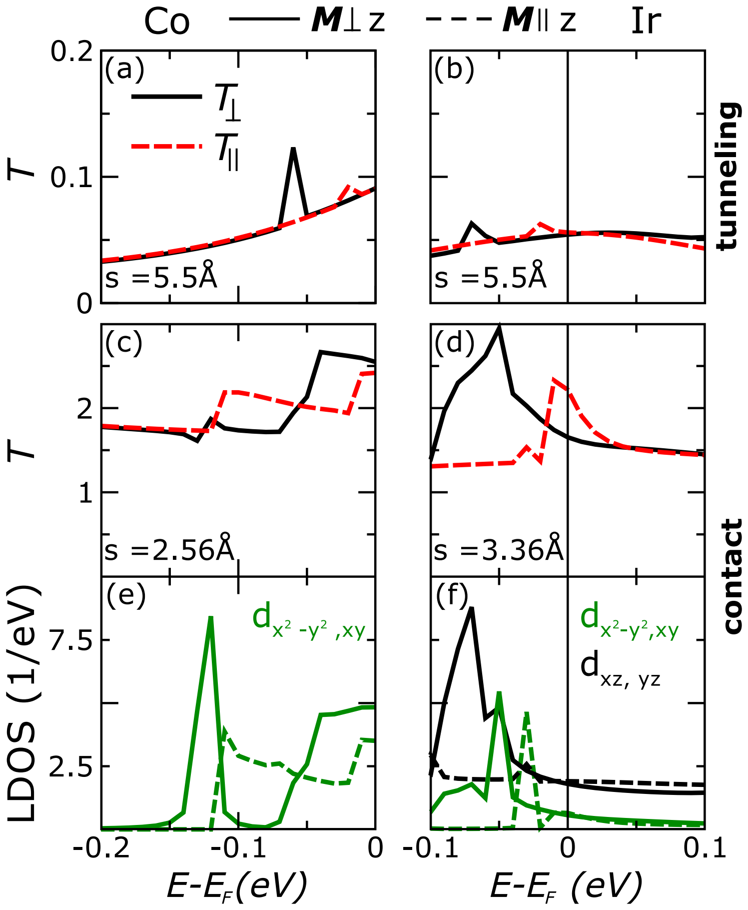

Figure 23. **Total transmission and LDOS of a junction of two Fe atom chains terminated with Co or Ir.**

All solid (dashed) lines correspond to a magnetization $\boldsymbol{M}$ perpendicular (parallel) to the wire axis. (a), (b) Total transmissions T in the tunneling regime at a separation of $s = 5.5$ Å for Co and Ir, respectively. (c), (d) Total transmissions in the contact regime for Co ($s = 2.56$ Å) and Ir ($s = 3.36$ Å), respectively. (e), (f) LDOS corresponding to (c), (d) of the $d_{x^2-y^2,xy}$ (green) and $d_{xz,yz}$ (black) states at the apex atom.

(c) Ab-initio model

So far we have shown that the experimental observations are in qualitative agreement with the expectations from the tight-binding model. Nonetheless, in contrast to this model, the full electronic structure of the atomic-scale junctions studied here consists of many states with lifted spin degeneracy. To analyze this issue we performed first-principles calculations based on density functional theory (DFT). The resulting strength of SOC and the spatial decay rates of the orbitals have been included in the tight-binding calculations presented before.

We considered symmetric junctions comprised of a linear Fe atom chain terminated by Co or Ir apex atoms. A gap of variable size s is introduced between the apex atoms to mimic the STM experiment.

The transmission was calculated with a DFT based method [148] utilizing the full-potential linearized augmented plane wave (FLAPW) method as implemented in the one-dimensional version of the `FLEUR` code [149]. The FLAPW wave functions are mapped on a local-basis representation in terms of maximally localized Wannier functions, which is used to construct a tight-binding like Hamiltonian. This Hamiltonian is then treated within a Green's function formalism to yield the transmission. The LDOS and the transmissions T for magnetizations parallel ($T_{\|}$, corresponding to the domains) and perpendicular ($T_{\perp}$, corresponding to the domain wall) to the wire axis are calculated taking SOC into account.

This model is suitable to realistically describe the spin-orbit coupling of the d-states at the apex atoms and their decay across the vacuum gap. As the apex atoms are coupled to one dimensional chains instead of the surface of a three dimensional crystal, we expect the energetic broadening of the atomic states (described by a self-energy in the tight-binding model) to be much weaker than in the experiment. This implies, that spectral features in the LDOS or transmission might be at different energies and much sharper compared to the experimental data. Although we cannot expect a one-to-one correspondence between the DFT calculations and the experimental data, we note that it is still possible to reproduce the experimental AMR by choosing suitable integration intervals.

Fig. **23** shows the total transmission and the LDOS at contact for parallel (dashed lines) and perpendicular (solid lines) magnetizations. In the tunneling range the transmission of Co (Fig. **23** (a)) is dominated by sd_{z^2} states because of their slow decay across the gap. For a magnetization perpendicular to the current direction the transmission $T_\perp$ displays a small peak at $E_\mathrm{F} - 60\,\mathrm{meV}$, which is caused by SOC-induced mixing of sd_{z^2} with d_{yz} states. This peak would lead to a negative AMR at large s, if the integration interval is chosen appropriately. The transmission of the Ir apex atoms shows similar peaks for both magnetization directions at energies below E_F (Fig. **23** (b)). The mechanism here is the same as reported in Refs. [25] and [110].

The transmissions at smaller separations (contact) are evidently different. For a magnetization along the chain, the Co apex atom shows the characteristic fingerprint of BAMR due to SOC induced band splitting, *i. e.,* step-like features in $T_\|$ (Fig. **23** (c)) [141]. This results from SOC lifting the degeneracy of the Co $d_{x^2-y^2}$ and d_{xy} states, which is discernible in the LDOS (Fig. **23** (e)). These two steps lead to a positive AMR in the energy interval between $-100\,\mathrm{meV}$ and $-50\,\mathrm{meV}$ and a negative AMR between $-50\,\mathrm{meV}$ and E_F.

In contrast to Co, the Ir apex atom has $d_{x^2-y^2,xy}$ and $d_{xz,yz}$ states of different spin channels near E_F at contact, which are mixed because of the stronger SOC constant of Ir (Fig. **23** (f)). This leads to a broad peak of $T_\perp$ between $-100\,\mathrm{meV}$ and E_F (Fig. **23** (d)). For parallel magnetization $T_\|$ peaks occur just below E_F, which is caused by the band edge of the $d_{x^2-y^2,xy}$-like states.

The DFT calculations confirm the tight-binding result. Indeed, the drastic change of the AMR from tunneling to contact is caused by orbitals with different symmetries and decay rates into the vacuum. However, the transmissions behave in a more complex manner than in the tight binding model due to a more intricate hybridization between a variety of states (sd_{z^2}, $d_{xz,yz}$ and $d_{x^2-y^2,xy}$), which partially are of different spin character.

The above results unambiguously show the occurrence of ballistic anisotropic magnetoresistance of single-atom junctions. Our calculations show that the magnetoresistance is caused by an intricate SOC-mediated hybridization between d orbitals of different symmetry and different decay rates. Because these are rather universal properties, BAMR should occur in a wide variety of single-atom junc-

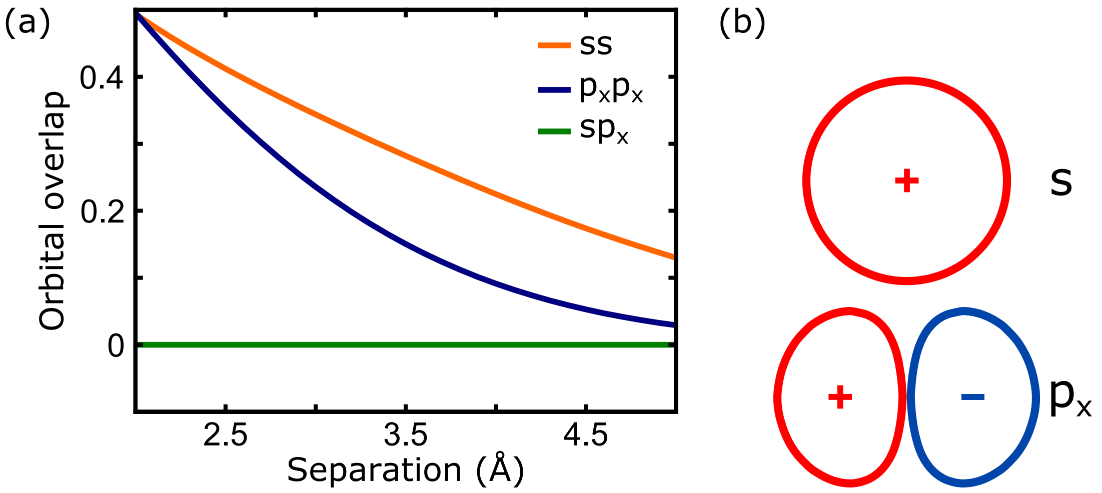

Figure 24. **Overlap between orbitals of different symmetry**

(a) The overlaps between s states and p_x states are calculated for different separations between the orbitals. While the ss overlap dominates at large separations, the $p_x p_x$ overlap significantly increases at smaller distances. The sp_x overlap is negligible. (b) The overlap between the s state and the p_x state vanishes because the positive and negative contribution of the p_x state compensate each other.

tions. We observed this effect from two species, Co and Ir, which exhibit different signs of the magnetoresistance in contact. Our results show that the sign of the BAMR and its magnitude may be tuned by using suitable adatoms to adjust the electronic structure close to the Fermi energy.

(d) Influence of the tip on the observed BAMR

The BAMR of single adatoms stems from orbitals being hybridized differently by SOC. While the current in the vacuum is typically dominated by s, p_z and d_{z^2} states, p and d states of different symmetry contribute significantly in the ballistic range, resulting in the BAMR described in the previous chapter. The amount by which an orbital can contribute to the total current depends on the tip and its states.

In a first approximation the tunneling current can be described by the overlap between the states of the tip and the adatom. Fig. **24** shows the calculated overlaps between s states and p_x states for different separations between the

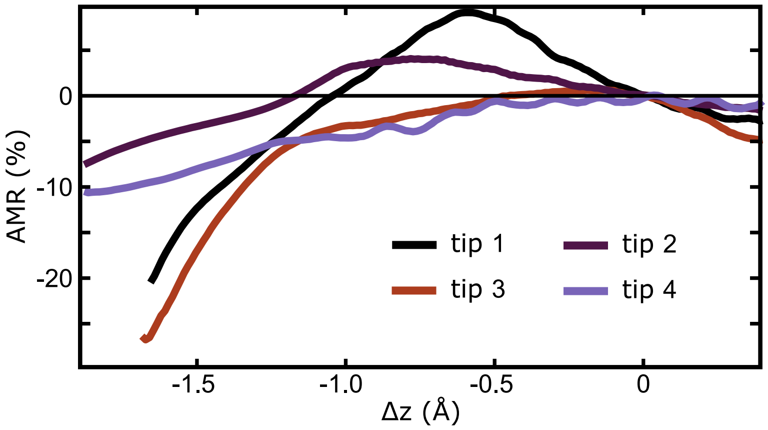

Figure 25. **Reproducibility of the AMR signature for Ir**

The AMR is shown for four different tips. Even though the evolution of the AMR is different, all tips display a negative AMR in contact. The data of tip four was shown in the previous chapter.

orbitals. In agreement with the calculations in the previous chapter, the vacuum regime (*i. e.,* at large separations) is dominated by the s states while in contact (*i. e.,* at smaller separations) the more localized p_x states significantly contribute. Important to note here is the vanishing of the sp_x overlap because the positive and the negative contribution of the p_x state cancel each other (Fig. **24** (b)). An adatom state is hence only visible in the current if a suitable orbital is present at the tip, which results in a non-vanishing overlap. In the previous chapter the BAMR for Ir adatoms was described by the SOC induced hybridization of the $d_{xz,yz}$ and $d_{x^2-y^2,xy}$ states. It follows from the considerations above that the contribution of these states to the current depends on the orbital structure of the tip. A variation of the observed BAMR for different tips may thus be expected and was also observed experimentally as is shown in Fig. **25**. Four different tips were used to measure the conductance of several adatoms adsorbed on domains and domain walls. Even though the magnitude and evolution of the AMR varies for the tips, it is always negative in contact. The conductance of the Ir atoms in contact is thus reduced for an in-plane magnetization due to SOC, which is the fingerprint of BAMR.

9. Conclusion

In this thesis I have used scanning tunneling microscopy (STM) to investigate the interplay between the electrical conductance and the magnetization at the atomic scale. Spin-dependent properties are induced in several metallic adsorbates by advantageously using a ferromagnetic Fe bilayer on W(110) as a substrate. Spin-polarized currents are measured on an atomic species that is paramagnetic as a bulk and the influence of the tunneling gap on the observed signal is revealed. The effect of spin-orbit coupling on the conductance is shown to critically depend on the atom structure and its occurrence on the ballistic scale is unambiguously observed for the first time.

Single Ir atoms adsorbed on a ferromagnetic Fe domain structure are investigated with STM. These adatoms are largely spin-polarized by this structure, which is demonstrated by measurements of the differential conductance using spin-polarized tips. These results show that a wide variety of atomic species beyond the well-known $3d$ elements may be expected to be spin-polarized on the atomic scale. Furthermore, the vacuum gap plays an important role on the observed signal as it acts as an orbital filter: At the adatom d states dominate, while sp_z states preponderate in the vacuum. This is expected to result in an inversion of the spin polarization above the adatom at certain energies. The distance dependence of this filter for single adatoms has thus been investigated experimentally here. Surprisingly, the sign of the spin-polarized signal is found to remain unchanged for the entire experimentally accessible range, which reaches to tip-adatom separations of 1 Å from the point of contact. Indeed, calculation corroborate that the filtering happens over a distance of less than 4 Å from the adatom and that an inversion of the spin polarization occurs within the next-neighbor distance. Consequently, the tunneling gap is efficiently filtering orbitals, *i. e.,* the spin-polarized signal calculated from spectra of the differential conductance is only weakly affected by the tip-adatom distance.

Non spin-polarized tips are used to observe modifications to the density of states due to spin-orbit coupling (SOC). Here, these modifications are first observed on atomic structures beyond the single adatom. Pb dimers with two orientations are built with the tip of the STM on the Fe bilayer on W(110). For one dimer species, the electronic structure is shown to significantly depend on the orientation of the magnetization, while the other dimer species remains essentially unaffected. The magnetization dependent DOS is explained using an orbital SOC model that attributes the observed effect to a SOC mediated hybridization of states with different spin. These results demonstrate the importance of the atomic environment since new orbitals may be admixed that are hybridized via SOC. This admixing is furthermore shown to critically depend on the adsorption geometry of the adsorbate as evidenced by the different behavior of the dimer species.

Ballistic contacts are formed by bringing a non spin-polarized tip into contact to single Ir atoms. The conductance of such contacts is shown to depend on the orientation of the magnetization and are thus linked to anisotropic magnetoresistance. Consequently, anisotropic magnetoresistance on the ballistic scale is shown unambiguously by these results in contrast to previous experiments that might have been influenced by magnetostriction. Magnetostriction, however, is negligible for contacts formed with the STM. These findings are interpreted in terms of a SOC mediated hybridization of orbitals. The observed signal furthermore depends on the tip-adatom separation, which is explained by different orbitals being probed in contact than in the vacuum due to different decay rates. Since these properties are rather universal, anisotropic magnetoresistance on the ballistic scale should occur in a wide variety of single-atom junctions.

10. Outlook

The experiments presented in this thesis show the importance of SOC on the atomic scale and indicate that the magnitude of SOC related effects may be tuned by choosing appropriate atomic species or building atomic structures. Furthermore, it was shown that the observed effect is largely dependent on the symmetry of the orbitals dominating the current. Consequently, SOC dependent effects may be largely enhanced by removing s states from the signal, because they are not affected by SOC and thus result in an independent background. Molecular junctions have been proposed to remove such backgrounds [150] and may be studied experimentally.

Additional modifications to the orbitals contributing to the current may be achieved by functionalizing the tip of the STM. By picking up CO molecules, for instance, the contributions of p_x and p_y states to the tunneling current are increased [151]. The proportion of states with different symmetry, *e. g.,* s states, is consequently decreased. This orbital filter may be investigated by measuring the same SOC dependent effect with a functionalized tip and a usual metal tip.

This thesis showed that anisotropic magnetoresistance – an effect known from bulk materials – also manifests itself on atomic structures. Magnetocrystalline anisotropy (MA), another SOC related effect, has also been observed for single adatoms subjected to differently oriented magnetic fields (*e. g.,* in Ref. [17]). In this study the observed MA was attributed to an interplay between the adatom and the anisotropic surface layer (Cu_2N on Cu(001)). To investigate the MA of adsorbates only, identical non-spherical structures with different orientations with respect to the magnetization direction may be build. This is illustrated in Fig. **26** by dimers adsorbed on an fcc(001) surface. Note that both dimers in Fig. **26** (a) and (b), respectively, have the same atomic environment, *i. e.,* possible effects on the electronic structure should be linked to their different orientations with respect to the magntization direction. A suitable system for these measurement are dimers on Co monolayers on Cu(001) that are magnetized along the [110] direction [152–154]. Atomic chains or molecules like pentacene might also be used instead of dimers.

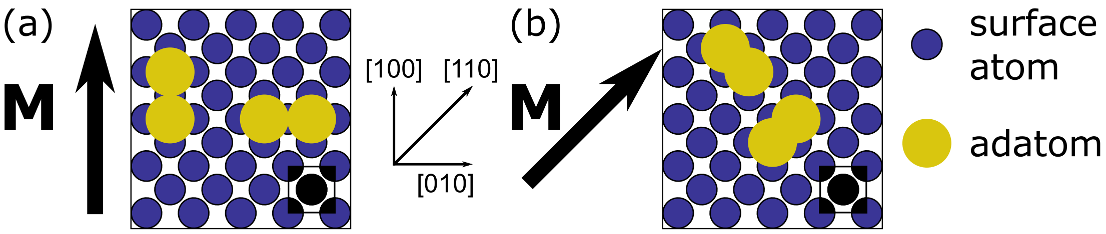

Figure 26. **Magnetocrstalline anisotropy on the atomic scale**
Dimers with different orientations but identical atomic environment can be built on an fcc(001) surface. Possible differences in the electronic structure of the dimers are thus linked to the different orientations of the dimers with respect to the magnetization $\boldsymbol{M}$ of the surface layer (or external magnetic field). The observed effect may therefore be understood as magnetocrystalline anisotropy. Such dimer pairs can be built for $\boldsymbol{M}$ being along the (a) [100] or the (b) [110] direction. The black inset in (a), (b) shows the conventional unit cell.

All experiments mentioned above are also possible with an external magnetic field instead of a ferromagnetic substrate to tilt the spin-quantization axis. Especially the angular dependence of the densities of states due to SOC may be studied in this way (see chapter **11 (a)**). However, due to the small energies associated with a magnetic field ($\approx 0.1\,\mathrm{meV/T}$) a high energy resolution and thus very low temperatures are needed[8]. It may be therefore preferable to use ferromagnetic substrates and align their magnetization direction with an external magnetic field.

---

[8] Due to the Fermi-distribution the spectroscopic resolution at a temperature T is limited to $\approx 4k_{\mathrm{B}}T$ with k_{B} as the Boltzmann constant [30]. This corresponds to $0.34\,\mathrm{meV/K}$.

11. Appendices

(a) Spin-orbit coupling matrix for p-states with an arbitrary orientation of the spin quantization axis

In this appendix the SOC model from chapter **3** for p states is expanded to arbitrary orientations of the spin-quantization axis (SQA). The resulting Hamiltonian is treated within a Green's function formalism to derive the DOS. The dependence of the projected DOS and the total DOS on the orientation of the SQA is illustrated for a few examples.

The SOC matrix can be written using two matrices M and N (see Refs. [36] and [39])[9]:

$$H_{\mathrm{SOC}} = \lambda \begin{pmatrix} M & N \\ -N^* & -M \end{pmatrix} \tag{27}$$

M (N) describes the coupling of states with equal (different) spin character. Please note that equation (27) verifies that SOC does not change the total energy if all states are occupied since $tr(H_{\mathrm{SOC}}) = \lambda(tr(M) + tr(-M)) = 0$ [36].

An arbitrary orientation of the spin quantization axis is defined using spherical coordinates (sinθ cosϕ, sinθ sinϕ, cosθ) with the azimuthal angle ϕ and the polar angle θ. Here, M and N and thus $H_{\mathrm{SOC}}(\theta,\phi)$ are calculated using the formulas given in in Ref. [4]. For p states and their basis $\{p_{x\uparrow}, p_{y\uparrow}, p_{z\uparrow}, p_{x\downarrow}, p_{y\downarrow}, p_{z\downarrow}\}$ with $p_x = \frac{1}{\sqrt{2}}(\,|1,-1> - |1,1>)$, $p_y = \frac{i}{\sqrt{2}}(\,|1,-1> + |1,1>)$ and $p_z = |1,0>$ [35] one obtains

$$M = i \begin{pmatrix} 0 & -\cos\theta & \sin\theta\,\sin\phi \\ \cos\theta & 0 & -\sin\theta\,\cos\phi \\ -\sin\theta\,\sin\phi & \sin\theta\,\cos\phi & 0 \end{pmatrix} \tag{28}$$

and

$$N = \begin{pmatrix} 0 & i\sin\theta & \cos\phi + i\sin\phi\,\cos\theta \\ -i\sin\theta & 0 & \sin\phi - i\cos\phi\,\cos\theta \\ -\cos\phi - i\sin\phi\,\cos\theta & -\sin\phi + i\cos\phi\,\cos\theta & 0 \end{pmatrix}. \tag{29}$$

---

[9] The element (2,2) is M^* in Ref. [36]. However, here it is $-M$, which is verified by equation (12) in chapter **3** and in agreement with Refs. [37] and [39].

The DOS resulting from H_{SOC} is calculated using the Green's function matrix g for the p basis, which is defined for an energy E via the resolvent

$$g(E) = \lim_{\eta \to 0^+} \left((E + i\eta) \cdot \mathbb{1} - H_0 - H_{\mathrm{SOC}} - \Gamma \right)^{-1}. \tag{30}$$

H_0 is the unperturbed Hamiltonian for the p states. Consequently, it is a diagonal matrix with the eigenvalues E_j for state p_j and an optional Zeeman term to lift the spin degeneracy. Γ is a diagonal matrix with imaginary elements to induce a broadening of the states in the DOS. The DOS of state j is given by the diagonal matrix elements of g via

$$\mathrm{DOS}_j(E) = -\frac{1}{\pi} \operatorname{Im}(g_{jj}(E)). \tag{31}$$

The total DOS is the sum over the DOS_j, *i. e.,* $\mathrm{DOS}_{\mathrm{tot}}(E) = -\frac{1}{\pi} \operatorname{Im}(tr(g(E)))$.

The effect of SOC on the DOS is illustrated in Fig. **27** for different choices for the E_j and different spin mixings. To this end the orientation of the SQA was rotated in the yz-plane from $+z$ to $+y$ to $-z$, *i. e.,* θ was changed from 0 to π for a fixed ϕ of $\pi/2$. Only the spin-averaged DOS are shown here because the corresponding SOC dependent experiments in chapters **7** and **8** are done with non-magnetic tips.

Fig. **27** (a) shows the effect of SOC for different E_j and spin-degeneracy, *i. e.,* $p_{j\uparrow}$ and $p_{j\downarrow}$ have the same initial energy. As mentioned in chapter **3**, no effect on the DOS occurs for this spin-degenerate case. To a first approximation the spin-degeneracy may be lifted by suppressing spin-mixing completely. Consequently, the hybridization via SOC is only described by the M matrix (see equation (28)) and the new energy eigenvalues ϵ are defined by

$$\begin{aligned} &(\epsilon - \mathrm{E}_x)(\epsilon - \mathrm{E}_y)(\epsilon - \mathrm{E}_z) = \dots \\ &\quad \dots \lambda^2 \left((\epsilon - \mathrm{E}_x)(\sin\theta \cos\phi)^2 + (\epsilon - \mathrm{E}_y)(\sin\theta \sin\phi)^2 + (\epsilon - \mathrm{E}_z)(\cos\theta)^2 \right) \end{aligned} \tag{32}$$

For equal $E_j = E$ the new eigenvalues E and $E \pm \lambda$ are independent of the angles θ and ϕ. This is verified by the total DOS in Fig. **27** (b) calculated for equal E_j and no spin-mixing. The projected DOS, however, depend on (θ, ϕ): For an orientation of the SQA in the j-direction ($j = x, y, z$) the p_j state remains an eigenstate with energy E and the other two states split by 2λ. Even though the total DOS remains independent of the orientation of the SQA, an effect in

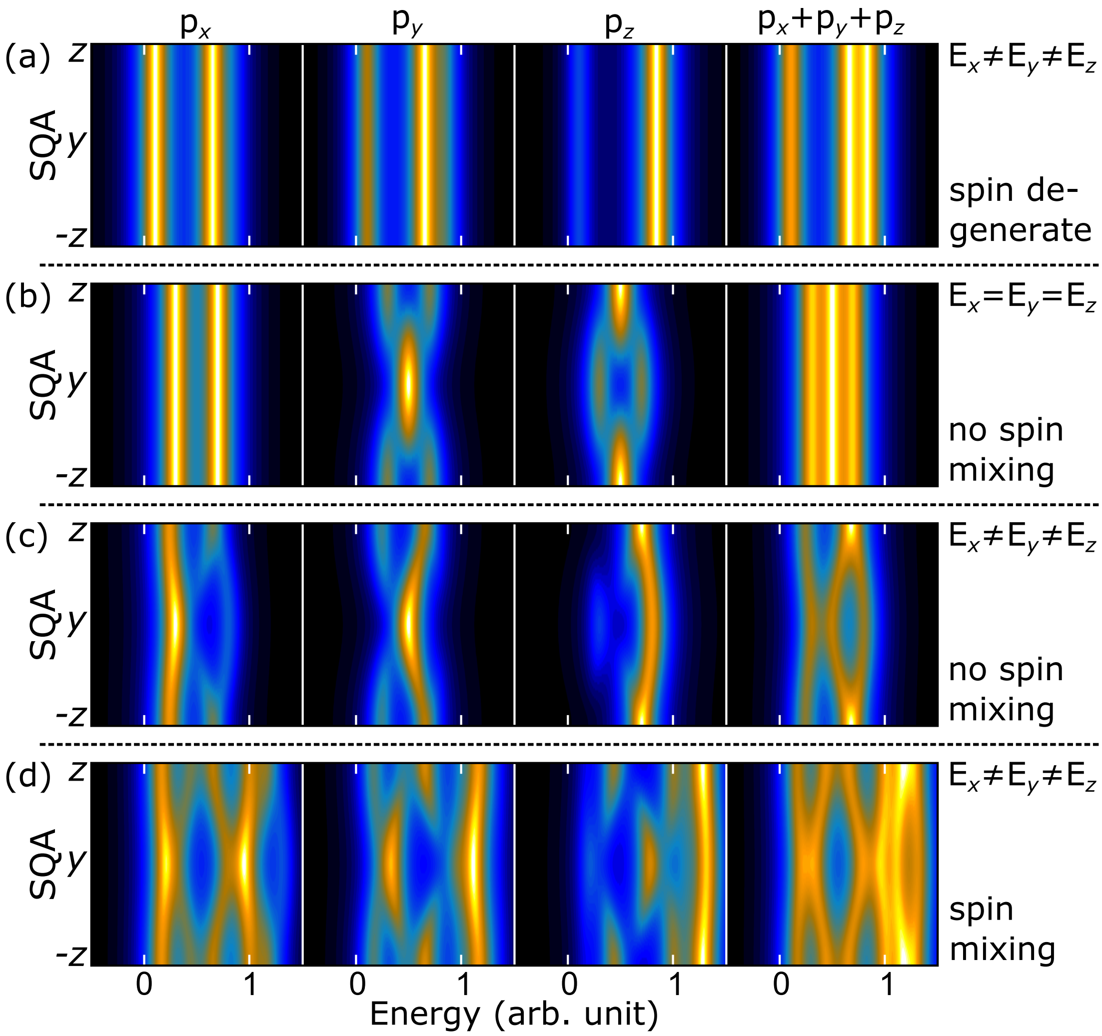

Figure 27. **Effect of SOC on the spin-averaged DOS of p states**

The effect of SOC on the projected and total DOS is illustrated for different choices of the eigenenergies E_j of the unperturbed p_j and different spin mixings in (a) to (d). The DOS were calculated for a spin-orbit parameter of $\lambda = 0.2\,\text{arb. unit}$ and a spin-quantization axis (SQA) rotating from $+z$ to $+y$ to $-z$. The color scale ranges from black (low) to blue to orange (high).

dI/dV spectra may be therefore be expected since the orbitals may contribute differently to the tunneling current. Considering adsorbates on a surface, the E_j are generally different because the states hybridize differently with states of the substrate. Fig. **27** (c) therefore shows the DOS for different E_j and suppressed spin-mixing. In agreement with equation (32) the p_j state is an eigenfunction for an orientation of the SQA along the $\pm j$ direction (here: p_z for $\pm z$ and p_y for

y). The DOS of the different states now show a more complex behavior than in Fig. **27** (b) resulting in a dependence of the total DOS on the orientation of the SQA.

The most general case is shown in Fig. **27** (d) with different E_j and a Zeeman energy that is comparable to the SOC strength. Consequently, all states – spin-up and spin-down – are hybridized via SOC. This results in a complex dependence of all DOS on the orientation of the SQA.

As pointed out, the E_j are expected to be different for adsorbates. Consequently, Fig. **27** (a), (c) and (d) show the behaviors of the DOS that might occur in experiments for different degrees of spin-lifting. In experiments the spins are separated in energy by exchange coupling or by an external magnetic field. Exchange coupling typically results in a shift of the majority and minority states by several 100 meV to eV against each other [4, 15, 37, 155]. Consequently, the behavior of the DOS on the orientation of the spin-quantization axis may resemble the DOS in Fig. **27** (c) and (d). Spin-lifting via an external magnetic field, however, results in a much weaker splitting of $\approx 0.1\,\mathrm{meV/T}$. Depending on the energy resolution, magnetic fields of several Tesla are therefore needed to observe an effect on the DOS. The DOS may therefore resemble Fig. **27** (a) for this case.

However, the advantages of exchange coupling and an external magnetic field may be combined: For ferromagnetic substrates the spins are split due to exchange coupling and their magnetization direction may be oriented with an external magnetic field.

(b) Height correction of dI/dV and conductance curves

In this thesis adsorbates are compared that are coupled to differently magnetized environments. To this end relative differences are calculated from $\mathrm{d}I/\mathrm{d}V$ or conductance curves measured on these adsorbates. Prior to acquiring these data the tip is stabilized at a tip-sample distance above the adsorbate that is controlled by keeping the tunneling current at a constant value. The current in turn is dependent on the probed DOS, which changes either due to SOC or due to the relative orientations between the magnetizations of tip and sample. Consequently, the apparent heights of the adsorbates and thus the tip-adsorbate separation vary. Here, the influence of this apparent height difference is discussed.

In spin-polarized measurements, the conductance asymmetry A, which is calculated from $\mathrm{d}I/\mathrm{d}V$ curves, is linked to the spin polarizations of tip and sample $P_{\mathrm{T,S}}$ via $A = P_{\mathrm{T}}\,P_{\mathrm{S}}$ in a first approximation (see chapter **2**). This relation is derived under the assumption that the $\mathrm{d}I/\mathrm{d}V$ curves are measured at the same tip-sample distance, resulting in a cancellation of the transmission factors τ (see equation (2) in chapter **2**). The effect of a vertical displacement is illustrated by the asymmetry of two $\mathrm{d}I/\mathrm{d}V$ curves measured at heights z and $z + \Delta z$:

$$\begin{aligned} A &= \frac{\mathrm{d}I/\mathrm{d}V_1(z) - \mathrm{d}I/\mathrm{d}V_2(z+\Delta z)}{\mathrm{d}I/\mathrm{d}V_1(z) + \mathrm{d}I/\mathrm{d}V_2(z+\Delta z)} = \frac{\mathrm{d}I/\mathrm{d}V_1(z) - \mathrm{d}I/\mathrm{d}V_2(z)\,e^{-2\kappa\,\Delta z}}{\mathrm{d}I/\mathrm{d}V_1(z) + \mathrm{d}I/\mathrm{d}V_2(z)\,e^{-2\kappa\,\Delta z}} \\ &= \frac{\mathrm{d}I/\mathrm{d}V_1(z) - \mathrm{d}I/\mathrm{d}V_2(z)}{\mathrm{d}I/\mathrm{d}V_1(z) + \mathrm{d}I/\mathrm{d}V_2(z)} + \frac{2 - 2\,e^{-2\kappa\,\Delta z}}{(1 + \frac{\mathrm{d}I/\mathrm{d}V_1(z)}{\mathrm{d}I/\mathrm{d}V_2(z)}) + (1 + \frac{\mathrm{d}I/\mathrm{d}V_2(z)}{\mathrm{d}I/\mathrm{d}V_1(z)})\,e^{-2\kappa\,\Delta z}} \end{aligned} \tag{33}$$

The first term is the asymmetry with $\mathrm{d}I/\mathrm{d}V$ curves measured at the same height and is thus linked to the spin polarization by the relation given above. The second term may be simplified because $\kappa \approx 1\,\mathring{\mathrm{A}}^{-1}$ for metals and Δz is typically on the order of $(1 - 10)\,\mathrm{pm}$. Consequently, the exponential term can be approximated and equation (33) modifies to

$$A \approx P_{\mathrm{T}}\,P_{\mathrm{S}} + \frac{4\,\kappa\,\Delta z}{2 + \frac{\mathrm{d}I/\mathrm{d}V_1(z)}{\mathrm{d}I/\mathrm{d}V_2(z)} + \frac{\mathrm{d}I/\mathrm{d}V_2(z)}{\mathrm{d}I/\mathrm{d}V_1(z)}}. \tag{34}$$

The upper limit of the second term is given for $\mathrm{d}I/\mathrm{d}V_1(z) = \mathrm{d}I/\mathrm{d}V_2(z)$, which results in

$$A \approx P_{\mathrm{T}}\,P_{\mathrm{S}} + \kappa\,\Delta z. \tag{35}$$

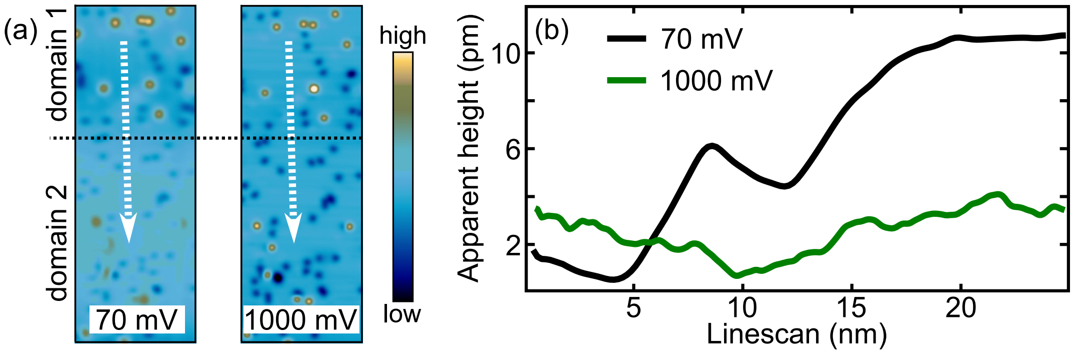

Figure 28. **Apparent height differences of spin-polarized data**

(a) Constant current topographs of the same area at two different bias voltages ($13 \times 36\,\mathrm{nm}^2$) measured with a spin-polarized tip. The boundary between two Fe domains is indicated with the horizontal dashed line. (b) Linescans across the vertical dashed lines in (a) display the dependence of the apparent height difference on the bias voltage.

A height difference of a few pm may thus be described as a shift of the asymmetry by roughly the pm value in %, which must not be confused with the spin polarization and therefore has to be considered in the experiment. A similar relation may be derived for the TAMR (see chapter **7** equation (24)). The effect of height differences on the (B)AMR is given by equation (26) in chapter **8**. For these quantities the correction of the apparent height differences enables a direct comparison with theoretical results, which are calculated for a fixed distance from the atomic core. Additionally, the results are rendered independent from the parameters used to stabilize the tip height prior to the measurements to a first approximation.

However, apparent height differences in TAMR and (B)AMR experiments are generally much smaller than in spin-polarized measurements. Indeed, SOC is changing the tunneling current by a smaller amount than spin-dependent tunneling does. The procedure used to correct height differences is thus illustrated using spin-polarized results (see Refs. [101] and [15]).

Apparent height differences can be reduced by stabilizing the tip height at certain bias voltages, which is illustrated in Fig. **28** (a) by constant current topographs of the same area at two different bias voltages. Linescans show that an apparent height difference of ≈ 10 pm between the domains occurs at 70 mV,

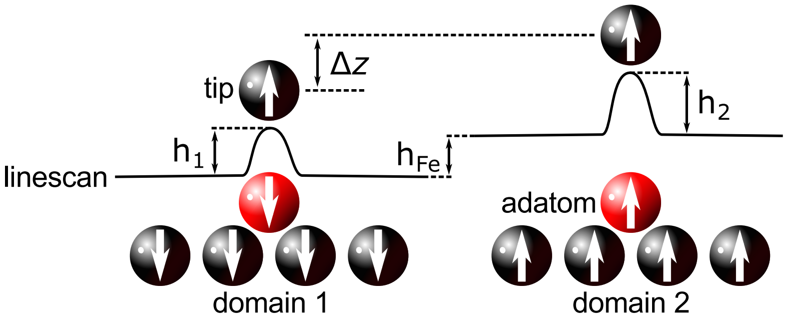

Figure 29. **Principle for correcting height differences**

The tip-adatom separation differs by Δz between adatoms that are adorbed on domains with antiparallel alignment of their magnetizations. Δz is extracted from the apparent heights $h_{1,2}$ of the adatoms and the apparent height difference between the domains h_{Fe}.

which vanishes at 1000 mV (Fig. **28** (b)).

Remaining apparent height difference Δz between adatoms can be corrected for by measuring the apparent heights $h_{1,2}$ of adatoms on oppositely magnetized domains and the apparent height difference h_{Fe} between these domains. The apparent heights were extracted from constant-current topographs by fitting the adatoms with 2D Gaussians and by taking linescans across the domains (see Fig. **28**). Fig. **29** illustrates the correction procedure for $h_2 > h_1$ and positive h_{Fe}. Consequently, the tip-adatom separation is larger on domain 2 than on domain 1 by $\Delta z = (h_{\mathrm{Fe}} + h_2) - h_1 > 0$. The $\mathrm{d}I/\mathrm{d}V$ curve of the atom on domain 2 has to be multiplied by a factor of $\exp(2\kappa\,\Delta z)$, *i. e.*, the $\mathrm{d}I/\mathrm{d}V$ is increased. In case of the (B)AMR the conductance curve of this atom has to be shifted by Δz to smaller tip-adatom separations. For the Ir adatoms, whose $\mathrm{d}I/\mathrm{d}V$ curves are shown in Fig. **9** (c) in chapter **6**, an apparent height difference of $\Delta z = (4.9 \pm 0.4)$ pm was measured at a bias voltage of 1000 mV. The correction of this difference resulted in a rather rigid shift for the asymmetry by (4.4 ± 0.8) % in agreement to the estimation given by equation (35). For these corrections the decay constant $\kappa = (0.96 \pm 0.09)\,\text{Å}^{-1}$ was extracted from conductance curves.

(c) Setup of a high temperature manipulator

The experiments presented in this thesis were done on a Fe bilayer adsorbed on a W(110) surface. To ensure a smooth surface of the Fe layer the W surface was cleaned from C impurities and tungsten oxides generated in O_2 cycles. Tungsten oxides evaporate at a temperature of $T_{110} = 2200\,\mathrm{K}$ from the (110) surface and $T_{001} = 2500\,\mathrm{K}$ from the (001) surface [68, 156, 157]. These temperatures are achieved by applying a high voltage to the crystal, which attracts and accelerates electrons emitted from a W filament. At these elevated temperatures radiation is the main energy drain. Consequently, the required electrical power P can be estimated using the Stefan-Boltzmann law $P = \sigma\, A\, \epsilon_t(T)\, T^4$ (σ: Stefan-Boltzmann constant, A: radiating surface area, ϵ_t: total emissivity). The W(110) [W(001)] crystal requires an electrical power of $P_{110} = 190\,\mathrm{W}$ [$P_{001} = 360\,\mathrm{W}$] for the surface area of the Ta sample holder of $A = 580\,\mathrm{mm}^2$ and a total emissivity of $\epsilon_t(2200\,\mathrm{K}) = 0.25$ [$\epsilon_t(2500\,\mathrm{K}) = 0.28$] [158]. This is, however, a lower boundary because the sample is mounted on a station during preparation and thus a substantially higher area might be expected to radiate power. Since the current of the available high voltage power supply is limited to 200 mA, several kV need to be applied to the sample. Consequently, a station suitable for W preparation must sustain high temperatures while maintaining an electrical insulation of the crystal.

The original preparation station used alumina ceramics (Al_2O_3) mounted close to the crystal for insulation. However, the capabilities of the ceramics were overestimated in this design: First, alumina melts at 2300 K rendering it useless for a W(001) preparation [122]. Second, its resistivity drops by nine orders of magnitude from room temperature to 1300 K [122]. Extrapolating this trend to 2200 K results in a resistance on the order of one Ohm or below for the mounted ceramics. Consequently, the electrical insulation breaks down at these temperatures setting different parts of the station to high voltage. A reliable preparation of W was thus not possible.

In the course of this thesis two new stations were built. Design considerations and their performance are described below. The main design criterion for both

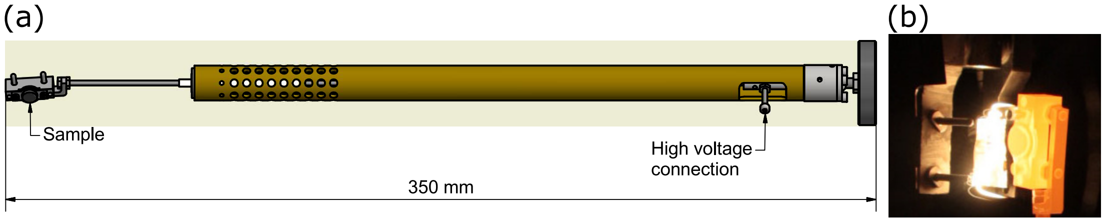

Figure 30. **Design of the first preparation station**

(a) The sample is positioned at the end of a Mo rod, which is clamped at the right side by a screw set to high voltage. To increase the mechanical stability the rod is embedded in a stainless steel tube from which it is insulated using alumina. Due to space limitations the station has to fit through a DN 16 Conflat Flange. (b) Photograph of the W(110) crystal mounted on a sample holder. The filament of the original station (left) is used to heat the crystal to 1500 K.

stations follows directly from the limitations of alumina, *i. e.,* no ceramics must be mounted close to the sample. Another criterion is the reduction of radiation losses by minimizing the surface area close to the sample.

The first station is depicted in Fig. **30** (a). It is mainly a support for the sample holder, which is set to high voltages. The electrons required for heating are emitted from the filament of the orginal station (Fig. **30** (b)). All experiments shown in this thesis were successfully prepared with this station. Due to space limitations the station has to fit through a DN 16 Conflat flange, which resulted in a reduced mechanical stability in comparison to the original station.

The second station, shown in Fig. **31**, was built to overcome these stability issues and as a replacement for the original station. Omitting the ceramics close to the sample resulted in a larger part of the station being at a high voltage as shown in red in Fig. **31** (a). A direct heating of this part is prevented by shields blocking the electrons. They additionally reflect radiation and thus minimize the required electrical power. The shields and most of the station are made from 99.9 % pure Mo. However, the rod supporting the sample is made from Ta because its vapor pressure at 2200 K is two orders of magnitude smaller than for Mo [122]. Ta was not used for the whole station because it is harder to machine and softer than Mo.

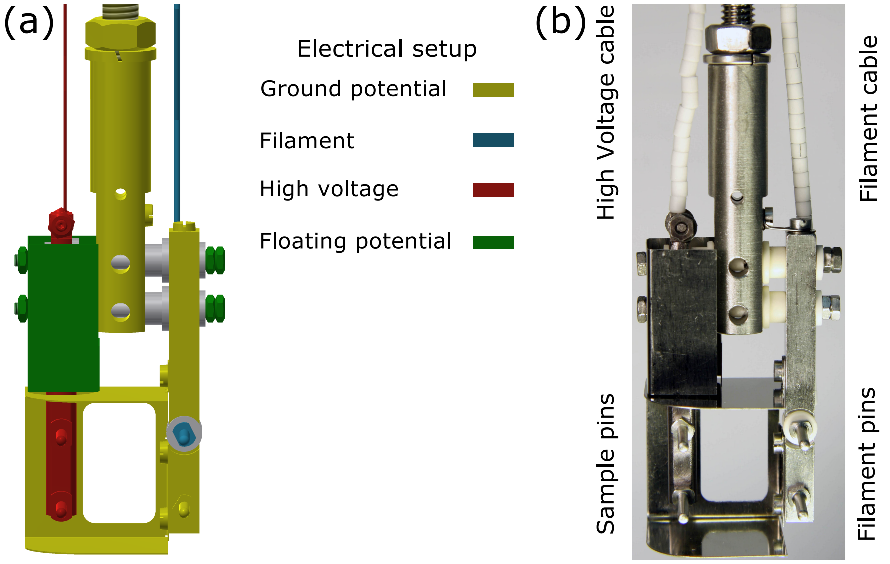

Figure 31. **Design of the second preparation station**

(a) Computer-aided design assembly. Colors indicate the electrical layout. High voltage and filament voltage are insulated from the ground potential by alumina ceramics (white). No ceramics are mounted close to the left pins, which carry the sample holder. (b) Assembled station. The maximum width of the station is 35 mm allowing it to travel through a DN 40 Conflat flange.

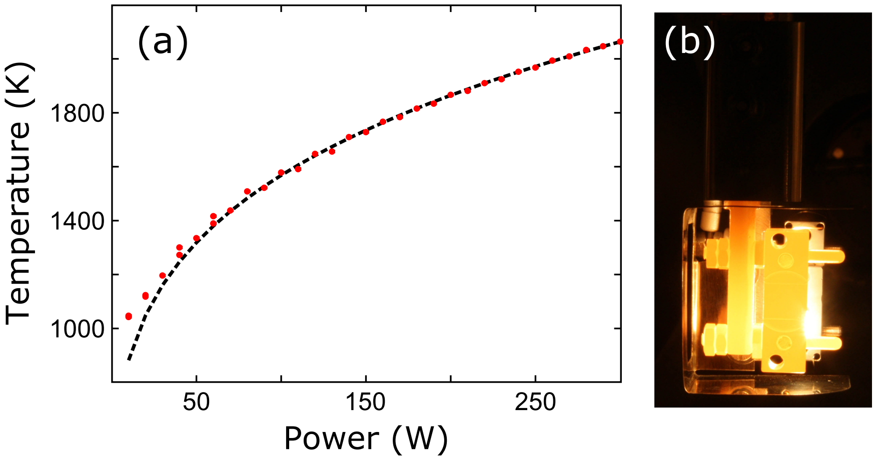

Figure 32. **Performance of the second preparation station**

(a) The temperature of a Ta sample holder mounted on the new preparation station was measured with a pyrometer (emissivity 0.25 (see Ref. [158])). The dashed line corresponds to a fit to the Stefan-Boltzmann law. (b) Photograph of the station at a temperature of the Ta sample holder of 1700 K.

Fig. **31** (b) shows the assembled station. To test its performance the temperature T of a Ta sample holder was measured with a pyrometer for various electrical heating powers P and an emissivity of 0.25 [158]. The data was fitted to the Stefan-Boltzmann law via $T = \sqrt[4]{P/(\sigma\,\epsilon_t\,A_{\text{eff}})}$ to determine the effective radiating area A_{eff}. The data and the fit are displayed in Fig. **32** (a). For elevated temperatures the data and the fit agree well, which confirms that energy is mainly drained by radiation. At smaller powers the measured temperature is higher than the fit suggests supposedly because of the additional heating due to thermal radiation of the filament.

The fit yields an effective radiating area of 1170 mm^2. This corresponds to the approximate size of two sample holders, which appears reasonable regarding the glowing area in Fig. **32** (b). Consequently, the electrical powers needed for W preparation are twice as large with respect to the estimation given at the beginning of this paragraph: For a temperature of 2200 K (2500 K) a total electrical power of 390 W (720 W) is needed. The long term stability of the station was tested by keeping it at 2060 K (300 W) for eight hours with no visible degradation. Future preparations of W but also other single crystals with lower melting points like Au or Ir are thus feasible with this station.

References

[1] M. N. Baibich, J. M. Broto, A. Fert, F. Nguyen Van Dau, F. Petroff, P. Etienne, G. Creuzet, A. Friederich, and J. Chazelas, *Giant magnetoresistance of (001)Fe/(001)Cr magnetic superlattices,* Phys. Rev. Lett. **61**, 2472 (1988).

[2] G. Binasch, P. Grünberg, F. Saurenbach, and W. Zinn, *Enhanced magnetoresistance in layered magnetic structures with antiferromagnetic interlayer exchange,* Phys. Rev. B **39**, 4828 (1989).

[3] G. Bertero, G. Guo, S. Dahandeh, and A. Krishnan, *Hard Disk Drives: Fundamentals and Perspectives*, edited by G. Varvaro and F. Casoli (Informa UK Limited, 2016) pp. 51–131.

[4] J. Stöhr and H. C. Siegmann, *Magnetism From Fundamentals to Nanoscale Dynamics* (Springer Berlin Heidelberg, 2006).

[5] G. Binnig, H. Rohrer, C. Gerber, and E. Weibel, *Surface studies by scanning tunneling microscopy,* Phys. Rev. Lett. **49**, 57 (1982).

[6] G. Binnig, H. Rohrer, C. Gerber, and E. Weibel, *Tunneling through a controllable vacuum gap,* Appl. Phys. Lett. **40**, 178 (1982).

[7] D. M. Eigler and E. K. Schweizer, *Positioning single atoms with a scanning tunnelling microscope,* Nature **344**, 524 (1990).

[8] R. Wiesendanger, H.-J. Güntherodt, G. Güntherodt, R. J. Gambino, and R. Ruf, *Observation of vacuum tunneling of spin-polarized electrons with the scanning tunneling microscope,* Phys. Rev. Lett. **65**, 247 (1990).

[9] M. Bode, *Spin-polarized scanning tunnelling microscopy,* Rep. Prog. Phys. **66**, 523 (2003).

[10] R. Wiesendanger, *Spin mapping at the nanoscale and atomic scale,* Rev. Mod. Phys. **81**, 1495 (2009).

[11] Y. Yayon, V. Brar, L. Senapati, S. Erwin, and M. Crommie, *Observing spin polarization of individual magnetic adatoms,* Phys. Rev. Lett. **99**, 067202 (2007).

[12] B. W. Heinrich, C. Iacovita, M. V. Rastei, L. Limot, J. P. Bucher, P. A. Ignatiev, V. S. Stepanyuk, and P. Bruno, *Spin structure of an atomic protrusion: Probing single atoms on cobalt nanoislands,* Phys. Rev. B **79**, 113401 (2009).

[13] D. Serrate, P. Ferriani, Y. Yoshida, S.-W. Hla, M. Menzel, K. von Bergmann, S. Heinze, A. Kubetzka, and R. Wiesendanger, *Imaging and manipulating the spin direction of individual atoms,* Nat. Nanotech. **5**, 350 (2010).

[14] M. Polok, D. V. Fedorov, A. Bagrets, P. Zahn, and I. Mertig, *Evaluation of conduction eigenchannels of an adatom probed by an STM tip,* Phys. Rev. B **83**, 245426 (2011).

[15] N. Néel, P. Ferriani, M. Ziegler, S. Heinze, J. Kröger, and R. Berndt, *Energy-resolved spin-polarized tunneling and exchange coupling of Co and Cr atoms on Fe islands on W(110),* Phys. Rev. B **85**, 155406 (2012).

[16] P. Gambardella, S. Rusponi, M. Veronese, S. S. Dhesi, C. Grazioli, A. Dallmeyer, I. Cabria, R. Zeller, P. H. Dederichs, K. Kern, C. Carbone, and H. Brune, *Giant magnetic anisotropy of single cobalt atoms and nanoparticles,* Science **300**, 1130 (2003).

[17] C. F. Hirjibehedin, C.-Y. Lin, A. F. Otte, M. Ternes, C. P. Lutz, B. A. Jones, and A. J. Heinrich, *Large magnetic anisotropy of a single atomic spin embedded in a surface molecular network,* Science **317**, 1199 (2007).

[18] S. Loth, M. Etzkorn, C. P. Lutz, D. M. Eigler, and A. J. Heinrich, *Measurement of fast electron spin relaxation times with atomic resolution,* Science **329**, 1628 (2010).

[19] A. A. Khajetoorians, S. Lounis, B. Chilian, A. T. Costa, L. Zhou, D. L. Mills, J. Wiebe, and R. Wiesendanger, *Itinerant nature of atom-magnetization excitation by tunneling electrons,* Phys. Rev. Lett. **106**, 037205 (2011).

[20] I. G. Rau, S. Baumann, S. Rusponi, F. Donati, S. Stepanow, L. Gragnaniello, J. Dreiser, C. Piamonteze, F. Nolting, S. Gangopadhyay, O. R. Albertini, R. M. Macfarlane, C. P. Lutz, B. A. Jones, P. Gambardella, A. J. Heinrich, and H. Brune, *Reaching the magnetic anisotropy limit of a 3d metal atom,* Science **344**, 988 (2014).

[21] S. Yan, D.-J. Choi, J. A. J. Burgess, S. Rolf-Pissarczyk, and S. Loth, *Three-dimensional mapping of single-atom magnetic anisotropy,* Nano Lett. **15**, 1938 (2015).

[22] A. A. Khajetoorians, J. Wiebe, B. Chilian, and R. Wiesendanger, *Realizing*

all-spin-based logic operations atom by atom, Science **332**, 1062 (2011).

[23] S. Loth, S. Baumann, C. P. Lutz, D. M. Eigler, and A. J. Heinrich, *Bistability in atomic-scale antiferromagnets,* Science **335**, 196 (2012).

[24] M. Bode, S. Heinze, A. Kubetzka, O. Pietzsch, X. Nie, G. Bihlmayer, S. Blügel, and R. Wiesendanger, *Magnetization-direction-dependent local electronic structure probed by scanning tunneling spectroscopy,* Phys. Rev. Lett. **89**, 237205 (2002).

[25] N. Néel, S. Schröder, N. Ruppelt, P. Ferriani, J. Kröger, R. Berndt, and S. Heinze, *Tunneling anisotropic magnetoresistance at the single-atom limit,* Phys. Rev. Lett. **110**, 037202 (2013).

[26] J. Tersoff and D. R. Hamann, *Theory and application for the scanning tunneling microscope,* Phys. Rev. Lett. **50**, 1998 (1983).

[27] J. Tersoff and D. R. Hamann, *Theory of the scanning tunneling microscope,* Phys. Rev. B **31**, 805 (1985).

[28] D. Wortmann, S. Heinze, Ph. Kurz, G. Bihlmayer, and S. Blügel, *Resolving complex atomic-scale spin structures by spin-polarized scanning tunneling microscopy,* Phys. Rev. Lett. **86**, 4132 (2001).

[29] J. G. Simmons, *Generalized formula for the electric tunnel effect between similar electrodes separated by a thin insulating film,* J. Appl. Phys. **34**, 1793 (1963).

[30] C. J. Chen, *Introduction to Scanning Tunneling Microscopy* (Oxford University Press, 1993).

[31] T. Fließbach, *Quantenmechanik* (Springer Spektrum, 2008).

[32] M. Julliere, *Tunneling between ferromagnetic films,* Phys. Lett. A **54**, 225 (1975).

[33] W. Demtröder, *Experimentalphysik 3* (Springer Berlin Heidelberg, 2010).

[34] R. M. White, *Quantum Theory of Magnetism*, 3rd ed. (Springer, 2006).

[35] F. Schwabl, *Quantenmechanik (QM I): Eine Einführung* (Springer-Lehrbuch, 2007).

[36] E. Abate and M. Asdente, *Tight-binding calculation of 3d bands of Fe with and without spin-orbit coupling,* Phys. Rev. **140**, A1303 (1965).

[37] S. Schröder, *First-Principles Study of Non-Collinear Magnetism and Spin-Orbit Driven Physics in Nanostructures at Surfaces*, Ph.D. thesis, Christian-Albrechts-

Universität zu Kiel (2013).

[38] R. J. Elliott, *Spin-orbit coupling in band theory-character tables for some "double" space groups,* Phys. Rev. **96**, 280 (1954).

[39] C. Li, A. J. Freeman, H. J. F. Jansen, and C. L. Fu, *Magnetic anisotropy in low-dimensional ferromagnetic systems: Fe monolayers on Ag(001), Au(001), and Pd(001) substrates,* Phys. Rev. B **42**, 5433 (1990).

[40] C. Gould, C. Rüster, T. Jungwirth, E. Girgis, G. M. Schott, R. Giraud, K. Brunner, G. Schmidt, and L. W. Molenkamp, *Tunneling anisotropic magnetoresistance: A spin-valve-like tunnel magnetoresistance using a single magnetic layer,* Phys. Rev. Lett. **93**, 117203 (2004).

[41] U. Gradmann and G. Waller, *Periodic lattice distortions in epitaxial films of Fe(110) on W(110),* Surf. Sci **116**, 539 (1982).

[42] R. Kurzawa, K.-P. Kämper, W. Schmitt, and G. Güntherodt, *Spin-resolved photoemission study of in situ grown epitaxial Fe layers on W(110),* Solid State Commun. **60**, 777 (1986).

[43] H. J. Elmers, J. Hauschild, H. Fritzsche, G. Liu, U. Gradmann, and U. Köhler, *Magnetic frustration in ultrathin Fe films,* Phys. Rev. Lett. **75**, 2031 (1995).

[44] C. Jensen, K. Reshöft, and U. Köhler, *Direct observation of strain relaxation in iron layers on W(110) by time-resolved STM,* Appl. Phys. A **62**, 217 (1996).

[45] J. Hauschild, U. Gradmann, and H. J. Elmers, *Perpendicular magnetization and dipolar antiferromagnetism in double layer nanostripe arrays of Fe(110) on W(110),* Appl. Phys. Lett. **72**, 3211 (1998).

[46] H. J. Elmers, J. Hauschild, and U. Gradmann, *Onset of perpendicular magnetization in nanostripe arrays of Fe on stepped W(110) surfaces,* Phys. Rev. B **59**, 3688 (1999).

[47] D. Sander, R. Skomski, C. Schmidthals, A. Enders, and J. Kirschner, *Film stress and domain wall pinning in sesquilayer iron films on W(110),* Phys. Rev. Lett. **77**, 2566 (1996).

[48] X. Qian and W. Hübner, *First-principles calculation of structural and magnetic properties for Fe monolayers and bilayers on W(110),* Phys. Rev. B **60**, 16192 (1999).

[49] O. Pietzsch, A. Kubetzka, M. Bode, and R. Wiesendanger, *Real-space observation of dipolar antiferromagnetism in magnetic nanowires by spin-polarized scanning tunneling spectroscopy,* Phys. Rev. Lett. **84**, 5212 (2000).

[50] M. Bode, O. Pietzsch, A. Kubetzka, S. Heinze, and R. Wiesendanger, *Experimental evidence for intra-atomic noncollinear magnetism at thin film probe tips,* Phys. Rev. Lett. **86**, 2142 (2001).

[51] A. Kubetzka, O. Pietzsch, M. Bode, and R. Wiesendanger, *Magnetism of nanoscale Fe islands studied by spin-polarized scanning tunneling spectroscopy,* Phys. Rev. B **63**, 140407 (R) (2001).

[52] A. Kubetzka, M. Bode, O. Pietzsch, and R. Wiesendanger, *Spin-polarized scanning tunneling microscopy with antiferromagnetic probe tips,* Phys. Rev. Lett. **88**, 057201 (2002).

[53] M. Bode, A. Kubetzka, S. Heinze, O. Pietzsch, R. Wiesendanger, M. Heide, X. Nie, G. Bihlmayer, and S. Blügel, *Spin-orbit induced local band structure variations revealed by scanning tunnelling spectroscopy,* J. Phys.: Condens. Matter **15**, S679 (2003).

[54] K. von Bergmann, M. Bode, A. Kubetzka, M. Heide, S. Blügel, and R. Wiesendanger, *Spin-polarized electron scattering at single oxygen adsorbates on a magnetic surface,* Phys. Rev. Lett. **92**, 046801 (2004).

[55] M. Bode, K. von Bergmann, O. Pietzsch, A. Kubetzka, and R. Wiesendanger, *Spin-polarized scanning tunneling spectroscopy of dislocation lines in Fe films on W(110),* J. Magn. Magn. Mater. **304**, 1 (2006).

[56] S. Meckler, N. Mikuszeit, A. Pressler, E. Y. Vedmedenko, O. Pietzsch, and R. Wiesendanger, *Real-space observation of a right-rotating inhomogeneous cycloidal spin spiral by spin-polarized scanning tunneling microscopy in a triple axes vector magnet,* Phys. Rev. Lett. **103**, 157201 (2009).

[57] J. Brede, N. Atodiresei, S. Kuck, P. Lazić, V. Caciuc, Y. Morikawa, G. Hoffmann, S. Blügel, and R. Wiesendanger, *Spin- and energy-dependent tunneling through a single molecule with intramolecular spatial resolution,* Phys. Rev. Lett. **105**, 047204 (2010).

[58] N. Atodiresei, J. Brede, P. Lazić, V. Caciuc, G. Hoffmann, R. Wiesendanger,

and S. Blügel, *Design of the local spin polarization at the organic-ferromagnetic interface,* Phys. Rev. Lett. **105**, 066601 (2010).

[59] L. Z. Mezey and J. Giber, *Calculation of surface free energies and characteristics of surface segregation of solids,* Surf. Sci **117**, 220 (1982).

[60] H. J. Elmers, G. Liu, and U. Gradmann, *Magnetometry of the ferromagnetic monolayer Fe(110) on W(110) coated with Ag,* Phys. Rev. Lett. **63**, 566 (1989).

[61] H. Bethge, D. Heuer, Ch. Jensen, K. Reshöft, and U. Köhler, *Misfit-related effects in the epitaxial growth of iron on W(110),* Surf. Sci. **331-333**, 878 (1995).

[62] U. Gradmann, J. Korecki, and G. Waller, *In-plane magnetic surface anisotropies in Fe(110),* Appl. Phys. A **39**, 101 (1986).

[63] U. Gradmann, M. Przybylski, H. J. Elmers, and G. Liu, *Ferromagnetism in the thermodynamically stable monolayer Fe(110) on W(110), coated by Ag,* Appl. Phys. A **49**, 563 (1989).

[64] H. J. Elmers, J. Hauschild, H. Höche, U. Gradmann, H. Bethge, D. Heuer, and U. Köhler, *Submonolayer magnetism of Fe(110) on W(110): Finite width scaling of stripes and percolation between islands,* Phys. Rev. Lett. **73**, 898 (1994).

[65] N. Weber, K. Wagner, H. J. Elmers, J. Hauschild, and U. Gradmann, *Nanoscale spatial switching of magnetic anisotropy in pseudomorphic Fe(110) on W(110),* Phys. Rev. B **55**, 14121 (1997).

[66] A. Kubetzka, O. Pietzsch, M. Bode, and R. Wiesendanger, *Spin-polarized scanning tunneling microscopy study of* 360° *walls in an external magnetic field,* Phys. Rev. B **67**, 020401 (2003).

[67] M. Heide, G. Bihlmayer, and S. Blügel, *Dzyaloshinskii-moriya interaction accounting for the orientation of magnetic domains in ultrathin films: Fe/W(110),* Phys. Rev. B **78**, 140403 (2008).

[68] R. G. Musket, W. McLean, C. A. Colmenares, D. M. Makowiecki, and W. J. Siekhaus, *Preparation of atomically clean surfaces of selected elements: A review,* Appl. Surf. Sci. **10**, 143 (1982).

[69] J. K. Gimzewski and R. Müller, *Transition from the tunneling regime to point contact studied using scanning tunneling microscopy,* Phys. Rev. B **36**, 1284 (1987).

[70] C. Joachim, J. K. Gimzewski, R. R. Schlittler, and C. Chavy, *Electronic trans-*

parence of a single C60 molecule, Phys. Rev. Lett. **74**, 2102 (1995).

[71] A. Yazdani, D. M. Eigler, and N. D. Lang, *Off-resonance conduction through atomic wires,* Science **272**, 1921 (1996).

[72] J. Kröger, N. Néel, and L. Limot, *Contact to single atoms and molecules with the tip of a scanning tunnelling microscope,* J. Phys.: Condens. Matter **20**, 223001 (2008).

[73] N. Agraït, A. L. Yeyati, and J. M. Ruitenbeek, *Quantum properties of atomic-sized conductors,* Phys. Rep. **377**, 81 (2003).

[74] M. Brandbyge, J. Schiøtz, M. R. Sørensen, P. Stoltze, K. W. Jacobsen, J. K. Nørskov, L. Olesen, E. Laegsgaard, I. Stensgaard, and F. Besenbacher, *Quantized conductance in atom-sized wires between two metals,* Phys. Rev. B **52**, 8499 (1995).

[75] J. Kröger, H. Jensen, and R. Berndt, *Conductance of tip–surface and tip–atom junctions on Au(111) explored by a scanning tunnelling microscope,* New J. Phys. **9**, 153 (2007).

[76] R. Landauer, *Spatial variation of currents and fields due to localized scatterers in metallic conduction,* IBM J. Res. Dev. **1**, 223 (1957).

[77] M. Büttiker, *Coherent and sequential tunneling in series barriers,* IBM J. Res. Dev. **32**, 63 (1988).

[78] S. Joo, K. Y. Jung, K. I. Jun, D. S. Kim, K. H. Shin, J. K. Hong, B. C. Lee, and K. Rhie, *Spin-filtering effect of thin Al_2O_3 barrier on tunneling magnetoresistance,* Appl. Phys. Lett. **104**, 152407 (2014).

[79] A. Kalitsov, P.-J. Zermatten, F. Bonell, G. Gaudin, S. Andrieu, C. Tiusan, M. Chshiev, and J. P. Velev, *Bias dependence of tunneling magnetoresistance in magnetic tunnel junctions with asymmetric barriers,* J. Phys.: Condens. Matter **25**, 496005 (2013).

[80] A. Fert, A. Barthélémy, J. Ben Youssef, J.-P. Contour, V. Cros, J. M. De Teresa, A. Hamzic, J. M. George, G. Faini, J. Grollier, H. Jaffreés, H. Le Gall, F. Montaigne, F. Pailloux, and F. Petroff, *Review of recent results on spin polarized tunneling and magnetic switching by spin injection,* Mat. Sci. Eng. B **84**, 1 (2001).

[81] G.-X. Miao, M. Münzenberg, and J. S. Moodera, *Tunneling path toward spin-*

tronics, Rep. Prog. Phys. **74**, 036501 (2011).

[82] W. H. Butler, X.-G. Zhang, T. C. Schulthess, and J. M. MacLaren, *Spin-dependent tunneling conductance of Fe | MgO | Fe sandwiches,* Phys. Rev. B **63**, 054416 (2001).

[83] S. F. Alvarado, *Tunneling potential barrier dependence of electron spin polarization,* Phys. Rev. Lett. **75**, 513 (1995).

[84] W. Wulfhekel, H. F. Ding, and J. Kirschner, *Tunneling magnetoresistance through a vacuum gap,* J. Magn. Magn. Mater. **242-245**, 47 (2002).

[85] M. Eltschka, B. Jäck, M. Assig, O. V. Kondrashov, M. A. Skvortsov, M. Etzkorn, C. R. Ast, and K. Kern, *Probing absolute spin polarization at the nanoscale,* Nano Lett. **14**, 7171 (2014).

[86] M. Bode, M. Getzlaff, and R. Wiesendanger, *Spin-polarized vacuum tunneling into the exchange-split surface state of Gd(0001),* Phys. Rev. Lett. **81**, 4256 (1998).

[87] S. N. Okuno, T. Kishi, and K. Tanaka, *Spin-polarized tunneling spectroscopy of Co(0001) surface states,* Phys. Rev. Lett. **88**, 066803 (2002).

[88] O. Pietzsch, A. Kubetzka, M. Bode, and R. Wiesendanger, *Spin-polarized scanning tunneling spectroscopy of nanoscale cobalt islands on Cu(111),* Phys. Rev. Lett. **92**, 057202 (2004).

[89] C. Iacovita, M. V. Rastei, B. W. Heinrich, T. Brumme, J. Kortus, L. Limot, and J. P. Bucher, *Visualizing the spin of individual cobalt-phthalocyanine molecules,* Phys. Rev. Lett. **101**, 116602 (2008).

[90] J. Brede and R. Wiesendanger, *Spin-resolved characterization of single cobalt phthalocyanine molecules on a ferromagnetic support,* Phys. Rev. B **86**, 184423 (2012).

[91] L. Zhou, F. Meier, J. Wiebe, and R. Wiesendanger, *Inversion of spin polarization above individual magnetic adatoms,* Phys. Rev. B **82**, 012409 (2010).

[92] P. Ferriani, C. Lazo, and S. Heinze, *Origin of the spin polarization of magnetic scanning tunneling microscopy tips,* Phys. Rev. B **82**, 054411 (2010).

[93] M. Häfner, J. K. Viljas, D. Frustaglia, F. Pauly, M. Dreher, P. Nielaba, and J. C. Cuevas, *Theoretical study of the conductance of ferromagnetic atomic-sized*

contacts, Phys. Rev. B **77**, 104409 (2008).

[94] G. Kresse and J. Furthmüller, *Efficient iterative schemes for ab initio total-energy calculations using a plane-wave basis set,* Phys. Rev. B **54**, 11169 (1996).

[95] G. Kresse and D. Joubert, *From ultrasoft pseudopotentials to the projector augmented-wave method,* Phys. Rev. B **59**, 1758 (1999).

[96] B. Hammer, L. B. Hansen, and J. K. Nørskov, *Improved adsorption energetics within density-functional theory using revised Perdew-Burke-Ernzerhof functionals,* Phys. Rev. B **59**, 7413 (1999).

[97] J. P. Perdew and A. Zunger, *Self-interaction correction to density-functional approximations for many-electron systems,* Phys. Rev. B **23**, 5048 (1981).

[98] D. M. Ceperley and B. J. Alder, *Ground state of the electron gas by a stochastic method,* Phys. Rev. Lett. **45**, 566 (1980).

[99] P. E. Blöchl, *Projector augmented-wave method,* Phys. Rev. B **50**, 17953 (1994).

[100] H. J. Monkhorst and J. D. Pack, *Special points for Brillouin-zone integrations,* Phys. Rev. B **13**, 5188 (1976).

[101] A. Kubetzka, O. Pietzsch, M. Bode, and R. Wiesendanger, *Determining the spin polarization of surfaces by spin-polarized scanning tunneling spectroscopy,* Appl. Phys. A **76**, 873 (2003).

[102] M. Ziegler, N. Ruppelt, N. Néel, J. Kröger, and R. Berndt, *Control of spin-polarized current in a scanning tunneling microscope by single-atom transfer,* Appl. Phys. Lett. **96**, 132505 (2010).

[103] P. M. Tedrow and R. Meservey, *Spin polarization of electrons tunneling from films of Fe, Co, Ni, and Gd,* Phys. Rev. B **7**, 318 (1973).

[104] W. A. Hofer, A. J. Fisher, R. A. Wolkow, and P. Grütter, *Surface relaxations, current enhancements, and absolute distances in high resolution scanning tunneling microscopy,* Phys. Rev. Lett. **87**, 236104 (2001).

[105] L. Limot, J. Kröger, R. Berndt, A. Garcia-Lekue, and W. A. Hofer, *Atom transfer and single-adatom contacts,* Phys. Rev. Lett. **94**, 126102 (2005).

[106] J. M. D. Coey, *Magnetism and Magnetic Materials* (Cambridge University Press, 2010).

[107] K. I. Bolotin, F. Kuemmeth, and D. C. Ralph, *Anisotropic magnetoresistance*

and anisotropic tunneling magnetoresistance due to quantum interference in ferromagnetic metal break junctions, Phys. Rev. Lett. **97**, 127202 (2006).

[108] M. Viret, M. Gabureac, F. Ott, C. Fermon, C. Barreteau, G. Autes, and R. Guirado-Lopez, *Giant anisotropic magneto-resistance in ferromagnetic atomic contacts,* Eur. Phys. J. B **51**, 1 (2006).

[109] J. D. Burton, R. F. Sabirianov, J. P. Velev, O. N. Mryasov, and E. Y. Tsymbal, *Effect of tip resonances on tunneling anisotropic magnetoresistance in ferromagnetic metal break-junctions: A first-principles study,* Phys. Rev. B **76**, 144430 (2007).

[110] N. M. Caffrey, S. Schröder, P. Ferriani, and S. Heinze, *Tunneling anisotropic magnetoresistance effect of single adatoms on a noncollinear magnetic surface,* J. Phys.: Condens. Matter **26**, 394010 (2014).

[111] F. Strigl, C. Espy, M. Bückle, E. Scheer, and T. Pietsch, *Emerging magnetic order in platinum atomic contacts and chains,* Nat. Comms. **6**, 6172 (2015).

[112] J. A. Stroscio and D. M. Eigler, *Atomic and molecular manipulation with the scanning tunneling microscope,* Science **254**, 1319 (1991).

[113] A. A. Khajetoorians, T. Schlenk, B. Schweflinghaus, M. dos Santos Dias, M. Steinbrecher, M. Bouhassoune, S. Lounis, J. Wiebe, and R. Wiesendanger, *Spin excitations of individual Fe atoms on Pt(111): Impact of the site-dependent giant substrate polarization,* Phys. Rev. Lett. **111**, 157204 (2013).

[114] F. Meier, L. Zhou, J. Wiebe, and R. Wiesendanger, *Revealing magnetic interactions from single-atom magnetization curves,* Science **320**, 82 (2008).

[115] T. Balashov, T. Schuh, A. F. Takács, A. Ernst, S. Ostanin, J. Henk, I. Mertig, P. Bruno, T. Miyamachi, S. Suga, and W. Wulfhekel, *Magnetic anisotropy and magnetization dynamics of individual atoms and clusters of Fe and Co on Pt(111),* Phys. Rev. Lett. **102**, 257203 (2009).

[116] A. A. Khajetoorians, J. Wiebe, B. Chilian, S. Lounis, S. Blügel, and R. Wiesendanger, *Atom-by-atom engineering and magnetometry of tailored nanomagnets,* Nat. Phys. **8**, 497 (2012).

[117] A. A. Khajetoorians, M. Steinbrecher, M. Ternes, M. Bouhassoune, M. dos Santos Dias, S. Lounis, J. Wiebe, and R. Wiesendanger, *Tailoring the chiral magnetic*

interaction between two individual atoms, Nat. Commun. **7**, 10620 (2016).

[118] B. Bryant, A. Spinelli, J. J. T. Wagenaar, M. Gerrits, and A. F. Otte, *Local control of single atom magnetocrystalline anisotropy,* Phys. Rev. Lett. **111**, 127203 (2013).

[119] K. Morgenstern, N. Lorente, and K.-H. Rieder, *Controlled manipulation of single atoms and small molecules using the scanning tunnelling microscope,* Phys. Status Solidi B **250**, 1671 (2013).

[120] L. Bartels, G. Meyer, and K.-H. Rieder, *Basic steps of lateral manipulation of single atoms and diatomic clusters with a scanning tunneling microscope tip,* Phys. Rev. Lett. **79**, 697 (1997).

[121] M. Ternes, C. P. Lutz, C. F. Hirjibehedin, F. J. Giessibl, and A. J. Heinrich, *The force needed to move an atom on a surface,* Science **319**, 1066 (2008).

[122] J. F. Shackelford and W. Alexander, *CRC Materials Science and Engineering Handbook*, 3rd ed. (CRC Press, 2000).

[123] J. A. Stroscio and R. J. Celotta, *Controlling the dynamics of a single atom in lateral atom manipulation,* Science **306**, 242 (2004).

[124] A. A. Khajetoorians, M. Valentyuk, M. Steinbrecher, T. Schlenk, A. Shick, J. Kolorenc, A. I. Lichtenstein, T. O. Wehling, R. Wiesendanger, and J. Wiebe, *Tuning emergent magnetism in a Hund's impurity,* Nat. Nanotech. **10**, 958 (2015).

[125] J. Sinova, S. O. Valenzuela, J. Wunderlich, C. H. Back, and T. Jungwirth, *Spin Hall effects,* Rev. Mod. Phys. **87**, 1213 (2015).

[126] N. Nagaosa, J. Sinova, S. Onoda, A. H. MacDonald, and N. P. Ong, *Anomalous Hall effect,* Rev. Mod. Phys. **82**, 1539 (2010).

[127] A. Manchon, H. C. Koo, J. Nitta, S. M. Frolov, and R. A. Duine, *New perspectives for Rashba spin-orbit coupling,* Nat.Mater. **14**, 871 (2015).

[128] B. G. Park, J. Wunderlich, X. Martí, X., V. Holý, V., Y. Kurosaki, M. Yamada, H. Yamamoto, A. Nishide, J. Hayakawa, H. Takahashi, and et al., *A spin-valve-like magnetoresistance of an antiferromagnet-based tunnel junction,* Nat. Mater. **10**, 347351 (2011).

[129] S.-H. Yang, K.-S. Ryu, and S. Parkin, *Domain-wall velocities of up to 750 m s^{-1} driven by exchange-coupling torque in synthetic antiferromagnets,* Nat. Nanotech.

10, 221 (2015).

[130] H. D. Chopra and S. Z. Hua, *Ballistic magnetoresistance over 3000% in Ni nanocontacts at room temperature,* Phys. Rev. B **66**, 020403 (2002).

[131] N. García, M. Muñoz, and Y.-W. Zhao, *Magnetoresistance in excess of 200% in ballistic Ni nanocontacts at room temperature and 100 Oe,* Phys. Rev. Lett. **82**, 2923 (1999).

[132] A. Brataas, G. Tatara, and G. E. W. Bauer, *Ballistic and diffuse transport through a ferromagnetic domain wall,* Phys. Rev. B **60**, 3406 (1999).

[133] H. Imamura, N. Kobayashi, S. Takahashi, and S. Maekawa, *Conductance quantization and magnetoresistance in magnetic point contacts,* Phys. Rev. Lett. **84**, 1003 (2000).

[134] A. K. Zvezdin and A. F. Popkov, *Effect of domain boundary on the electrical conductivity of a magnetic nanocontact,* JETP Lett. **71**, 209 (2000).

[135] A. von Bieren, A. K. Patra, S. Krzyk, J. Rhensius, R. M. Reeve, L. J. Heyderman, R. Hoffmann-Vogel, and M. Kläui, *Domain-wall induced large magnetoresistance effects at zero applied field in ballistic nanocontacts,* Phys. Rev. Lett. **110**, 067203 (2013).

[136] B. Doudin and M. Viret, *Ballistic magnetoresistance?* J. Phys.: Condens. Matter **20**, 083201 (2008).

[137] S. Egle, C. Bacca, H. F. Pernau, M. Huefner, D. Hinzke, U. Nowak, and E. Scheer, *Magnetoresistance of atomic-size contacts realized with mechanically controllable break junctions,* Phys. Rev. B **81**, 134402 (2010).

[138] M. Ye. Zhuravlev, E. Y. Tsymbal, S. S. Jaswal, A. V. Vedyayevb, and B. Dieny, *Spin blockade in ferromagnetic nanocontacts,* Appl. Phys. Lett. **83**, 3534 (2003).

[139] N. Néel, J. Kröger, and R. Berndt, *Quantized conductance of a single magnetic atom,* Phys. Rev. Lett. **102**, 086805 (2009).

[140] K. Tao, I. Rungger, S. Sanvito, and V. S. Stepanyuk, *Quantum conductance of a single magnetic atom: An ab initio study,* Phys. Rev. B **82**, 085412 (2010).

[141] J. Velev, R. F. Sabirianov, S. S. Jaswal, and E. Y. Tsymbal, *Ballistic anisotropic magnetoresistance,* Phys. Rev. Lett. **94**, 127203 (2005).

[142] D. Jacob, J. Fernández-Rossier, and J. J. Palacios, *Anisotropic magnetoresistance*

in nanocontacts, Phys. Rev. B **77**, 165412 (2008).

[143] G. Autès, C. Barreteau, D. Spanjaard, and M.-C. Desjonquères, *Electronic transport in iron atomic contacts: From the infinite wire to realistic geometries,* Phys. Rev. B **77**, 155437 (2008).

[144] A. Smogunov, A. Dal Corso, and E. Tosatti, *Magnetic phenomena, spin-orbit effects, and Landauer conductance in Pt nanowire contacts: Density-functional theory calculations,* Phys. Rev. B **78**, 014423 (2008).

[145] M. Häfner, J. K. Viljas, and J. C. Cuevas, *Theory of anisotropic magnetoresistance in atomic-sized ferromagnetic metal contacts,* Phys. Rev. B **79**, 140410 (2009).

[146] A. Sokolov, C. Zhang, E. Y. Tsymbal, J. Redepenning, and B. Doudin, *Quantized magnetoresistance in atomic-size contacts,* Nat. Nanotech. **2**, 171 (2007).

[147] S.-F. Shi and D. C. Ralph, *Atomic motion in ferromagnetic break junctions,* Nat. Nanotech. **2**, 522–522 (2007).

[148] B. Hardrat, N.-P. Wang, F. Freimuth, Y. Mokrousov, and S. Heinze, *One-dimensional ballistic transport with FLAPW wannier functions,* Phys. Rev. B **85**, 245412 (2012).

[149] Y. Mokrousov, G. Bihlmayer, and S. Blügel, *Full-potential linearized augmented plane-wave method for one-dimensional systems: Gold nanowire and iron monowires in a gold tube,* Phys. Rev. B **72**, 045402 (2005).

[150] F. Otte, S. Heinze, and Y. Mokrousov, *Molecular anisotropic magnetoresistance,* Phys. Rev. B **92**, 220411 (2015).

[151] L. Gross, N. Moll, F. Mohn, A. Curioni, G. Meyer, F. Hanke, and M. Persson, *High-resolution molecular orbital imaging using a p-wave STM tip,* Phys. Rev. Lett. **107**, 086101 (2011).

[152] P. Krams, F. Lauks, R. L. Stamps, B. Hillebrands, and G. Güntherodt, *Magnetic anisotropies of ultrathin Co(001) films on Cu(001),* Phys. Rev. Lett. **69**, 3674 (1992).

[153] W. Weber, A. Bischof, R. Allenspach, C. H. Back, J. Fassbender, U. May, B. Schirmer, R. M. Jungblut, G. Güntherodt, and B. Hillebrands, *Structural relaxation and magnetic anisotropy in Co/Cu(001) films,* Phys. Rev. B **54**, 4075

(1996).

[154] C. A. F. Vaz, J. A. C. Bland, and G. Lauhoff, *Magnetism in ultrathin film structures,* Rep. Prog. Phys. **71**, 056501 (2008).

[155] M. Bode, M. Getzlaff, A. Kubetzka, R. Pascal, O. Pietzsch, and R. Wiesendanger, *Temperature-dependent exchange splitting of a surface state on a local-moment magnet: Tb(0001),* Phys. Rev. Lett. **83**, 3017 (1999).

[156] W. Wulfhekel, F. Zavaliche, R. Hertel, S. Bodea, G. Steierl, G. Liu, J. Kirschner, and H. P. Oepen, *Growth and magnetism of Fe nanostructures on W(001),* Phys. Rev. B **68**, 144416 (2003).

[157] K. von Bergmann, M. Bode, and R. Wiesendanger, *Magnetism of iron on tungsten (001) studied by spin-resolved scanning tunneling microscopy and spectroscopy,* Phys. Rev. B **70**, 174455 (2004).

[158] A. G. Worthing, *Physical properties of well seasoned molybdenum and tantalum as a function of temperature,* Phys. Rev. **28**, 190 (1926).

12. Acknowledgments

I am deeply grateful for all the people, who supported me over the years with fruitful discussions and collaborations, which helped to shed light on my experimental results. I want to thank...

- Prof. Dr. Richard Berndt, for giving me the opportunity to work in his group, for letting me pursue my own experimental ideas and for invaluable suggestions during my work.
- Prof. Dr. Stefan Heinze and his former group members Dr. Paolo Ferriani, Dr. Nuala Mai Caffrey, Dr. Fabian Otte and Dr. Silke Schröder for helpful discussions and calculations, which allowed for a better understanding of my experimental results.
- Dr. Nuala Mai Caffrey for her calculations of the spin polarization of Ir atoms and the Fe bilayer, which are presented in chapter **6**.
- Dr. Paolo Ferriani for his first DFT calculations of the Pb dimers, which are promising.
- Dr. Fabian Otte for his tight-binding model and his DFT calculations of the BAMR, which are presented in chapter **8**.
- Prof. Dr. Jörg Kröger and Dr. Nicolas Néel for their experimental work on the Co adatoms, which complemented my work on the BAMR of the Ir adatoms.
- Dr. Manuel Gruber and Dr. Alexander Weismann for proofreading parts of this thesis.
- the team of the 4K laboratory: Dr. Alexander Weismann, Torben Jasper-Tönnies, Andreas Burtzlaff, Michael Mohr and Neda Noei.
- René Woltmann, Frank Brach and his co-workers in the precision work shop for technical advice and manufacturing components that were essential for my experiments.
- Monika Seeger for always helping me out when a wild bureaucratic task appeared.

Finally, I want to thank my family and Katharina for their unconditional support. This work was supported by the DFG through SFB 668, which is gratefully acknowledged.

Eidesstattliche Erklärung

Hiermit erkläre ich, dass ich diese Arbeit unter Einhaltung der Regeln guter wissenschaftlicher Praxis der Deutschen Forschungsgemeinschaft selbstständig erstellt habe. Diese Arbeit ist - abgesehen von der Beratung durch meine wissenschaftlichen Lehrer - nach Inhalt und Form meine eigene und sie wurde weder ganz noch in Teilen an anderer Stelle im Rahmen eines Prüfungsverfahrens vorgelegt, veröffentlicht oder zur Veröffentlichung eingereicht. Frühere Promotionsversuche wurden von mir nicht vorgenommen.

Kiel, 2016

(Johannes Schöneberg)